INFORMATION TO USERS

This manuscript has been reproduced from the microfilm master. UMI films the text directly from the original or copy submitted. Thus, some thesis and dissertation copies are in typewriter face, while others may be from any type of computer printer.

The quality of this reproduction is dependent upon the quality of the copy submitted. Broken or indistinct print, colored or poor quality illustrations and photographs, print bleedthrough, substandard margins, and improper alignment can adversely affect reproduction.

In the unlikely event that the author did not send UMI a complete manuscript and there are missing pages, these will be noted. Also, if unauthorized copyright material had to be removed, a note will indicate the deletion.

Oversize materials (e.g., maps, drawings, charts) are reproduced by sectioning the original, beginning at the upper left-hand corner and continuing from left to right in equal sections with small overlaps. Each original is also photographed in one exposure and is included in reduced form at the back of the book.

Photographs included in the original manuscript have been reproduced xerographically in this copy. Higher quality 6" x 9" black and white photographic prints are available for any photographs or illustrations appearing in this copy for an additional charge. Contact UMI directly to order.

UMI

A Bell & Howell Information Company
300 North Zeeb Road, Ann Arbor MI 48106-1346 USA
313/761-4700 800/521-0600

HARVARD UNIVERSITY
Graduate School of Arts and Sciences

THESIS ACCEPTANCE CERTIFICATE

The undersigned, appointed by the

Division

Department of Physics

Committee

have examined a thesis entitled
"A Search for ν_μ to ν_e Oscillations with the NOMAD Detector at the CERN SPS"

presented by Thomas Dignan

candidate for the degree of Doctor of Philosophy and hereby certify that it is worthy of acceptance.

Signature .....

Typed name Gary Feldman, Chair

Signature .....

Typed name Melissa Franklin

Signature .....

Typed name Howard Georgi

Date February 26, 1998

A Search for ν_μ to ν_e Oscillations with the NOMAD Detector at the CERN SPS

A thesis presented

by

Thomas Gerardo Paul Mungo Dignan

to

The Department of Physics

in partial fulfillment of the requirements

for the degree of

Doctor of Philosophy

in the subject of

Physics

Harvard University

Cambridge, Massachusetts

June 1998

Abstract

The results of a search for the oscillation $\nu_\mu \rightarrow \nu_e$ with the NOMAD experiment at the CERN SPS wide band ν_μ beam are presented. After a total of approximately 1×10^{19} protons on target worth of data were analyzed, no evidence of excess ν_e production was observed. A limit of 3.2×10^{-3} on $\sin^2(2\theta)$ in the high Δm^2 limit is set at a 90% C.L. and a limit on Δm^2 of less than 1 eV^2/c^4 is set for full mixing.

Acknowledgments

When one has been in graduate school as long as I have, one develops a great many relationships and each one in their own way shapes a person for better or worse. I would like to acknowledge some of those people here. There are a great many of you so if I have left you out I hope that you don't think it was done intentionally. It may have been, but I wouldn't want you to think that.

First and foremost I would like to thank Sanjib Mishra and Gary Feldman. Their advice, guidance and friendship have molded me into the physicist and man that I am today (does anybody really want that kind of responsibility?) I would also like to thank Melissa Franklin for her early encouragement.

Secondly I would have never made it this far without the help of my fellow Harvardians Peter Hurst, Dan Hubbard and Fred Weber. Their level enthusiasm and optimistic outlook may have been the deciding factor in my not losing all faith and hope in this experiment. And to Dave Daniels who actually read the thing. Equally important are my collaborators on the NOMAD experiment, who provided the opportunity to overcome the challenges that we constantly faced.

My conspirators in crime at CERN know who they are (if they remember). Thanks to Hal for providing me with a floor, a cold shower and an audience, to Dave P. for giving me a sense of perspective, to Andrew, Andrew, Jim, Emmett and Martin for helping me to lose said sense, to Dave S. for showing me where sense goes beyond sensibility, to Damon and Jean for keeping me in shape, to Steve for having faith in me in the clutch, to Ofer for Pogeybait [1] and of course to Zimm for not falling on me. Then there's Shank.

Meanwhile, back in the jungle, I was duped into feeling I had a life by many people. In particular Michael provided abuse and a shower curtain for protection, Andrew was there with quandary and what not, Colin proved that the Guiness from the top of the keg is better, Rowan really was from Texas (or was that Cal), Tom gave me wood, Maria let me wear her hat, Ted fed me frogs, Jun taught me the benefit of self-control and Robyn was persecuted. Rich, John, Dave, Eric, Matt, Railbaron. Gina and Tania gave me a roof and cards. Al was Al. A lot. And let's not forget those guys from home, Coban who is acting responsibly (whoa!) and Nick who doesn't mind staying up all night talking about salt.

My unending gratitude goes to my parents without who, of course, I wouldn't be here. Their faith and support in me has made all of this possible. Thanks to Sette and Molly, my sisters, for being there to tell me when I'm out of line. Also thanks to Lola for smiling.

Contents

List of Figures

List of Tables

Chapter 1

Introduction

The question of massiveness of the neutrino has been with us since its inception. There is no a priori reason for the neutrino to have a mass of zero yet its size is much smaller than its other fermionic companions in the Standard Model. As the direct search for a non-zero mass component continues, the world turns to other more indirect means of determining once and for all the answer to that elusive question: Does the neutrino have mass?

The neutrino oscillation effect has long been known to be a consequence of the massiveness of neutrinos. Several experiments recently have had results which could be interpreted as evidence for neutrino oscillations. The continued deficit of solar neutrinos has many people proposing that this effect is due to neutrino oscillations. The ratio of ν_μ to ν_e from atmospheric neutrinos has been measured to be off by a factor of two from expected. This could also be due to neutrino oscillations. Most recently the LSND experiment has observed an excess of $\overline{\nu_e}$

events, which has persisted after significant increases of statistics. This also could be explained by ν oscillations.

Massive neutrinos also gain impetus from cosmology. Many cosmologists believe the universe to be flat, i.e., that the universe will eventually come to rest. The luminous matter in the universe can account for only about 1% of the total needed to have a flat universe. It has been postulated that neutrino remnants from the Big Bang can account for a significant fraction of this amount if they have mass. Neutrinos with mass of the order 10 eV/c^2 are currently favored, which is precisely the range probed by the NOMAD experiment.

The NOMAD (Neutrino Oscillation MAgnetic Detector) experiment was first proposed to look for $\nu_\mu \rightarrow \nu_\tau$ oscillations, but was designed to be able to perform as a multi-purpose neutrino experiment. The detector was particularly geared toward the identification of electrons and the electron decay of tau is one of the most sensitive channels in the search for $\nu_\mu \rightarrow \nu_\tau$ oscillations. A search for $\nu_\mu \rightarrow \nu_e$ oscillations can thus also be undertaken.

Here within is discussed an attempt to find evidence for $\nu_\mu \rightarrow \nu_e$ oscillations of the same order as that seen at the LSND experiment with data from the NOMAD detector.

Chapter 2

History and Background

2.1 The Birth of the Neutrino

One of the main problems confronting Physics in the late 1920s was the energy spectrum of electrons coming from radioactive beta-decay [2]. The expected spectrum from a two-body decay is monochromatic yet, when measured, the beta-decay spectrum was anything but. So problematic was it that it was proposed that energy conservation might need to be thrown out. To explain this discrepancy Wolfgang Pauli proposed that there was a third, undetected, neutral, light particle involved in the process that carried off the missing energy. Enrico Fermi later used this particle in his 4-point interaction model of beta-decay and dubbed it the neutrino.

The success of Fermi's theory in predicting the shape of the Kurie plot, the beta decay spectrum, solidified the existence of the neutrino in most people's

minds. It was believed to be a very light or massless, weakly interacting particle. Due to the extremely feeble strength of the weak nuclear force, direct evidence for the neutrino would have to wait over twenty years. In 1956 Reines and Cowen [3] made the first observation of antineutrinos. The experiment consisted of looking for the reaction:

$$\overline{\nu} + p \rightarrow e^{+} n \tag{2.1}$$

by observing two gammas, one produced by neutron capture, the other produced by the positron annihilating with an electron, in coincidence in a large liquid scintillation detector.

Melvin Schwartz and Bruno Pontecorvo proposed making beams of neutrinos at accelerators from the decays of pions and kaons:

$$\pi \rightarrow \mu\nu \qquad \text{and} \qquad \mathrm{K} \rightarrow \mu\nu. \tag{2.2}$$

In 1962 G. Danby *et al.* [4] created such a beam at the Brookhaven AGS using a 15 GeV proton beam directed at a beryllium target to produce π's and K's. The neutrinos were detected in a ten-ton spark chamber with aluminum plates separated by lucite spacers. A substantial difference in the number of muons produced from the number of electrons produced showed that neutrinos from the above reactions generate muons preferentially to electrons. It was thus shown that there were two flavors of neutrino, one associated with electrons (the electron

neutrino or ν_e) such as those produced in beta decay, and one associated with muons (the muon neutrino or ν_μ) such as those found in the muonic decays of pions.

Since the discovery of the τ lepton in 1976 [5] it is believed that there are three flavors of neutrinos. There is a significant amount of evidence to support this from neutrino scattering experiments in which ν_μ's fail to produce τ's. Also, fits of the invisible width of the Z^0 resonance show that there are three light neutrinos. As of yet though, there has been no direct evidence for the existence of ν_τ.

2.2 The Mass of the Neutrino

The neutrino was first postulated to be light, but this does not necessarily mean massless. In the currently favored model of elementary interactions, the masses of the neutrinos are set to zero but there is no a priori reason why this should be the case.

When Fermi first made his theory of beta-decay he observed that the introduction of neutrino mass would produce a nonlinearity in the Kurie plot near the endpoint of the spectrum. Indeed this is still the preferred method for direct measurement of the ν_e mass. A limit of about 5 eV/c^2 on the mass of the ν_e has been set by looking at the end point spectrum of tritium beta-decay. In actuality, the mass squared of the neutrino is what is measured and many of these tritium

measurements have produced a mass-squared which is negative, clearly unphysical. The Particle Data Group [6] estimates that there is only a 3.5% chance given all the measurements and reported errors that the mass-squared of the ν_e is positive. Needless to say, this result is controversial.

A similar problem existed in the measurement of the mass of the ν_μ. The preferred method measures the momentum of the outgoing muon p_μ in the reaction:

$$\pi^+ \rightarrow \mu^+ \nu_\mu \tag{2.3}$$

where

$$p_\mu^2 = \frac{(m_\pi^2 + m_\mu^2 - m_\nu^2)^2}{4m_\pi^2} - m_\mu^2. \tag{2.4}$$

Again m_ν^2 is the value that is actually measured. Until recently the mass squared of the ν_μ was found to be negative. A new measurement of the pion mass helps to alleviate this problem and limit of 0.17 MeV/c^2 can be set for the ν_μ mass.

The mass of the tau neutrino is estimated from high multiplicity decays of tau. The current best limit is set from a fit to the invariant mass of the decay:

$$\tau \rightarrow 5\pi(\pi^0) \tag{2.5}$$

and is found to be 24 MeV/c^2.

2.3 Majorana versus Dirac Neutrino

CPT transforms ν_L into $\overline{\nu_R}$. If the mass of the neutrino is non-zero then a Lorentz boost can flip helicity. That means that a left-handed neutrino can be transformed into a right handed neutrino. If ν_L and $\overline{\nu_R}$ are distinct states the neutrino is called a Dirac particle. This is just like the other fermions in the Standard Model, such as the the electron and the quarks.

The neutrino is different. Since it has no charge it is possible that its anti-particle is the same state. In this case the neutrino would be called a Majorana particle. It would then be possible for weak interactions to violate lepton number conservation.

2.4 Mass in the Standard Model

The Standard Model, an $SU(2)_L \times U(1)_Y$ gauge theory, has been incredibly successful at predicting the properties of electromagnetic and weak interactions. In the Standard Model, though, mass terms in the Lagrangian violate gauge invariance. This problem was overcome by invoking a new scalar isodoublet

$$\phi = \begin{pmatrix} \phi_+ \\ \phi_0 \end{pmatrix} \tag{2.6}$$

with the following interaction V

$$V = -\mu^2 \phi^\dagger \phi + \lambda (\phi^\dagger \phi)^2. \tag{2.7}$$

This introduces new gauge invariant interaction terms

$$L_Y = -\begin{pmatrix} \overline{\nu} \\ \overline{l} \end{pmatrix}_L \phi l_R + h.c. \tag{2.8}$$

If $-\mu^2 < 0$ then ϕ acquires a vacuum expectation value η and via a gauge transformation can take on the form:

$$\phi(x) = \frac{1}{\sqrt{2}}\eta + \sigma(x). \tag{2.9}$$

This process is known as spontaneous symmetry breaking. The vacuum expectation value gives masses to the gauge bosons and via the term L_m in the Lagrangian,

$$L_m = -m(\bar{l}_L l_R + \bar{l}_R l_L) = -m\bar{l}l \tag{2.10}$$

it also gives masses to the fermions.

In the Standard Model the neutrino has no right-handed component; therefore, as seen in equation (2.10), the neutrino will have no mass term and thus no mass. In a simple extension to the Standard Model, a right-handed component to the neutrino can be invoked which will give the mass terms in the Lagrangian L_m

$$L_m = -m(\overline{\nu}_L \nu_R + \overline{\nu}_R \nu_L) = -m\overline{\nu}\nu. \tag{2.11}$$

This creates a leptonic sector of the Standard Model with a 3×3 matrix for mixing between generations, as well as providing mass for the neutrinos, similar to that in the quark sector. Since the neutrinos have zero charge, their right-hand

components are singlets of $SU(2)_L \times U(1)_Y$ so there can be a new gauge invariant mass term

$$L_{bare} = -\frac{1}{2}b(\overline{\hat{\nu}_L}\nu_R + h.c.) \tag{2.12}$$

The mass term for the neutrinos in the Lagrangian now take the form

$$-L_{mass} = \frac{1}{2}\begin{pmatrix} \overline{\nu}_L & \overline{\hat{\nu}_L} \end{pmatrix}\begin{pmatrix} 0 & m \\ m & b \end{pmatrix}\begin{pmatrix} \hat{\nu}_R \\ \nu_R \end{pmatrix} \tag{2.13}$$

When this mass matrix is diagonalized these two eigenvalues

$$m_{1,2} = \frac{1}{2}(\sqrt{b^2 + 4m^2} \mp b) \tag{2.14}$$

and these two Eigenvectors

$$\begin{pmatrix} n_{1L} \\ n_{2L} \end{pmatrix} = \begin{pmatrix} \cos\theta & -\sin\theta \\ \sin\theta & \cos\theta \end{pmatrix}\begin{pmatrix} \nu_L \\ \hat{\nu}_L \end{pmatrix} \tag{2.15}$$

and

$$\begin{pmatrix} n_{1R} \\ n_{2R} \end{pmatrix} = \begin{pmatrix} -\cos\theta & \sin\theta \\ \sin\theta & \cos\theta \end{pmatrix}\begin{pmatrix} \nu_R \\ \hat{\nu}_R \end{pmatrix} \tag{2.16}$$

are found, where

$$\tan 2\theta = \frac{2m}{b}. \tag{2.17}$$

The new mass term in the Lagrangian now reads

$$-L_{mass} = m_1\overline{n}_{1L}n_{1R} + m_2\overline{n}_{2L}n_{2R} + h.c. \tag{2.18}$$

It can be seen that

$$n_1 = -\hat{n}_1 \text{ and } n_2 = \hat{n}_2. \tag{2.19}$$

These are two massive Majorana neutrinos.

An interesting case is where $b \gg m$. In this case it is seen that the masses gotten for the two neutrino states of

$$m_1 \simeq \frac{m^2}{b} \text{ and } m_2 \simeq b \tag{2.20}$$

one very light neutrino m_1 and one heavy neutrino m_2. This effect is known as the See-Saw Mechanism. It is very elegant as it can explain the apparent lightness of the neutrino quite naturally.

2.5 Neutrino Oscillations

Neutrinos are created in weak flavor eigenstates which are assumed to be a superposition of mass eigenstates. One of the consequences of neutrinos having a non-zero mass is that these mass eigenstates evolve differently in time. When neutrinos are then detected in weak eigenstates they are not necessarily in the same state as at the time of creation. This effect is called a neutrino oscillation.

More formally, neutrinos are generated for N generations of neutrinos as:

$$|\nu_l >= \sum_{i=1}^{N} U_{li} |\nu_i > \tag{2.21}$$

and they evolve in time as

$$|\nu_l(t) >= \sum_{i=1}^{N} U_{li} e^{-iE_i t} |\nu_i > \tag{2.22}$$

In most cases the neutrinos are ultra-relativistic:

$$p \gg m_i \Rightarrow E_i \simeq p + \frac{m_i^2}{2p} \tag{2.23}$$

so

$$|\nu_l(t)>= e^{-ipt}\sum_{i=1}^{N} U_{li}e^{-i\frac{m_i^2}{2p}t}|\nu_i> . \tag{2.24}$$

The probability for $(l \to l')$ is therefore

$$P_{ll'} = |\sum U_{li}U_{il'}^{\dagger}e^{-i\frac{m_i^2}{2p}t}|^2 \tag{2.25}$$

$$= \sum |U_{li}U_{il'}^{\dagger}|^2 + Re\sum_i\sum_{i\neq j} U_{li}U_{il'}^{\dagger}U_{lj}U_{jl'}^{\dagger}e^{-i\frac{|m_i^2-m_j^2|}{2p}L} \tag{2.26}$$

For the case of two neutrinos this reduces to

$$P_{ll'} = \sin^2 2\theta \sin^2 \frac{L}{L_{osc}} \tag{2.27}$$

where

$$L_{osc}(km) = \frac{E_\nu(\mathrm{GeV})}{1.27|m_1^2 - m_2^2|(\mathrm{eV}^2/\mathrm{c}^4)} \tag{2.28}$$

is the characteristic oscillation length.

This derivation in fact is not obviously correct as it assumes that p is fixed. If one does a momentum wave packet expansion in order to derive the oscillation probability, one does in fact get the same result [7].

2.6 Hints of Neutrino Oscillations

There are several observed phenomena that can be explained by neutrino oscillations. A few of them are here discussed.

2.6.1 Solar Neutrinos

The sun is powered by nuclear fusion reactions of hydrogen nuclei into helium at its center. The majority of this energy is released in the form of photons, but a significant fraction is carried off by neutrinos. The density of the sun is such that the mean time for a photon generated at the center to reach the surface is on the order 10^6 years. The neutrinos have a much longer interaction length and can emerge straight from the the solar core. Neutrinos can thus provide very useful information about the center of the sun.

A prediction of the flux of neutrinos from the sun is obtainable from the Standard Solar Model. One such model has been made by J. N. Bahcall and M. H. Pinsonneault [8]. The predicted flux of neutrinos from different fusion reactions in the solar core can be seen in Figure 2.1.

Several experiments have been designed to observe solar neutrinos. These experiments can be broken down into two categories, those involving inverse beta-decay (such as GALLEX [17] and SAGE [18] and the Homestake [19] experiment) and those using elastic neutrino-electron scattering (such as Kamiokande [20]).

The inverse beta decay experiments try to observe the reaction

$$\nu_e + (A, Z) \rightarrow e^- + (A, Z+1) \tag{2.29}$$

The Homestake experiment, performed by Davis *et al.* in a gold mine in South Dakota since the 1960s, measures the production rate of ^{37}Ar from neutrino

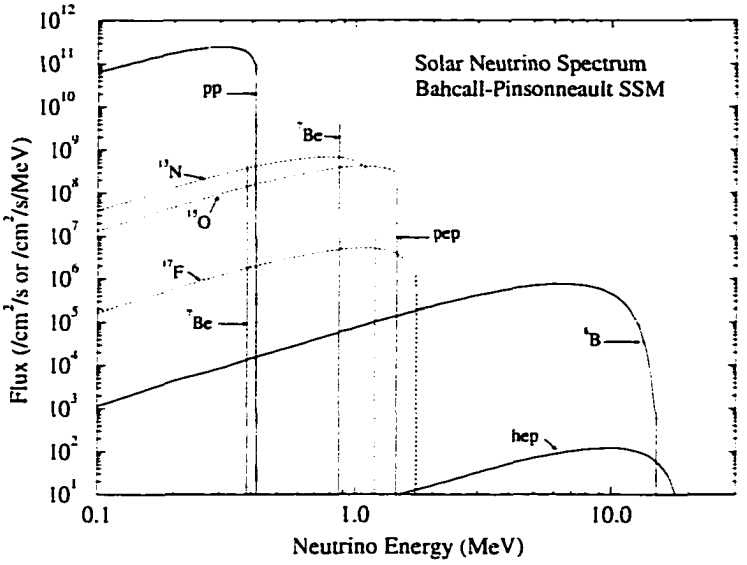

Figure 2.1: Flux of Solar Neutrinos on the Earth from Different Fusion Reactions as Predicted by Bahcall and Pinsonneault.

capture in chlorine via the reaction

$$\nu_e + {}^{37}\mathrm{Cl} \rightarrow \mathrm{e}^- + {}^{37}\mathrm{Ar} \tag{2.30}$$

The energy threshold of this reaction is 0.8 MeV. The GALLEX and SAGE experiments measure the production rate of ^{71}Ge from neutrino capture in gallium via the reaction

$$\nu_e + {}^{71}\mathrm{Ga} \rightarrow \mathrm{e}^- + {}^{71}\mathrm{Ge}. \tag{2.31}$$

The energy threshold for this reaction is much lower (0.2 MeV). This makes gallium experiments more sensitive to a larger fraction of solar neutrinos. Specifically, they are sensitive to *pp* neutrinos which come from hydrogen fusion, the largest source of neutrinos from the sun.

The Kamiokande [20] experiment in the Kamioka mine in Japan measures the flux of solar neutrinos through elastic electron-neutrino scattering via the reaction

$$\nu_e + e^- \rightarrow \nu_e + e^- \tag{2.32}$$

The Kamiokande experiment is a water-Cherenkov detector. It can therefore measure the direction of the incoming neutrinos. The solar origin of the observed neutrinos is easily established. The threshold for this reaction is 7.5 MeV; therefore only the most energetic of solar neutrinos are observable.

Experiment	BP SSM	TCL SSM	Exp
Kamiokande	5.69 ± 0.82	4.4 ± 1.1	$2.80 \pm 0.19 \pm 0.33$
Homestake	8.0 ± 1.0	6.4 ± 1.4	$2.55 \pm 0.17 \pm 0.18$
Gallium(combined)	131.5^{+7}_{-6}	122.5 ± 7	77 ± 9

Table 2.1: Predictions [9] of Bahcall and Pinsonneault (BP SSM) and Turk-Chieze and Lopes (TCL SSM) and measured solar neutrino fluxes and errors for the Kamiokande, Homestake, and Gallium (GALLEX and SAGE) experiments. Numbers for Kamiokande are given in units of 10^6 $cm^{-2}s^{-1}$. All other numbers are given in SNUs. A SNU (Solar Neutrino Unit) is 1 capture per second per 10^{36} target atoms.

In Table 2.1 the measured fluxes for the experiments described above and the predictions from the models of Bahcall and Pinsonneault, and Turk-Chieze and

Lopes are presented. The experimental results are smaller than the prediction in each experiment. There are several possible explanations for this discrepancy. One is that the experiments are mistaken, i.e., there are underestimates of the errors of the measurements. In the case of GALLEX a calibration run using a radioactive chromium source makes this possibility remote. Another possibility that has not been ruled out is that there is a significant error in the Standard Solar Model. For this discussion, though, the possibility that the discrepancy arises from the lack of knowledge of the neutrino, i.e., that it may have mass and therefore oscillate, is the most interesting. If the ν_e were to oscillate in flight between the sun and Earth, where the experiments are, then it may be possible to explain this deficit.

An intriguing possibility is that the oscillation is enhanced by the MSW [10][11] effect. By travelling through matter the electron neutrino gains an effective energy by a charged-current scatter off of electrons, which the other neutrino flavors lack. The electron-neutrino therefore evolves differently in time. The energy of the ν_e is now

$$E_\nu = p + \frac{m^2}{2E} + \sqrt{2} G_F N_e \tag{2.33}$$

where G_F is the Fermi Constant and N_e is the number density of electrons in the matter traveled through. There is now get a new value for the mixing angle $\tilde{\theta}$ given by

$$\tan 2\tilde{\theta} = \frac{\Delta m^2 \sin 2\theta}{\Delta m^2 \cos 2\theta - A} \tag{2.34}$$

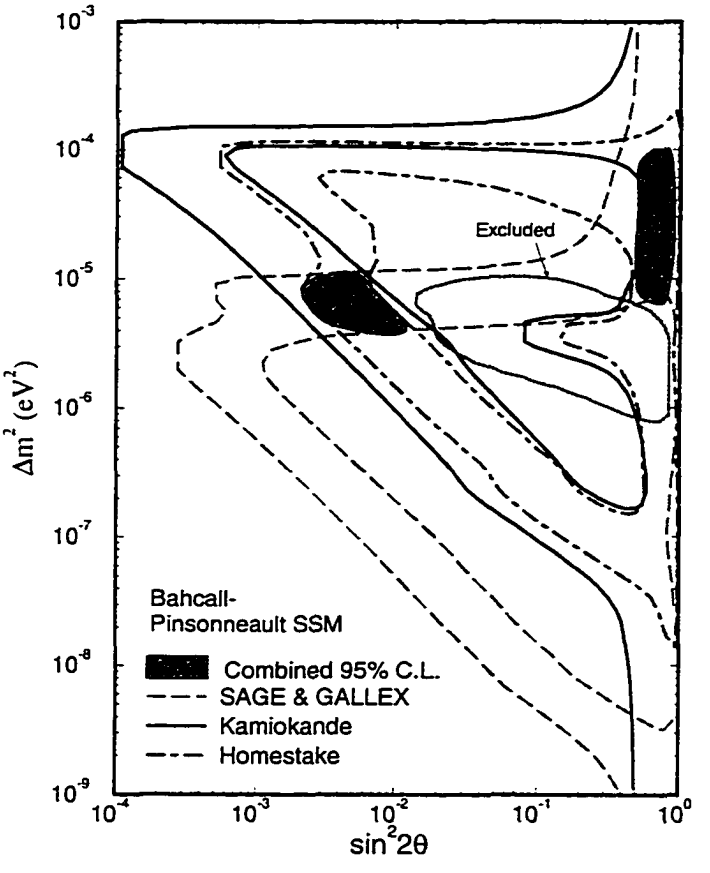

Figure 2.2: Allowed Regions for the Kamiokande, Homestake and Gallium Experiments Using the SSM of Bahcall and Pinsonneault Including the MSW Effect.

where

$$A = 2\sqrt{2}G_F n_e p. \tag{2.35}$$

In Figure 2.2 the regions of the $\Delta m^2 - \sin^2(2\theta)$ space allowed for oscillations by the SSM of Bahcall and Pinsonneault if the MSW effect is taken into account is shown. A Δm^2 of around $10^{-5}\mathrm{eV}^2/\mathrm{c}^4$ can be seen to account for the SSM-experimental discrepancy.

2.6.2 Atmospheric Neutrinos

Cosmic ray protons scatter off of the top of the atmosphere and create pions that decay above the Earth which in turn decay into muons via the reactions

$$\pi \rightarrow \mu + \nu_\mu \qquad \mu \rightarrow e + \nu_\mu + \nu_e. \tag{2.36}$$

Naively, a ratio of 2 to 1 for the ratio of ν_μ's to ν_e's from the atmosphere would be expected. Detailed Monte Carlo simulations of protons in the atmosphere confirm that this is correct, but they are not reliable to more than 10% due to uncertainties in hadron cross-sections and the cosmic ray flux.

Several experiments have studied atmospheric neutrinos. Kamiokande [12] and IMB-3 [13] are both water-Cherenkov detectors where as Frejus [14] , Nusex [15] and Soudan-2 [16] are fine-grained iron calorimeter experiments. As can be seen in Table 2.2, a majority of these experiments observe a fewer ν_μ's than expected. Particularly notable is that the effect is seen by the experiments with the largest exposure.

Experiment	Exposure	$\frac{(\frac{\nu_\mu}{\nu_e})_{DATA}}{(\frac{\nu_\mu}{\nu_e})_{MC}}$
Kamiokande	6.1	$0.60 \pm 0.07 \pm 0.05$
IMB-3	7.7	$0.54 \pm 0.05 \pm 0.07$
Frejus	1.6	$1.00 \pm 0.15 \pm 0.08$
Soudan-2	1.0	$0.67 \pm 0.17 \pm 0.09$
Nusex	0.7	0.99 ± 0.29

Table 2.2: Results from Atmospheric Neutrino Observatories. Exposure is given in kiloton-years. The data-MC ratio of $\nu_\mu - \nu_e$ ratios is the standard means of expressing these results.

This anomaly can be taken as evidence for neutrino oscillations. The disappearance of ν_μ's can be accounted for by oscillations into either ν_e's or ν_τ's with a Δm^2 value of around 10^{-2}.

2.6.3 Previous Accelerator Experiments

Neutrinos are created at accelerators by creating pions and kaons from a proton beam hitting a fixed target. These pions and kaons decay in flight, producing neutrinos. The neutrinos from the decays are then detected downstream. Neutrino beams have been generated at BNL, CERN, Fermilab, RAL and Los Alamos and experiments at all of these facilities have conducted neutrino oscillation searches. No one had seen this effect until LSND [21], a mid-range energy experiment at

Los Alamos, saw an excess in the production of $\overline{\nu}_e$'s.

LSND is a tank of 167 tons of liquid scintillator covered by photomultiplier tubes on the tank surface to collect scintillation and Cherenkov light. Neutrinos are created in the beam dump of the 800 MeV proton accelerator, LAMPF, from pions that decay at rest, followed by muons decaying. $\overline{\nu}_e$'s are detected via the reaction

$$\overline{\nu}_e + p \rightarrow e^+ + n \tag{2.37}$$

where the detection of the positron is correlated with the observation of 2.2 MeV gammas from neutron capture in the hydrogen-rich liquid. A tight selection of a positron of energy between 36 and 60 MeV with a correlated 2.2 MeV gamma results in 22 events for 4.6 ± 0.6 background events. The probability that the observed events are entirely due to a statistical fluctuation of the background is 4.1×10^{-8}. If the excess is attributed to the oscillation of $\overline{\nu}_\mu \rightarrow \overline{\nu}_e$ this corresponds to an oscillation probability of $(0.31 \pm 0.12 \pm 0.005)\%$. The allowed region for oscillations is shown in Figure 2.3.

An experiment working in the same energy regime, KARMEN [22], is being conducted with the ISIS proton beam at RAL. So far, KARMEN has seen no excess signal of $\overline{\nu}_e$'s. For large Δm^2 the limit set for the probability of oscillations is set at 8.5×10^{-3}. With more statistics on the way KARMEN should be able to either confirm or disprove the LSND result.

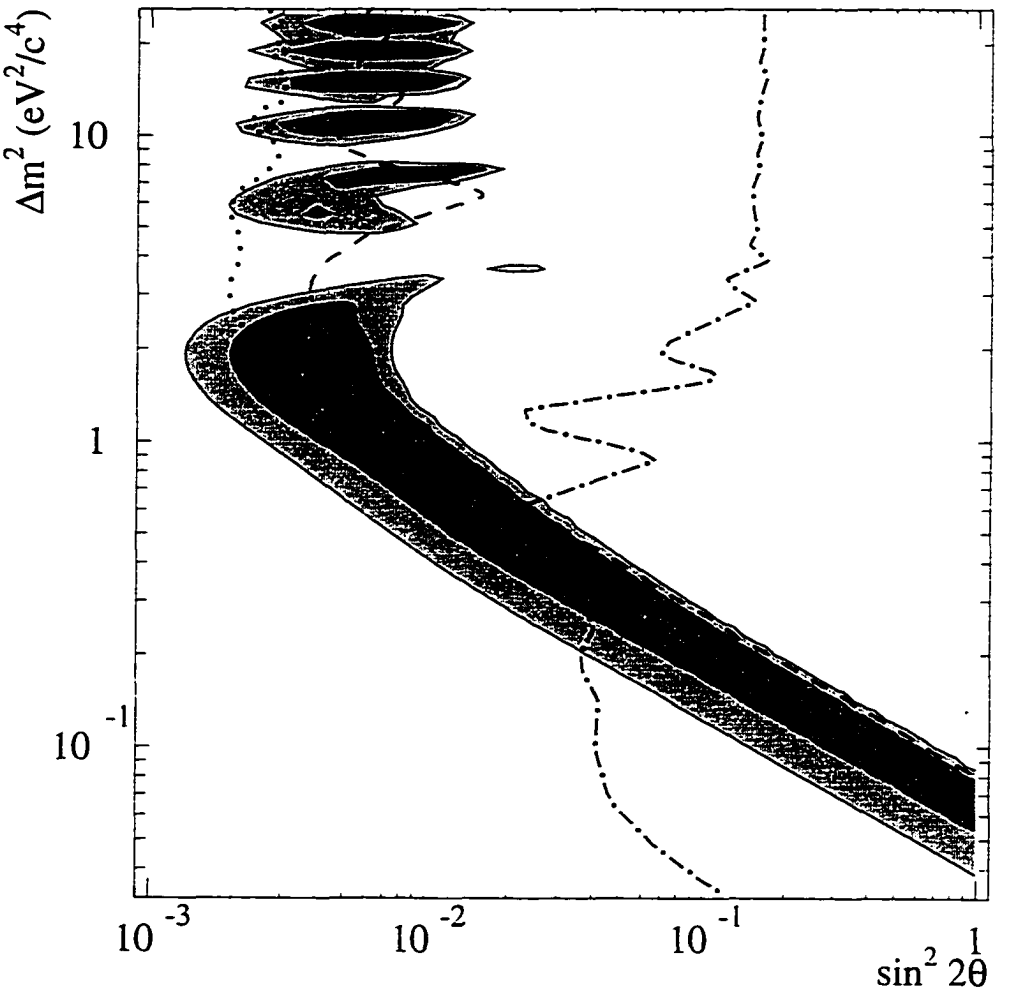

Figure 2.3: Limits at 90% C.L. for $\overline{\nu}_\mu \rightarrow \overline{\nu}_e$ Oscillations for E776 (dotted), KARMEN (dashed) and Bugey, a reactor experiment, (dot-dashed) and the regions favored by LSND at 99% (light-shaded) and 90% (dark-shaded) likelihood [21].

2.6.4 Summation

Three different anomalies can be explained by the existence of $\nu_\mu \rightarrow \nu_e$ oscillations but all three are in very different regions of Δm^2 space. The solar neutrino problem requires a value of Δm^2 around 10^{-5} eV$^2/c^4$, the atmospheric neutrino anomaly calls for a value closer to 10^{-2} eV$^2/c^4$ and LSND favors a value closer to 1 eV$^2/c^4$. Clearly, more study is necessary to reconcile all these numbers.

Chapter 3

Experimental Setup

NOMAD (Figure 3.1) was conceived as an electronic bubble chamber. The target region, a series of drift chambers, also acts as a tracking apparatus. Located in a magnetic field, it is used for measuring the momentum of charged particles. This is followed downstream by the transition radiation detector, the preshower and the electro-magnetic calorimeter (ECal) which are used for electron identification. The ECal is also used to measure photon energy. Next, there is the hadronic calorimeter used to measure neutral hadron energy and finally the muon chambers, used to identify muons. This enables the experiment to benefit from being able both to look at a large statistical sample and to look at the kinematic details of events. Upstream from the main NOMAD detector is the forward calorimeter which is able to accumulate a large statistical sample of neutrino interactions for studies of charm production as well as to look for new weakly interacting particles that may be produced from neutrinos.

Most of the information in this section is taken from [23] and [24].

3.1 Coordinate System

The convention for the coordinate system is: z is the beam direction (ignoring the 42.53 mrad tilt of the beam in the vertical direction), y is vertical (down to up), and x is horizontal (from counting room to the gas hut). In other words, the x-z plane is parallel with the surface of the floor of the hall. The Magnetic field points in the positive x direction. The coordinates u and v are $-5°$ and $+5°$ from y, respectively.

The origin is defined to be at the inner edge of the basket at the incoming beam side and by the support axis of the basket.

3.2 The Forward Calorimeter

The forward support I's of NOMAD have been instrumented with scintillator counters in order to provide an additional massive target upstream of the main detector. Four sets of 5 scintillator counters are ganged together in the 20 gaps between the iron planes and stacked 10 high.

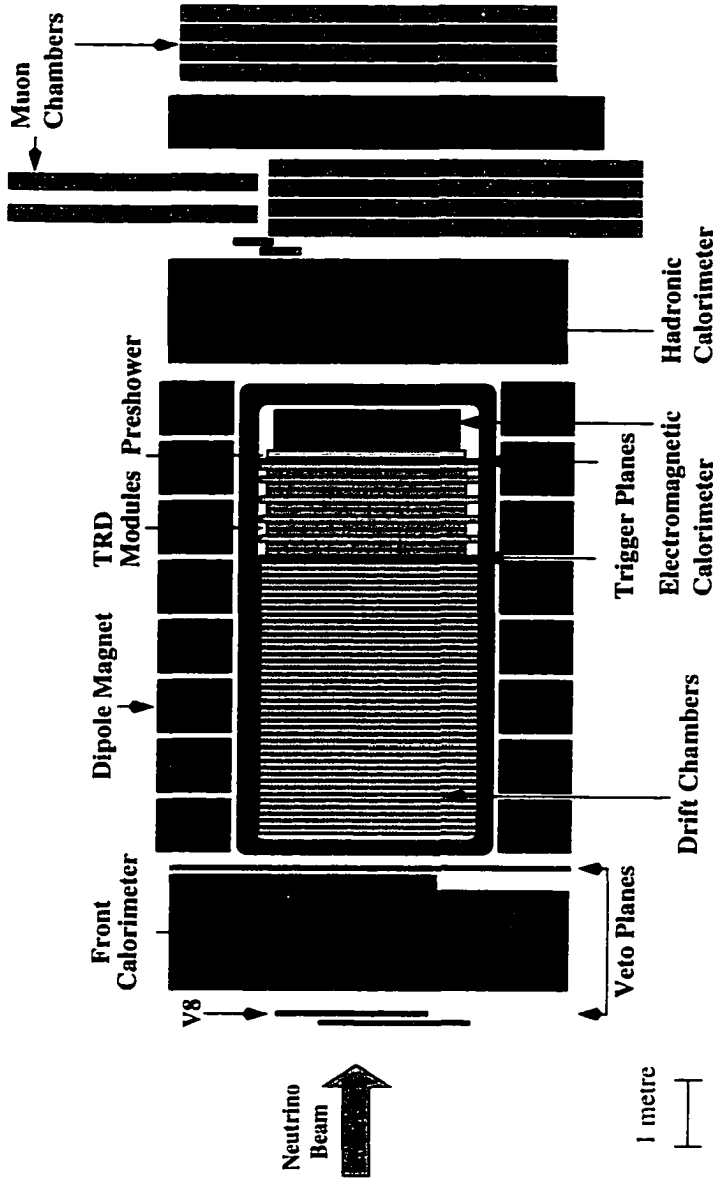

Figure 3.1: Side View of the NOMAD Detector.

3.3 The Veto Counters

The veto is placed upstream to eliminate triggers due to charged particles not coming from interactions in the fiducial volume. The veto consists of 53 scintillators organized into 9 banks. The slabs of scintillator are made out of NE110 and they come in two sizes (long and short). Most scintillators have double-ended read-out through wedge shaped light-guides that feed into Philips XP2020 photomultipliers. These are then mean-timed, forming one signal per counter that is fed onto a TDC channel. The three scintillators in bank 9 are single-ended and only have read-out from the top. The signals from all counters are then or'ed to form the veto. A veto anti-coincidence with hits in the two trigger planes is required for the standard NOMAD trigger.

Veto Statistics :

- size of long scintillator : 2.1 cm x 21.2 cm x 300.0 cm
- size of short scintillator : 2.1 cm x 21.2 cm x 210.0 cm
- maximum extent in x and y (total veto) : 535.4 cm x 502.0 cm
- active veto area : 23.642 m^2
- maximum extent in x and y (active veto) : 413.0 cm x 502.0 cm
- number of long scintillators : 38
- number of short scintillators : 15
- number of photomultiplier tubes : 103

- number of TDC channels : 53
- typical efficiency : 96.5-97.5%
- time resolution : 0.3 ns
- typical dead-time due to veto : 3%

3.4 The Magnet

In order to measure the momenta of charged tracks the tracking devices have been placed in the recycled UA1 aluminum dipole magnet with an iron flux return (in the shape of "[ ]" known as C's). The support structure for the magnet also contains the hadronic calorimeter and the forward calorimeter.

Magnet Statistics :

- inner size of coil : 709.6 cm x 353.6 cm x 350.0 cm
- average field : 0.4 Tesla @ 5713 Amps
- field homogeneity : $\sim$ 2% (at center) to $\sim$ 10% (near edge)

3.5 The Drift Chambers

The NOMAD drift chambers act both as an interaction target and as our primary tracking medium. There are 11 modules of 4 chambers each forming the target region. There are 5 chambers positioned in the TRD region as well (see TRD

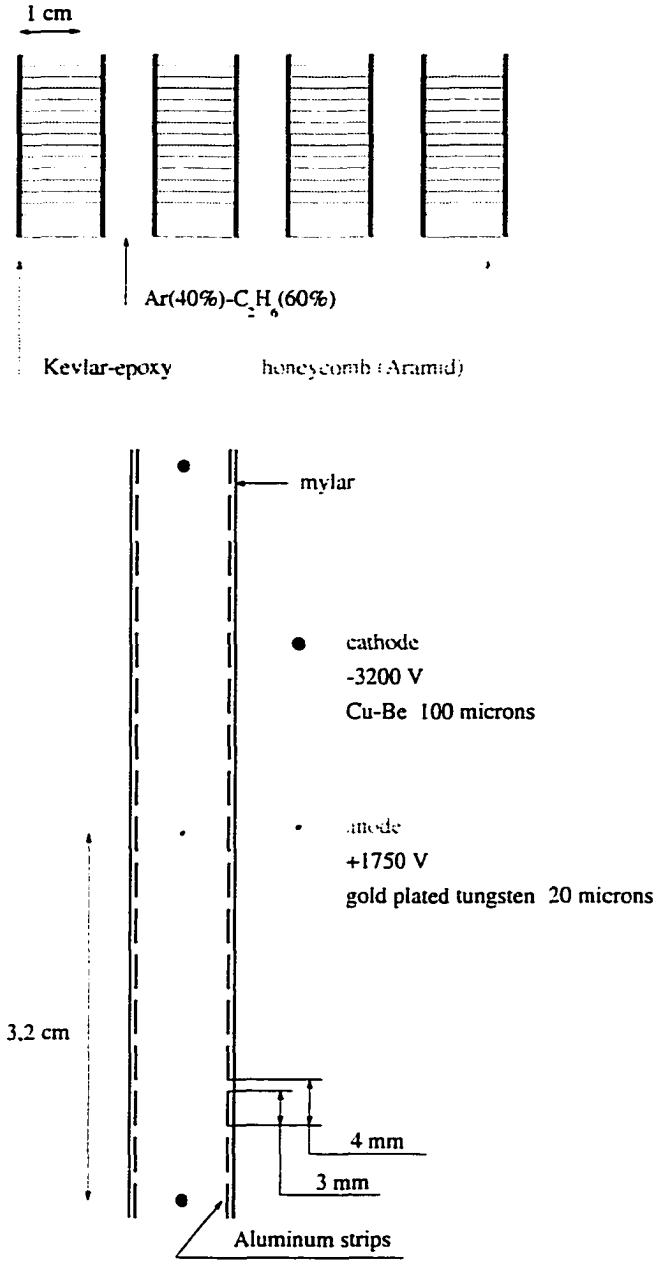

Figure 3.2: NOMAD Drift Chamber Overview.

section). Each chamber consists of three planes of sense wires at $-5°$, $+5°$, $0°$ with respect to the magnetic field which correspond to u, v, and y measurements, respectively. Four walls of Aramid fiber honeycomb covered with Kevlar-epoxy layers sandwich the wire planes (see Figure 3.2). These form the support walls of the chamber as well as providing the primary target material. The separation between anode wires is 6.4 cm with a cathode wire between each pair of anodes. Field shaping is provided by 3 mm wide aluminum strips, with 1 mm separation, glued to the chamber walls. The gas is an ethane-argon mixture with 60% ethane and 40% argon.

To help eliminate up-down ambiguity, the chambers are offset by ± 1.6 cm in y. The chambers are moved alternatively +1.6 cm (up) or -1.6 cm (down).

Drift Chamber Statistics :

- x range : -150.0 cm $\leq x \leq$ 150.0 cm
- y range : -150.0 cm $\leq y \leq$ 150.0 cm
- z range : 0.0 cm $\leq z \leq$ 404.0 cm
- covered x range : -135.0 cm $\leq x \leq$ 135.0 cm
- covered y range : -130.0 cm $\leq y \leq$ 130.0 cm
- covered z range : 0.0 cm $\leq z \leq$ 400.0 cm
- fiducial tonnage : 2.57 tons
- number of wires in y : 44

- number of wires in u and v: 41
- wire spacing : 6.4 cm
- wire length : 300.0 cm
- honeycomb and mylar thickness : 1.6 cm
- drift gap width : 0.8 cm
- radiation lengths per chamber : .02 X_o
- position resolution in x : $\sim$1500 μm per chamber
- position resolution in y : $\sim$250 μm per plane

3.6 The Trigger Planes

The trigger planes (see Figure 3.3) consist of two planes of scintillator counters, one before and one after the TRD region. Each plane is divided into two half planes consisting of 14 horizontal counters read out on one side only. The light guides of the horizontal counters are covered by 2 vertical counters in order to increase the fiducial area. A coincidence of hits in the two trigger planes with an anti-coincidence with the veto constitute the primary trigger.

Trigger Statistics :

- transverse area : 286.0 cm x 286.0 cm
- size of horizontal counters : 124.0 cm x 19.9 cm x .5cm

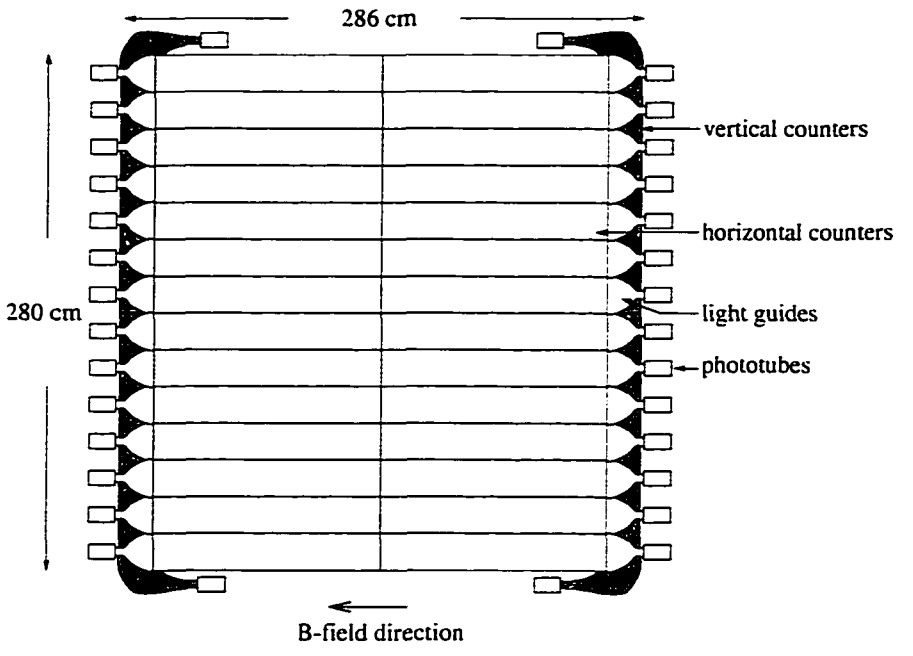

Figure 3.3: Front view of NOMAD Trigger plane.

- size of vertical counters : 130.0 cm x 19.9 cm x .5cm
- position of plane 1 : 408.3 cm
- position of plane 2 : 569.3 cm
- single counter efficiency : $\sim$ 98%
- CC trigger efficiency (from MC) : $\sim$ 98%
- NC trigger efficiency (from MC) : $\sim$ 83%

3.7 The Transition Radiation Detectors

The transition radiation detector (TRD) (see Figure 3.4) is used for identifying tracks as electrons. The TRD has 9 radiators, 9 straw tube planes and 5 drift

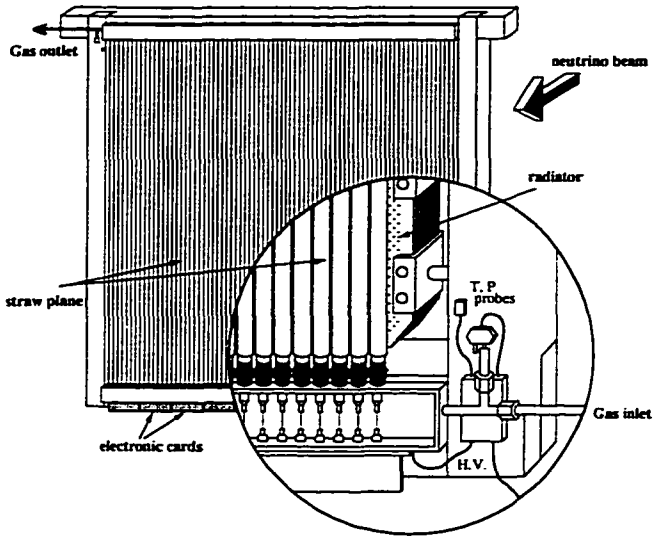

Figure 3.4: A TRD plane with a Detail of Inner Workings.

chambers. A module of TRD is a radiator followed by a plane of straw tubes. The drift chambers are placed after the modules #2, #4, #6, #8, and #9. The radiators themselves are made of 315 foils, 15 μm thick with 250 μm gas gap between foils. This gap is filled with nitrogen gas to prevent contamination from moisture and oxygen. A straw tube plane has 176 tubes per plane oriented vertically. The tubes are 3.0 m long made of 25 μm thick aluminized-Mylar tube. with an internal diameter of 1.6 cm. The sense wire is a 50 μm diameter tungsten wire. The tube is filled with 80% xenon and 20% methane. Consecutive planes are staggered to cover the dead area caused by the walls and space between tubes.

Overall, the TRD gives an e/π rejection factor of 10^3.

TRD Statistics :

- position of first module : 412.3 cm
- overall dimensions : 3.0 m × 3.0 m × 0.8 m
- number of radiators : 9
- number of foils per radiator : 315
- foil material : polypropylene
- foil thickness : 15 μm
- gap between foils : 250 μm
- foil gap medium : nitrogen gas
- radiation length of radiator: 0.1 X_o
- number of straw tube planes : 9
- number of tubes per plane : 176
- length of tube : 3.0 m
- inside diameter of tube : 1.6 cm
- diameter of wire : 50 μm
- wire material : tungsten
- tube medium : 75% xenon, 25% methane
- tube wall thickness : 25 μm
- tube wall material : aluminized-Mylar

3.8 The Preshower

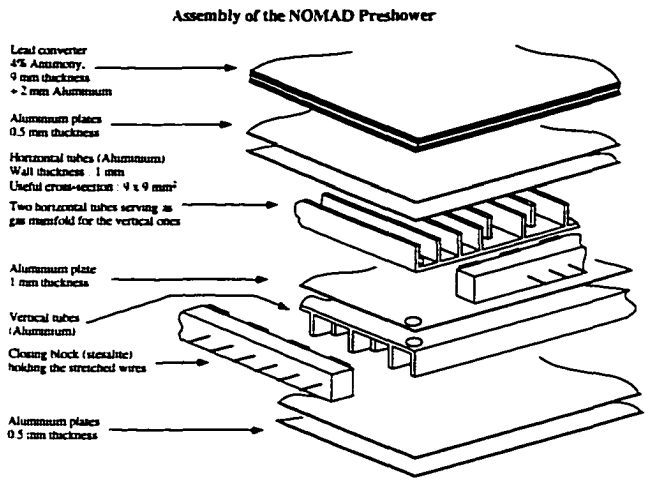

Figure 3.5: Detail of the Preshower.

The NOMAD preshower (see Figure 3.5), located just upstream of the electromagnetic calorimeter, is used to aid in the identification of electrons and electromagnetic showers in the ECal. It is also used in the identification of photons. It consists of two lead-antimony (4% Sb by weight) sheets hanging on either side of a 2.0 mm thick Al sheet, followed by two planes (horizontal and vertical) of 290 proportional tubes of which 286 are active in the horizontal direction and 288 are active in the vertical direction. The gas is .80/.20 argon-CO_2.

Preshower Statistics :

- transverse size : 292.1 cm x 290.1 cm
- cross-sectional size of tubes : 1.0 cm x 1.0 cm, internal size 0.9 × 0.9

mm^2

- length of horizontal tubes : 291.1 cm
- length of vertical tubes : 288.7 cm
- transverse size of lead sheet : 288.0 cm x 288.0 cm
- thickness of each of two lead sheets : 0.45 cm
- front face of lead position : 575.8 cm
- radiation length : 1.6 X_o
- interaction length : 0.05 λ

3.9 The ElectroMagnetic Calorimeter

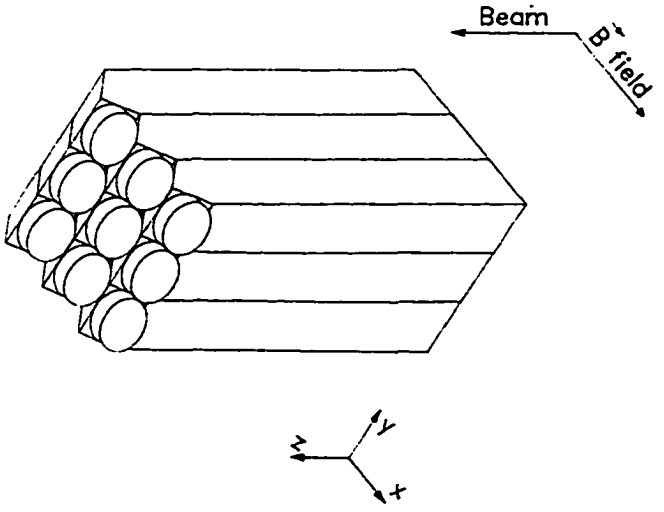

Figure 3.6: View of ECAL Lead Glass with Photoelectrodes.

The NOMAD electromagnetic calorimeter is used to identify electrons and photons and to measure their energy. It consists of 875 (35 rows of 25 towers) TF1-000 rectangular lead glass blocks (see Figure 3.6), each equipped with 3-inch Hamamatsu photoelectrodes of type R2186. The photoelectrodes are coupled to the block with a tilt of 45° with respect to the magnetic field direction and the axis of the block. Each block is monitored by two LEDs on opposite corners of the slanted face of the tower. The calibration was done in November 1993 and moved to NOMAD assuming that the LED signals remain the same.

ECal Statistics :

- transverse size : 280.0 cm x 277.0 cm
- transverse size of block : 11.2 cm x 7.9 cm
- block length : 49.4 cm
- front face position : 582.3 cm
- weight : $\sim$ 20 tons
- photoelectrons/GeV (B off) : $\sim$ 1200
- photoelectrons/GeV (B on) : $\sim$ 950
- minimum ionizing signal : 0.55 GeV
- GeV/ADC count : $\sim$ 0.025 GeV
- radiation length : 19.8 X_o
- interaction length : 1.6 λ

- energy resolution $\sigma/E = 0.0085 + 0.03/\sqrt{E(\mathrm{GeV})}$

3.10 The Hadronic Calorimeter

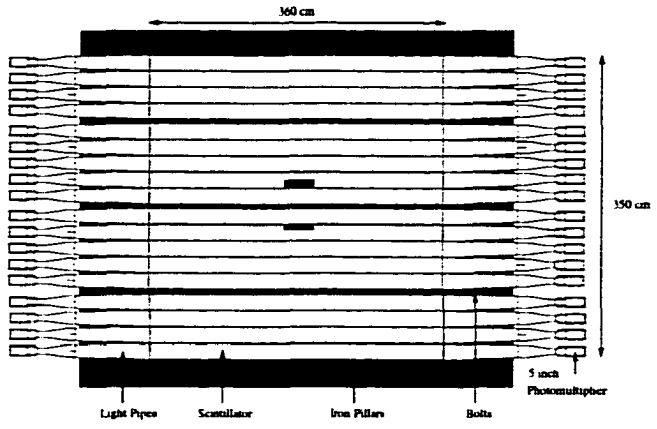

Figure 3.7: Front View of NOMAD Hadronic Calorimeter.

The NOMAD hadronic calorimeter (see Figure 3.7) is used to measure energy of neutral hadrons and to help identify electrons and muons. It is a sampling calorimeter downstream from the ECal and the magnet coil in the slotted iron. It consists of 11 steel planes and scintillator counters. The 11 counters in each plane are ganged together and read out by a single photo-tube on each side. Each active plane contains 18 counters. There are two notches in counters 8 and 11 (counting from the bottom up) to provide for bolts which support the cradle. The hadronic calorimeter was installed for the 1995 run.

HCal Statistics :

- transverse area : 360.0 cm x 350.0 cm
- thickness of iron plane : 4.9 cm
- length of a counter : 360.0 cm
- thickness of counter : 1.0 cm
- height of standard counter : 18.3 cm
- height of counter 7 & 8 : 21.9 cm
- height of counter 9 : 10.6 cm
- height of counter 10 : 13.6 cm
- position of front face : 710.6 cm
- interaction length : 3.2 λ
- energy resolution $\sigma/E = .965/\sqrt{E(\mathrm{GeV})} + 0.140$

3.11 The Muon Chambers

The NOMAD Muon Chambers (see Figure 3.8) are used to identify tracks as muons. They are 5 modules salvaged from the UA1 muon system. Each module consists of 2 chambers (one oriented horizontally and one vertically). Each chamber consists of 48 long tubes oriented along the length of the chamber and 73 short tubes oriented along the width with anode wire centrally positioned. The tubes are stacked in two rows one behind the other offset by half a tube. Modules 1-4 are oriented vertically and module 5 is oriented horizontally. Modules 1, 2

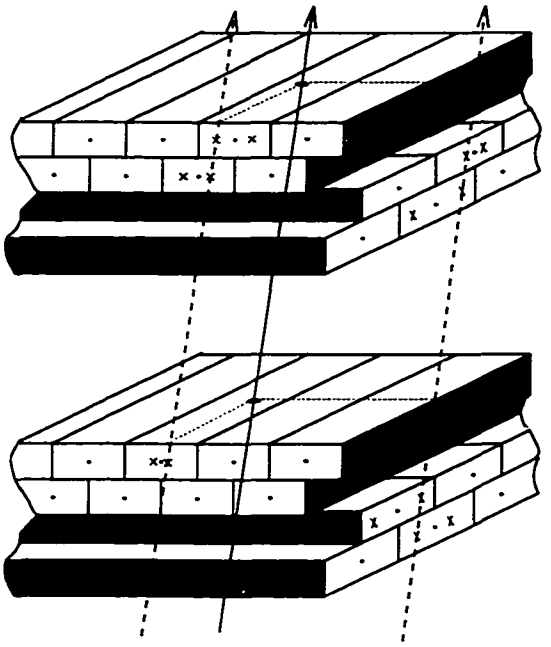

Figure 3.8: Cut Through View of NOMAD Muon Chambers with a Typical Hit Pattern for a Through Going Muon (solid line) and Reconstructed Projections (dashed line).

and 5 are located in front of an iron absorber wall. Modules 3 and 4 are located behind the wall. The gas is argon:ethane, 40:60.

Muon Chamber Statistics :

- transverse size of chamber : 375.0 cm x 555.0 cm
- length of long tube : 555.0 cm
- length of short tube : 375.0 cm
- transverse size of tube : 14.9 cm x 4.4 cm
- position of module 1 x,y,z : -172.5 cm, -135.0 cm, 907.3 cm
- position of module 2 x,y,z : 172.5 cm, -135.0 cm, 945.3 cm
- position of module 3 x,y,z : -172.5 cm, 0.0 cm, 1144.3 cm
- position of module 4 x,y,z : 172.5 cm, 0.0 cm, 1182.3 cm
- position of module 5 x,y,z : 0.0 cm, 363.0 cm, 926.3 cm
- thickness of iron wall : 80.0 cm
- transverse area of wall : 720.0 cm x 640.0 cm
- resolution .25 mm for 0° track, .50 mm for 40° track

3.12 The Neutrino Beam

Neutrinos are produced for NOMAD by the West Area Neutrino Facility (WANF) off the CERN SPS (see Figure 3.9) . Protons hit a beryllium target to produce

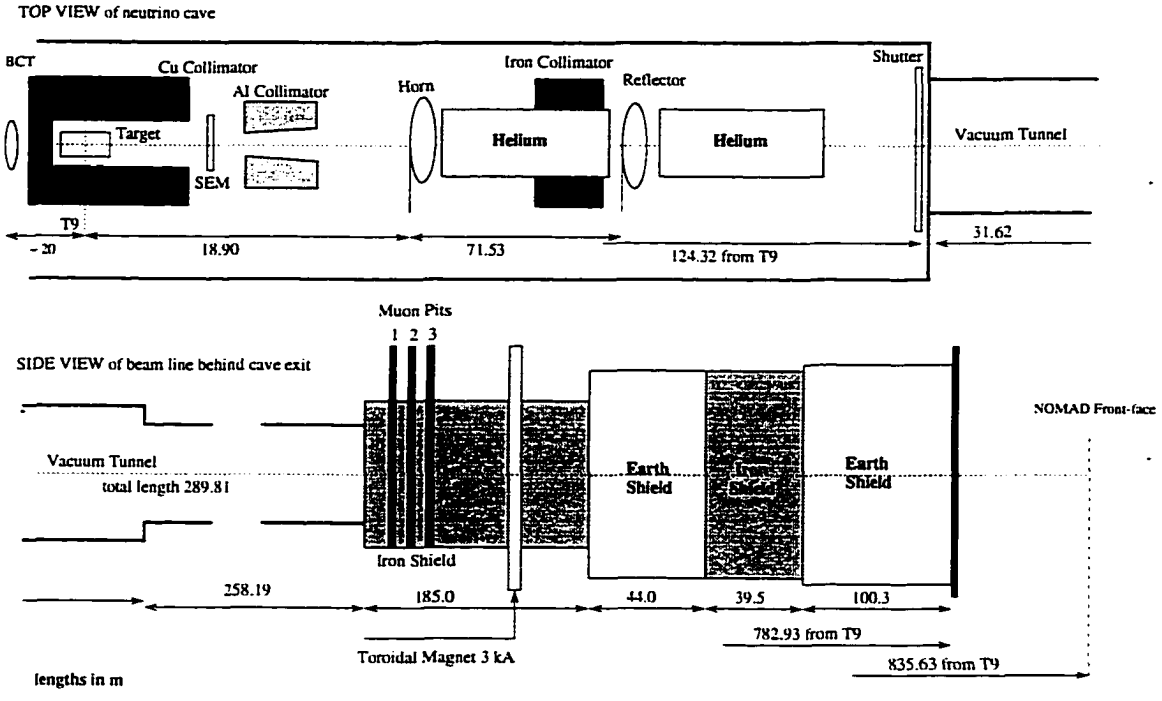

Figure 3.9: The West Area Neutrino Facility Layout.

pions and kaons which are allowed to decay in flight.

The SPS accelerates protons to an energy of 450 GEV and extracts them to experiments on a cycle of 14.4 s. Twice per cycle approximately 10^{13} protons are extracted from the SPS for neutrinos over a 4 ms spill separated by 2.6 seconds. The protons impinge on a series of 11 colinear 10cm long, 3mm diameter beryllium rods each separated by 9 cm to produce primarily pions and kaons. A copper and an aluminum collimater absorb particles coming off the target at high angles.

Positive secondaries are then focused through a pair of magnets, horn and reflector. Each carry equal amounts of current in opposite directions and are synchronized to have maximum current during the neutrino spills of the SPS cycle. The areas between the horn and the reflector and the area between the reflector and the decay tunnel are filled with helium to minimize the absorption of the secondaries. Also between the horn and the reflector there is an iron collimator to catch defocused negative secondaries to further reduce the production of anti-neutrinos.

The focused secondaries then fly into a 290m long vacuum tunnel where they are allowed to decay. The decay tunnel is followed by 370m of earth and iron shielding to absorb non-neutrino secondaries. In the shielding there is a toroidal magnet that refocuses muons back into the shielding for further absorption. All surviving particles then reach the BEBC hall which contains the NOMAD and CHORUS detectors.

The beam is monitored in three ways. First, in front of the target there is a

pair of beam current transformers (BCT) which measures the flux of incoming particles. The SEM, just downstream of the target, measures the flux of secondary particles. Thirdly, in the iron shielding following the decay tunnel, there are three "muon pits" containing arrays of small silicon strip detectors which give a measure of the absolute muon flux.

Chapter 4

Event Selection and Reconstruction

4.1 Data Acquisition

The NOMAD DAQ is synchronized with the SPS cycle in order to accept triggers during the two windows of the neutrino spills. The trigger, during the neutrino spills for acceptance of neutrino events in the main detector, is formed by a coincidence of hits in the two trigger planes and an anti-coincidence with the veto. During the flat-top between neutrino spills the trigger is formed by a coincidence of hits in the trigger planes and the veto in order to record muons for calibrations.

NOMAD uses three different types of FASTBUS modules for digitizing signals from the various sub-detectors. Two different kinds of 12-bit ADC are used, one

peak sensing and the other charge integrating, as well as a 16-bit TDC with 1 ns resolution. Digitized information is buffered internally by the FASTBUS electronics and then read out at the end of each spill in order to reduce dead-time.

Five VME-based cards control all the FASTBUS electronics and group all the data into sub-events. These sub-events are then assembled along with other beam information by another VME-card, the event-builder, to form a complete event. Events are stored on a local disk and then written to high-density tapes twice a day.

A monitoring program is running to insure that data quality is acceptable. This program produces a standard set of histograms for each sub-detector and the beam which are constantly ignored by people on shift for comparison with a set of template histograms to see any deviations from normal.

4.2 Event Filtering

There are problems reconstructing events with large amounts of detector activity. The first set in the filter pre-selection is to reject events which have a hit density of larger than 12 hits per plane. Events which pass this cut are run through the track and vertex reconstruction program.

After this, events are passed through a loose filter. This filter rejects events which have a vertex outside of the target region or those with fewer than two

tracks. An intermediate filter then selects events which have at least one track with momentum greater than 0.5 GeV/c and have the primary vertex downstream from the first trigger plane.

4.3 Event Reconstruction

4.3.1 Track and Vertex Reconstruction

Track finding and fitting [25] is conducted in four stages. First, triplets are formed. A triplet is a set of three hits in adjacent u-v-y planes which are determined to be geometrically compatible. If a group of three triplets is found then a helix can be fit to them. After a helix is fit, a search is conducted down a road along that helix for additional hits. Finally, all the hits are fitted to a helix and position, curvature and direction of the helix may be estimated. The helix fit is done via a Kalman filter which takes into account variations in magnetic field and multiple scattering.

A version of the Kalman filter is used in fitting tracks to vertices [26]. This allows for a fast fit as well as a simple means of adding or removing tracks without completely refitting the vertex. Once tracks are associated with a vertex the track parameters (ie momentum and position) are fit for that vertex. We consider three classes of vertices:

- The primary vertex is the most upstream vertex.

- A V0 vertex is a vertex from which the invariant mass is of a known neutral (ie a γ, K_s or a Λ).

- A secondary vertex is any other vertex with more than one track. It can have an incoming track associated with it.

- Tracks not associated to a vertex are referred to as hanging tracks.

4.3.2 ECal Clustering

There are two kinds of electro-magnetic clusters, charged clusters and neutral clusters. Charged clusters are energy in the ECal associated with a track and neutral clusters are energy in the ECal not associated with a track.

In order to find clusters in the ECal, tracks found in the drift chambers are extrapolated to the ECal. The ECal block that is at the extrapolated point is taken as the cluster seed. Blocks within a predetermined rms distance to the seed are added to the cluster. Blocks shared by two clusters share energy weighted by the energy of the cluster.

Neutral clusters are then formed. The remaining unused block with the highest energy is taken as the seed for a neutral cluster. Blocks within a predetermined rms distance to the seed are added to the cluster. The process is continued until there are no blocks unassociated with a cluster.

Chapter 5

Event and Detector Simulation

Central to this study is the ability to predict the number of signal and background events that are to be observed in the detector and what they will look like. In order to do this at NOMAD, several computer simulations using the Monte Carlo method have been written in order to have an output that has a format which is identical to that of the data.

The simulation of the data sample is done in three steps. First, the beam line is simulated in order to determine the neutrino energy spectrum. Secondly, the interaction of the neutrino with the detector is generated. Lastly, the detectors response to the generated interaction is produced. We will discuss these three steps here.

5.1 Beam Simulation

The simulation of the neutrino beam at NOMAD is performed by a Monte Carlo simulation program called NUBEAM. NUBEAM is based on the GEANT [27] package developed at CERN and the hadronic interaction package FLUKA92 [28]. NUBEAM takes 450 GeV protons, impinges them on the beryllium target, using FLUKA to simulate the interaction and generate the secondary particles. then propagates the secondaries through the beam line to the detector using a detailed GEANT simulation. From this we can get the spectra and radial distributions for the various neutrino species (see Figures 5.1 and 5.2.)

The main uncertainty in the beam composition arises due to our lack of knowledge of the relative pion and kaon production rates at the initial proton-beryllium interaction. This is particularly problematic in this case as ν_e arise almost exclusively from kaon decays. This uncertainty is currently under investigation by the SPY [29] collaboration who are studying pion and kaon yields in proton beryllium interactions at the same energies as NOMAD.

For this analysis not only is an accurate knowledge of the neutrino spectrum necessary but it is also necessary to know how well the beam spectrum is known. The flux from NUBEAM is therefore supplemented by an empirically derived spectrum. This measurement was done by Mishra and Das [30]. In this measurement, the differential cross section for secondary hadron production for the

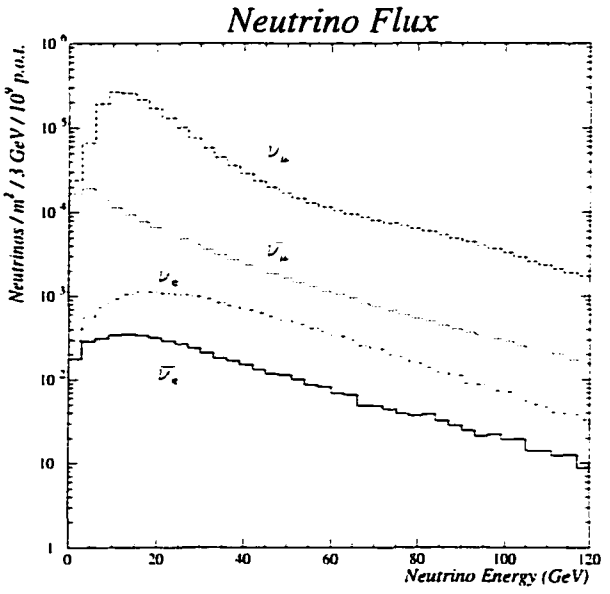

Figure 5.1: Neutrino Flux Predicted by NUBEAM.

proton-beryllium interaction is expressed as:

$$\frac{d\sigma}{dx_F dP_T^2} = C \times f(x_F) \times g(P_T) \times h(x_F, P_T), \tag{5.1}$$

where $x_F = p/p0$, $p0$ is the energy of the primary proton (450 GeV), p is the energy of the secondary meson, and f, g, h are functions of the two Feynman variables. The functions f, g, h are then determined empirically for different hadronic secondaries from the flux of different neutrino species at NOMAD. The ratio of K^+/π^+ can be predicted from measuring the ν_μ flux. Measuring the $\overline{\nu_e}$ flux can predict the contributions in the beam from K_L^0. The K^-'s and μ^-'s can be determined from the $\overline{\nu_\mu}$ flux. From, this a prediction of the ν_e flux is made to a level of 2.7% accuracy.

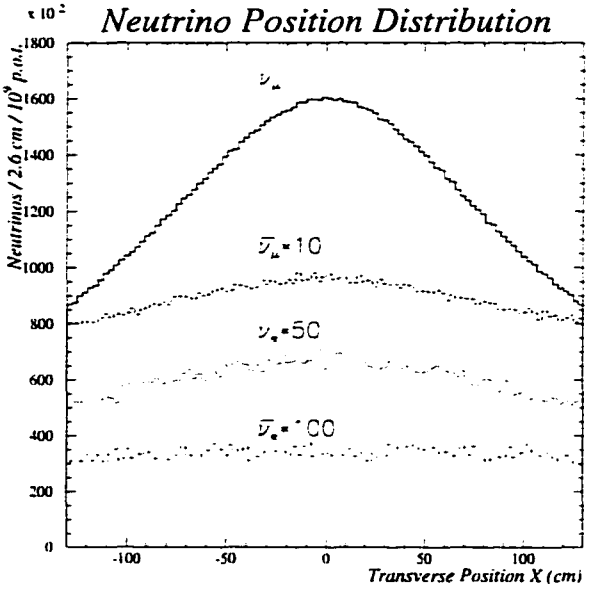

Figure 5.2: Neutrino Radial Distribution Predicted by NUBEAM.

5.2 Neutrino Event Generation

The neutrino interation in the detector is generated with the program NEGLIB [31]. NEGLIB takes the output of NUBEAM to generate a position and energy for the event vertex. The material density distribution in the target is also taken into account in generating the vertex position. NEGLIB then simulates deep inelastic neutrino-nucleon scatters using the LEPTO [32] package. LEPTO uses leading order standard model electroweak cross sections and first order QCD corrections for the parton level interaction. The Lund string model is used for hadronization. NEGLIB also simulates Fermi motion of the struck nucleon.

5.3 Detector Simulation

In order to simulate the detector's response to the neutrino event, a GEANT based program, GENOM[33], is used. GENOM tracks individual particles as they step through the material of the detector and simulates their interactions therein. GENOM takes into account electro-magnetic and strong interactions as well as decays of unstable particles. Strong interactions are simulated using the FLUKA and GHEISHA [34] packages depending on which part of the detector the particle happens to be in. FLUKA is used in the tracking section and GHEISHA is used in the calorimetric sections. When a particle travels through an active region of the detector, GENOM simulates the response and outputs in a format which is identical to the data.

Chapter 6

ν_e Analysis

6.1 Event Selection

6.1.1 Data Sample

The data sample used was taken in 1995. Due to various technical difficulties during some of the data taking period, only a portion of the commissioned drift chamber modules were present. This data sample was, therefore, taken in three different configurations: 4 DC modules, 8 DC modules and 11 DC modules. This data is reconstructed as described in Chapter 4. Monte Carlo samples of ν_e charged current interactions and ν_μ charge current and neutral current interactions were also generated as described in Chapter 5 and reconstructed as per Chapter 4. All Monte Carlo was generated with an 11 DC module configuration. Also, all Monte Carlo samples were generated using an old version of the

beam Monte Carlo called GBEAM. Reweight tables between GBEAM and the empirical parametrization have been used for translation.

6.1.2 Track Selection

Tracks were selected for an event if they meet one of the following criteria.

- A track is associated with the primary vertex.
- A track is associated with a V0 vertex.
- A track is associated with a secondary vertex that has no associated incoming track.
- A track is a hanging track that points back to within 20 cm in the x-y plane of the primary vertex.
- A neutral ECal cluster having energy greater than 120 MeV.

Neutral ECal clusters and V0's are called neutral tracks, while all other tracks will be referred to as charged tracks.

6.1.3 Vertex Selection

Events were selected if the reconstructed vertex was within ± 130 cm in both x and y and z was less than 404 cm. For 4 module data z was required to be greater than 260 cm, for 8 module data z was required to be greater than 113 cm, and for 11 module data z was required to be greater than 3 cm.

It was further required that the primary vertex have a minimum of two tracks associated with it.

Reweighting was done on Monte Carlo to deal with the fact that all Monte Carlo was generated in an 11 module configuration. Reweighting was done based on the relative number of protons on target for each of the three different configurations. The reweighting factors are given in Table 6.1.

Vertex z (cm)	*modules in range*	*p.o.t. available*	*correction factor*
$0 < z < 110$	1-3	3.0×10^{18}	.3488
$110 < z < 256$	4-7	6.0×10^{18}	.6977
$256 < z$	8-11	8.6×10^{18}	1.0

Table 6.1: 4, 8, and 11 Module Data Correction Factors [35].

Drift chamber inserts and glue strips, regions where the density differs from the rest of the chamber, were not simulated in the Monte Carlo. MC events were reweighted based on the simulated x and y positions by scale factors of 6 for inserts and 2.2 for glue strips as described in Table 6.2.

It can be seen that the vertex distribution in the data and the expectation from the Monte Carlo (including corrections) in Figure 6.1 agree well.

Vertex x (cm)	*Vertex y (cm)*	*correction factor*
-74.0< x <-66.5	-71.0< y <-63.0	6.0
-74.0< x <-66.5	-0.5 < y < 7.5	6.0
-74.0< x <-66.5	70.0 < y < 78.0	6.0
-2.0 < x < 6.0	-71.0< y <-63.0	6.0
-2.0 < x < 6.0	-0.5 < y < 7.5	6.0
-2.0 < x < 6.0	70.0 < y < 78.0	6.0
71.3 < x < 79.3	-71.0< y <-63.0	6.0
71.3 < x < 79.3	-0.5 < y < 7.5	6.0
71.3 < x < 79.3	70.0 < y < 78.0	6.0
-140 < x < 140	-51.3< y <-51.0	2.2
-140 < x < 140	-49.3< y <-49.0	2.2
-140 < x < 140	56.0 < y < 56.3	2.2
-140 < x < 140	59.0 < y < 59.3	2.2

Table 6.2: Correction Factors for Inserts and Glue Strips. The positions given are approximate only as they are extracted phenomenologically from the data, and do not necessarily reflect the true geometry [35].

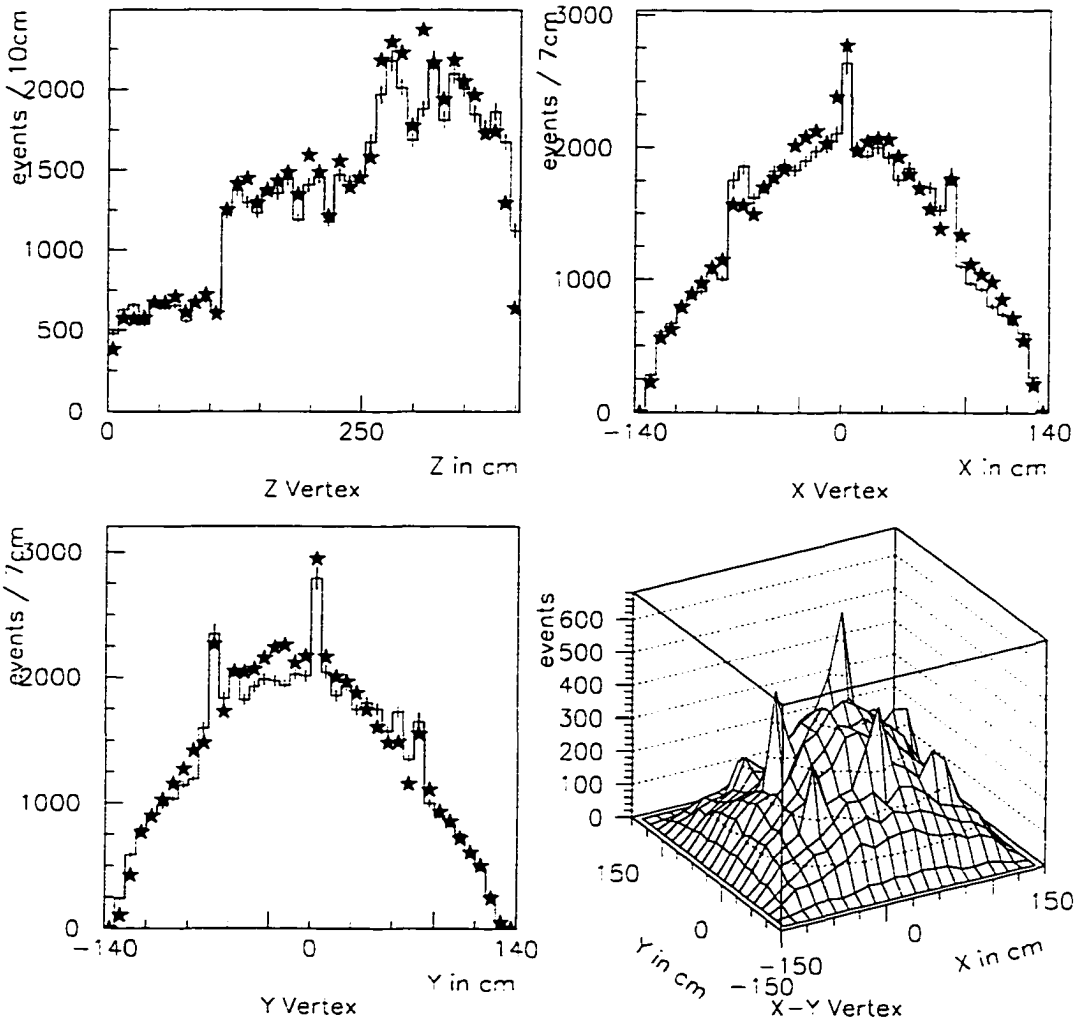

Figure 6.1: Vertex Distribution for Selected Events in cm. The solid line is the Monte Carlo and the stars are the data.

6.1.4 Leading Lepton Selection

Kinematical criteria were used to select the leading lepton in the event prior to any event selection. Three different methods for kinematical selection were investigated: selecting the charged track in the event with the maximum momentum in the lab frame, selecting the charged track in the event with the maximum momentum in the center of mass frame, and selecting the charged track in the event with maximum thrust. Monte Carlo efficiency studies showed that the second method was the most effective (see Table 6.3) overall and as a function of the event energy as is seen in Figure 6.2 and in Figure 6.3.

Method	Muon Efficiency	Electron Efficiency
Charged Track with Max p in Lab	.738	.706
Charged Track with Max p in CoM	.797	.759
Charged Track with Max Thrust	.755	.706

Table 6.3: MC Leading Lepton Selection Efficiencies.

6.1.5 Kinematic Selection

Neutral current (NC) events appear kinematically distinct from charged current (CC) events due to the fact that the final state neutrino is not observed. Nonetheless, neutral currents can appear in the charged current sample because leptons (either muons or electrons) can be produced in the hadronic shower of the event,

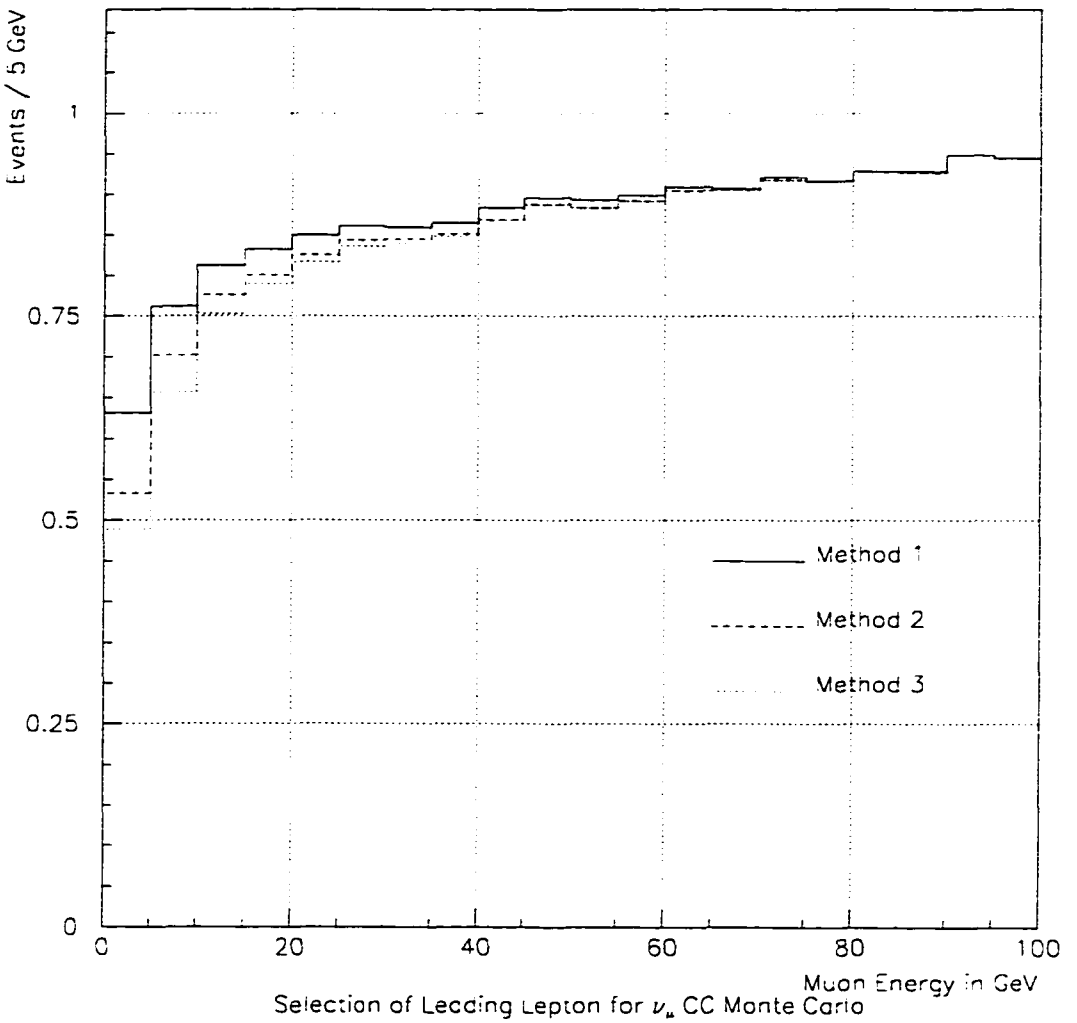

Figure 6.2: Lepton selection efficiency for ν_μ CC events vs. energy for the three methods described in the text. Method one is selection of the charged track with the highest momentum in the COM frame. Method two is selection of the charged track with maximal thrust in the lab frame. Method three is selection of the charged track with maximum momentum in the lab frame.

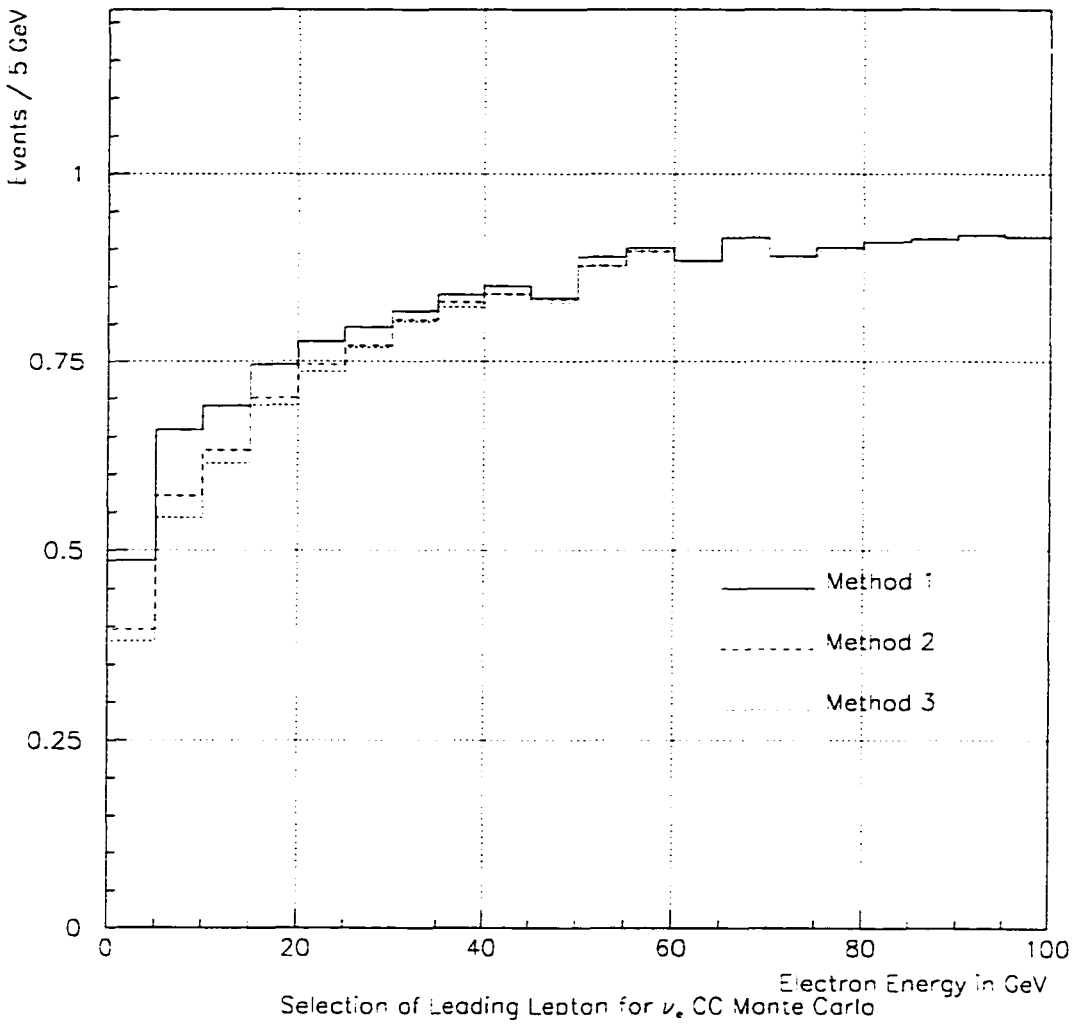

Figure 6.3: Lepton selection efficiency for ν_e CC events vs. energy for the three methods described in the text. Method one is selection of the charged track with the highest momentum in the COM frame. Method two is selection of the charged track with maximal thrust in the lab frame. Method three is selection of the charged track with maximum momentum in the lab frame.

either from interactions or decays of the shower products. Also hadrons in the shower may be misidentified as leptons. In order to minimize this background in the data sample, cuts were made on the momentum of the final state lepton with respect to the total reconstructed momentum (Q_t), the transverse reconstructed momentum with respect to the beam direction (p_t), the momentum transferred (Q^2), the invariant mass of the hadronic system (W^2) and the distance from the vertex to the first point of the reconstructed lepton track (Δz), as stated below.

- $Q_t > 1.0$ GeV
- $p_t < 2.5$ GeV
- $\Delta z < 15$ cm
- $Q^2 > 2$ GeV^2
- $W^2 > 5$ GeV^2

Q_t for neutral currents will tend to be small, as the lepton track comes from the hadronic shower, compared with CC events where the lepton and hadron are more separated, as can be seen in Figure 6.4.

In NC events there are large amounts of missing transverse momentum due to the fact that the final state lepton (a neutrino) was not measured, whereas in CC events it was, as can be seen in Figure 6.5.

A cut was performed on Q^2 and W^2 to get rid of certain non-scaling processes which were not well simulated.

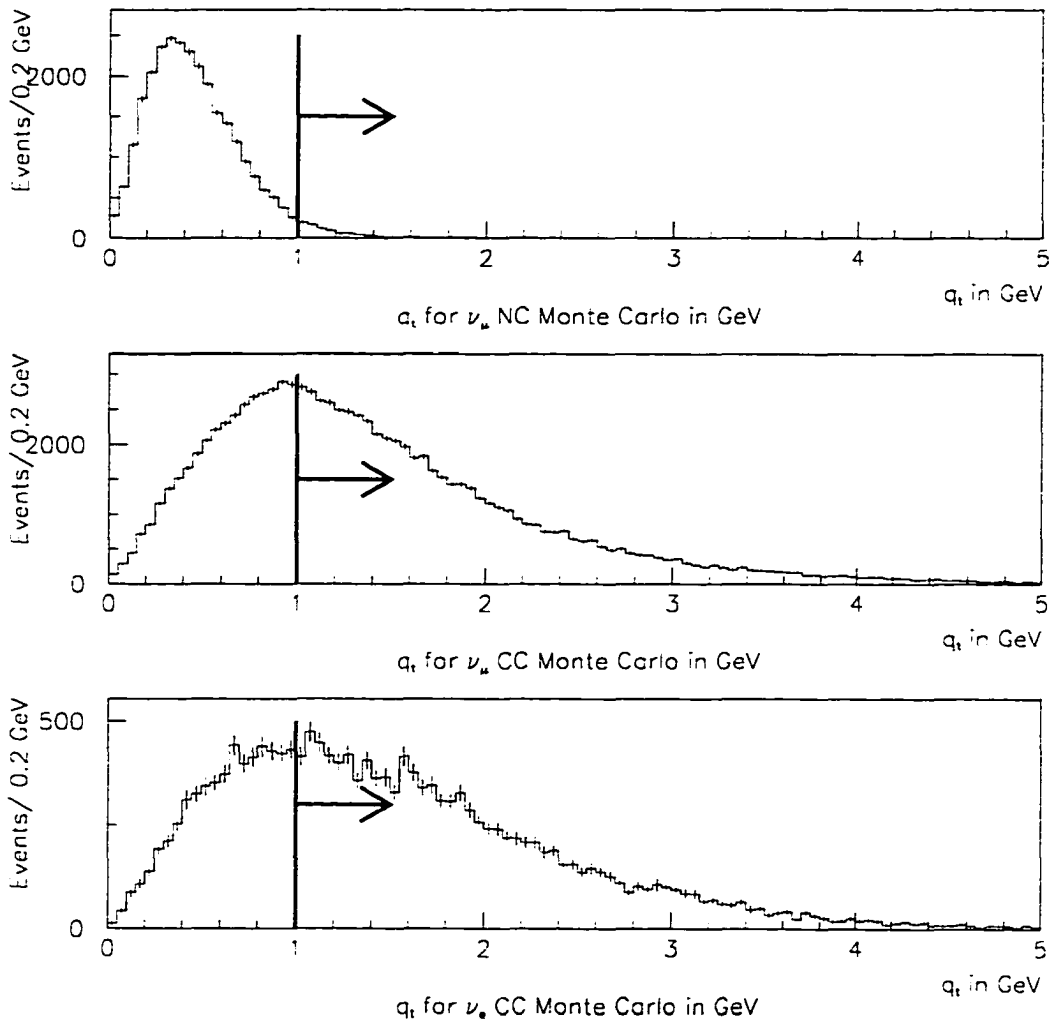

Figure 6.4: Q_t for ν_μ CC, ν_μ NC, ν_e CC Events with Selection Cut.

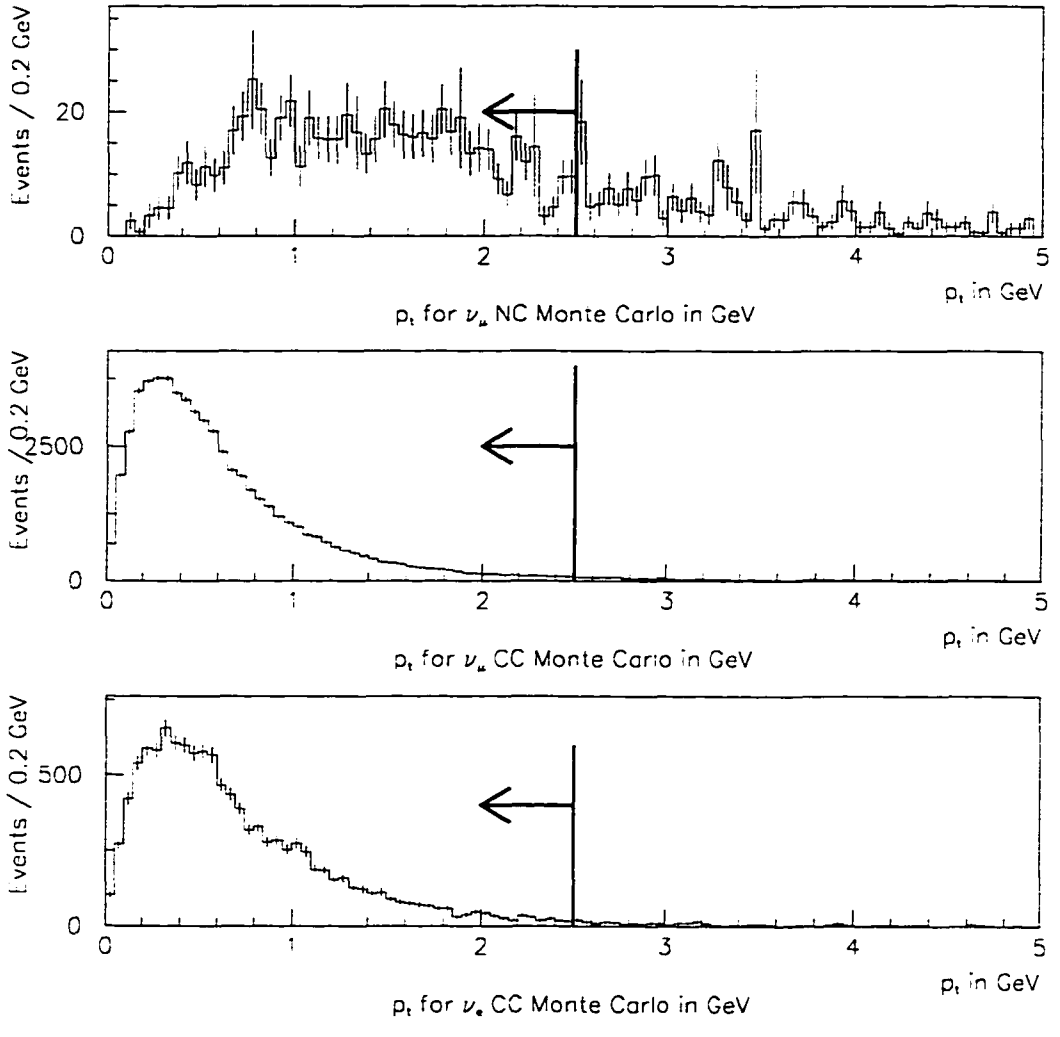

Figure 6.5: p_t for ν_μ CC, ν_μ NC, ν_e CC Events with Selection Cut.

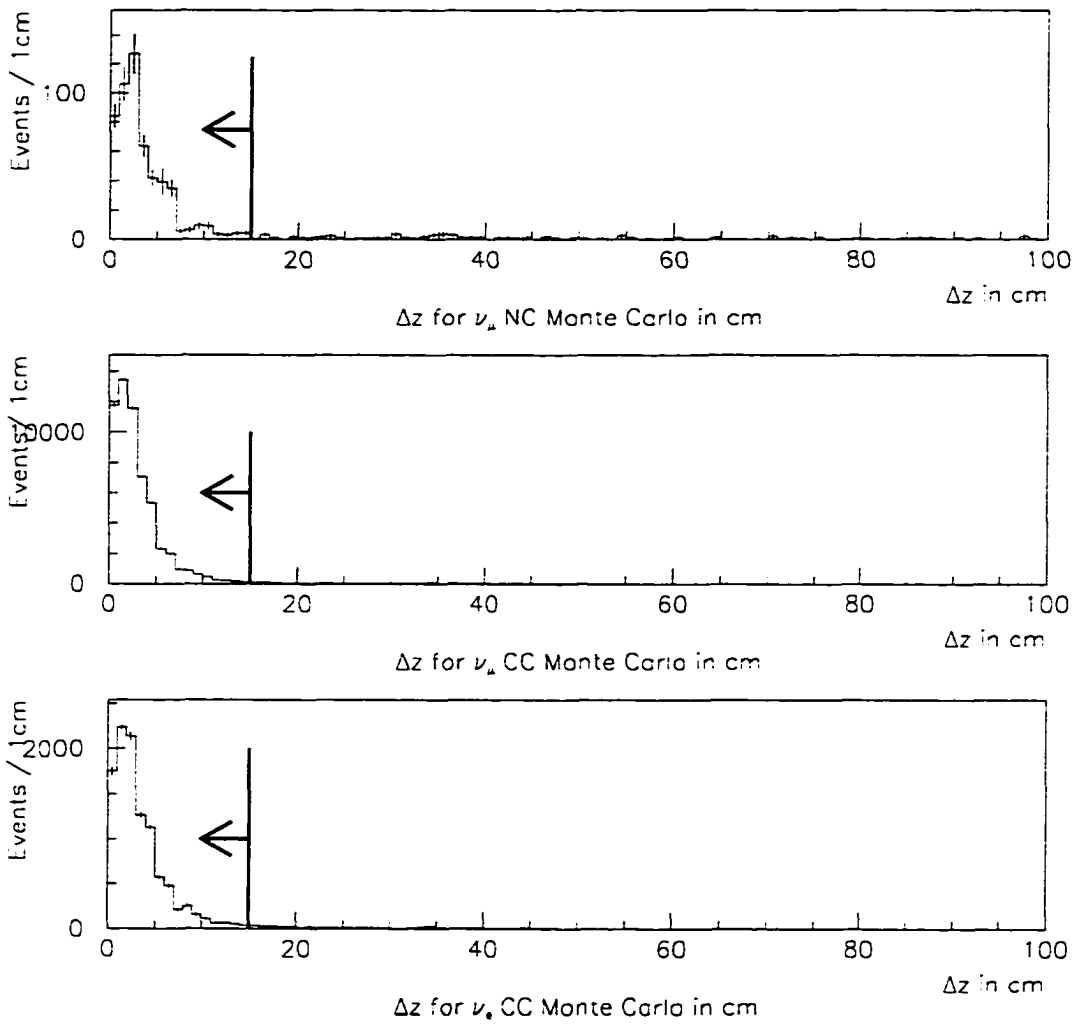

Figure 6.6: Δz for ν_μ CC, ν_μ NC, ν_e CC Events with Selection Cut.

Finally, the cut on Δz was performed because misidentified leptons from photon conversions or decays will tend to be separated from the primary vertex. The effect this selection cut has can be seen in Figure 6.6.

6.2 The Q_t Cut

The Q_t cut was the major cut to reduce the neutral current background in this event sample. However, as can be seen in Table 6.4 and Table 6.5, it also reduces the charged current sample significantly. In order to see that the Q_t cut was optimized, the final sensitivity was studied to see how it shifts for different values of cuts on Q_t and p_t. The sensitivity is defined to be the limit that would be set with the available statistics if the Monte Carlo and data samples agreed perfectly. The method used for calculating the limit is described further in the text.

In Figure 6.7 it can be seen that the final sensitivity does not depend very strongly on p_t but is affected by variations in Q_t. In fact looking at this plot the choice made for the value of the cut of 1.0 GeV seems questionable. A choice of 0.9 or 0.8 gives a better sensitivity. The calculation of the sensitivity assumes that the signal and background are perfectly understood. Unfortunately, this is not the case. As can be seen in Figure 6.8, if the neutral and charged current ν_μ background level exceeds 5% in the ν_e sample, there is a strong systematic shift in $\sin^2(2\theta)_{BEST}$, thus indicating a misunderstanding of these background levels. The Q_t cut was therefore chosen to keep these levels low in order to avoid this

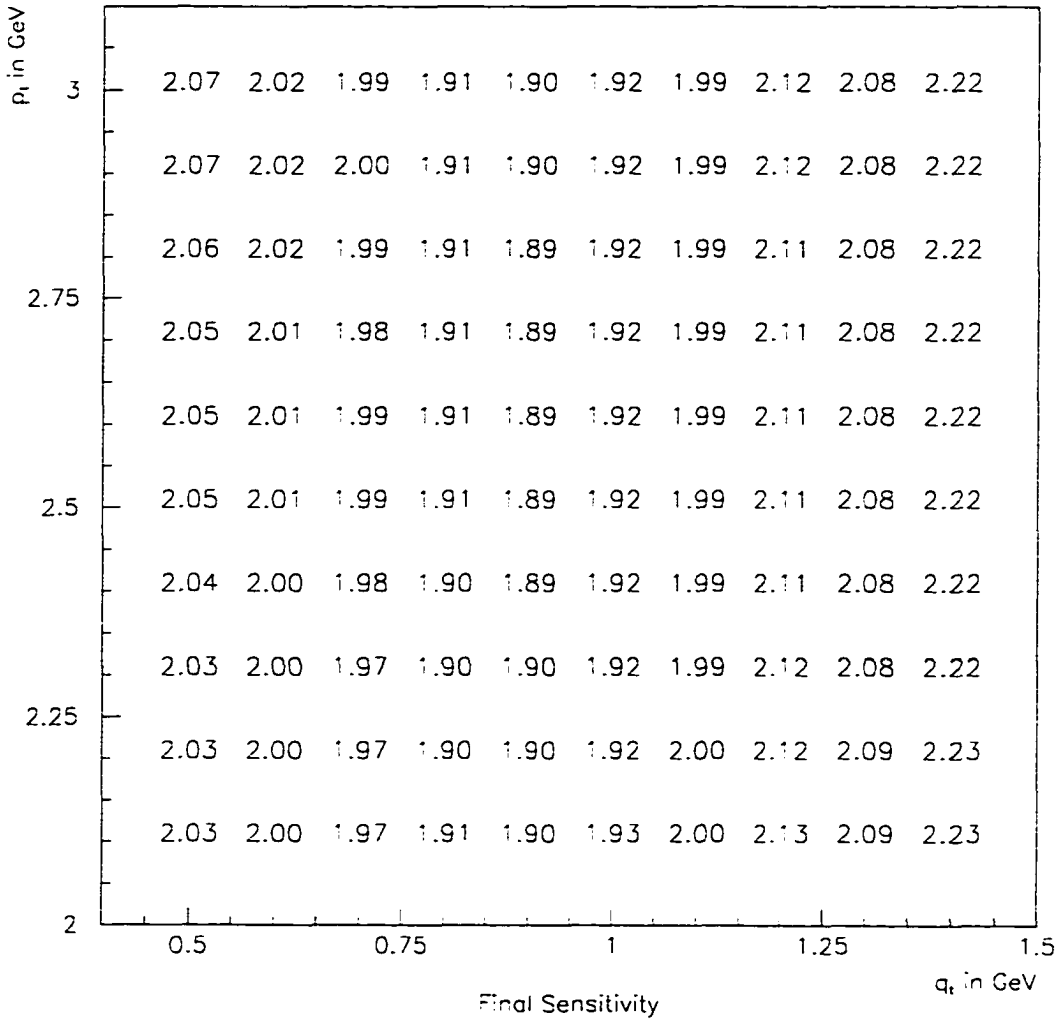

Figure 6.7: Final Sensitivity of the Measurement for Different Values of Q_t and p_t in GeV. The sensitivity is given in units of 10^{-3} and is calculated for a value of Δm^2 of 1000 eV^2/c^4.

poorly understood region.

In Figure 6.9 it can be seen that by moving into a completely different piece of $Q_t - p_t$ space to make a cut where the p_t cut is dominant, for example, a choice of 0.6 GeV for Q_t and 1.6 GeV for p_t does not give a better sensitivity. In fact, having the p_t cut dominate tends to reduce the ν_e sample while maintaining a similar amount of background, as can be seen in Figure 6.10.

6.3 Lepton Identification

The particle type of the leading charged particle was determined to set the incoming neutrino flavor, i.e., if the leading particle was an electron the event is classified as a ν_e, if the leading particle was a muon the event is classified as a ν_μ, and if it is neither the event was ignored. Particle identification was done using information from the transition radiation detector, the preshower, the electromagnetic calorimeter, and the muon chambers.

6.3.1 Electron-Pion Rejection with the TRD

For each track an association with hits in the TRD based on proximity was made. Electron identification was then done using a measurement of the total charge deposited in each straw tube associated with the track. The electron signature was determined through a likelihood ratio method [36]. A variable

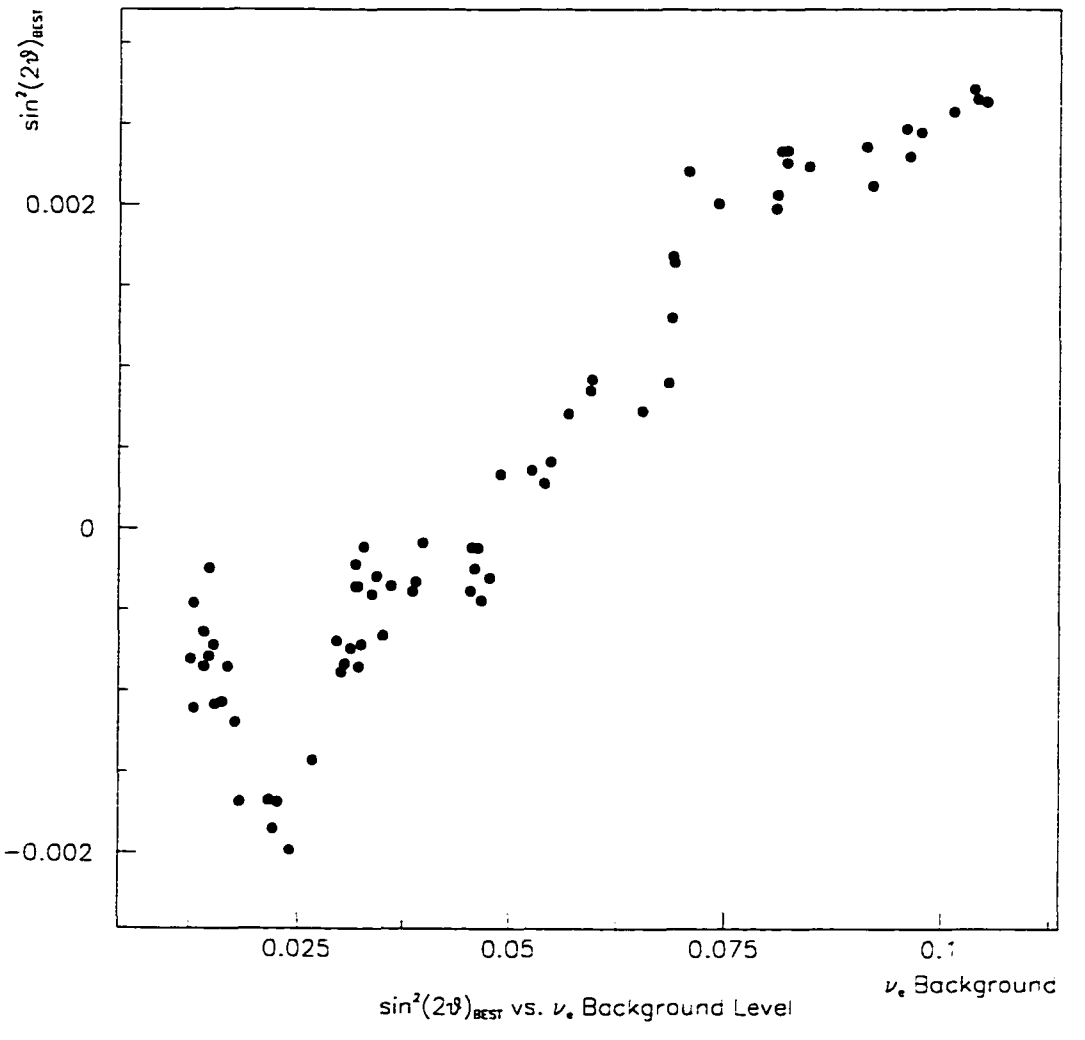

Figure 6.8: $\sin^2(2\theta)_{BEST}$ vs. the Percentage of Background from CC and NC ν_μ to the ν_e Spectrum. $\sin^2(2\theta)_{BEST}$ is calculated for a value of Δm^2 of 1000 eV^2/c^4.

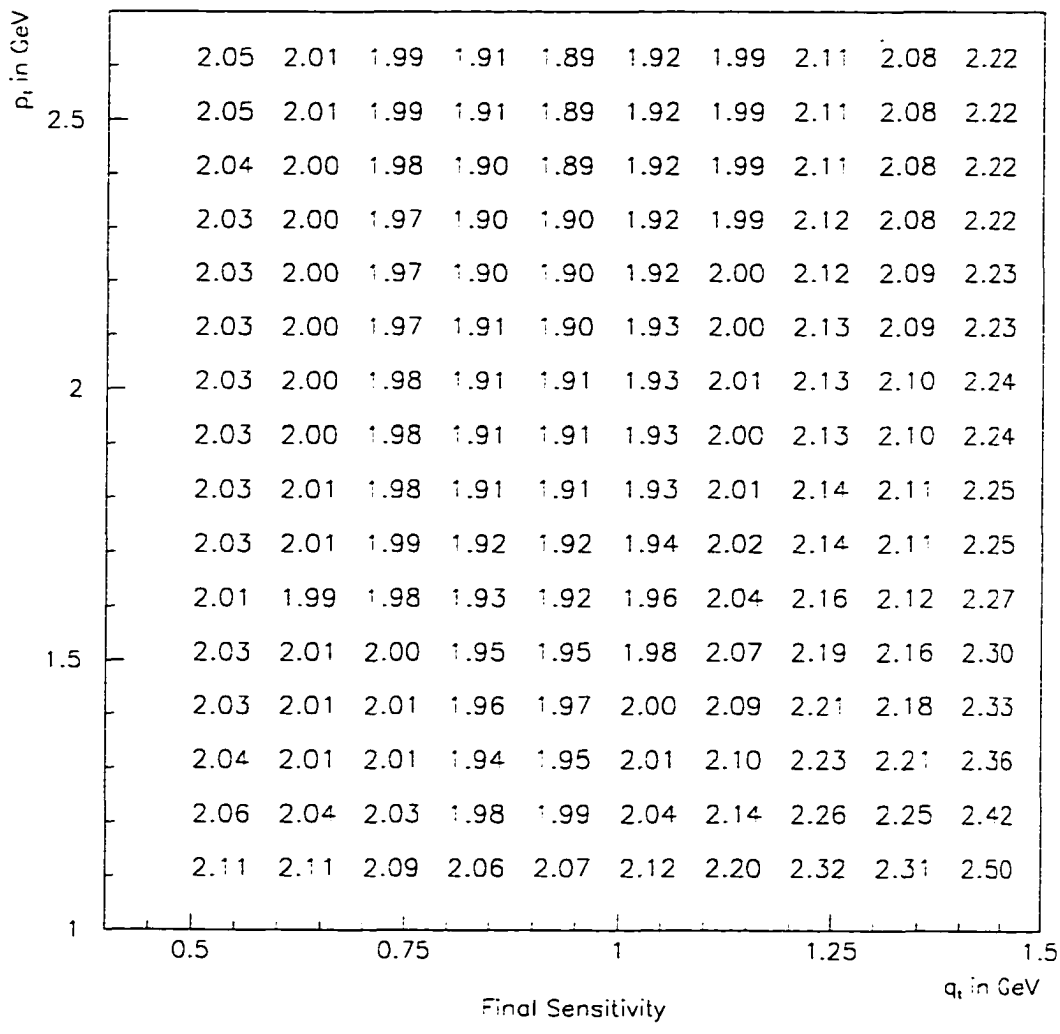

Figure 6.9: Statistical Sensitivity of the Measurement for Different Values of Q_t and p_t in GeV. The sensitivity is given in units of 10^{-3} and is calculated for a value of Δm^2 of 1000 eV^2/c^4.

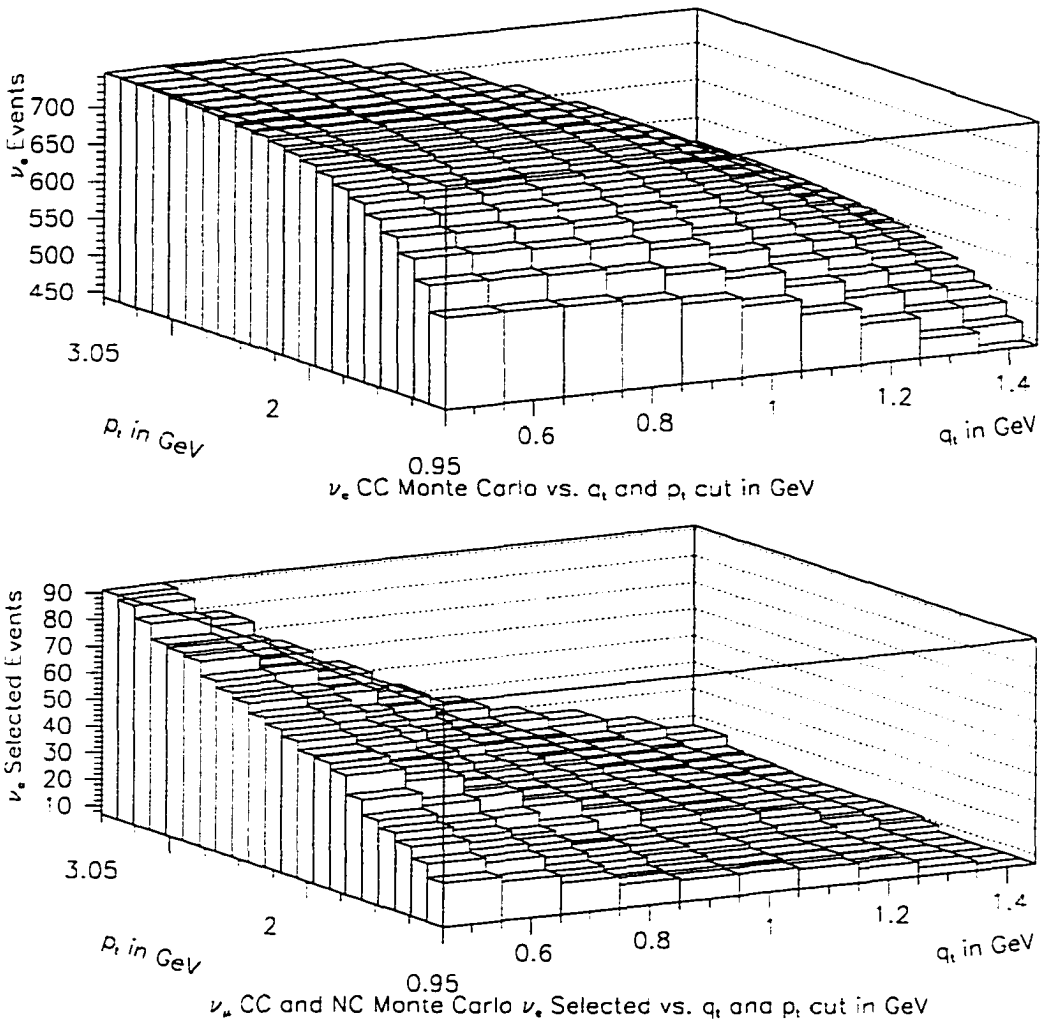

Figure 6.10: ν_e Selected Events for Different Values of Q_t and p_t in GeV. The top plot shows the ν_e CC events selected and the bottom shows the level of background from ν_μ CC and NC.

called $TRDPICON$ was calculted from the likelihood ratio $\mathcal{L}$:

$$\mathcal{L} = \log(\frac{\mathcal{P}(\vec{\epsilon} \mid])}{\mathcal{P}(\vec{\epsilon} \mid \pi)} \tag{6.1}$$

where

- $\vec{\epsilon} = (\epsilon_1, \epsilon_2, ..., \epsilon_N)$ is the set of energies ϵ_i deposited in N TRD planes,
- $P(\vec{\epsilon} \mid e)$ is the probability for an electron to produce $\vec{\epsilon}$
- $P(\vec{\epsilon} \mid \pi)$ is the probability for a pion to produce $\vec{\epsilon}$.

$P(\vec{\epsilon} \mid \pi)$ and $P(\vec{\epsilon} \mid e)$ are determined from a TRD simulation package called TRDSM [37] which was tuned using test beam data. $TRDPICON$ is defined to be the pion rejection factor for the value of the likelihood ratio computed, i.e., the integral of the likelihood ratio distribution derived for pions above the value of the likelihood ratio found for the given track. The pion-electron separation using this variable can be seen in Figure 6.11.

6.3.2 Electron Signatures in the Preshower

For each track an association with hits in the preshower based on proximity was made. In each projection a match between clusters formed in the preshower was made with incoming tracks and the energy deposited in each tube was summed. An identity decision was made based on the amount of energy deposited by a track relative to that of a minimum ionizing particle (see Figure 6.12).

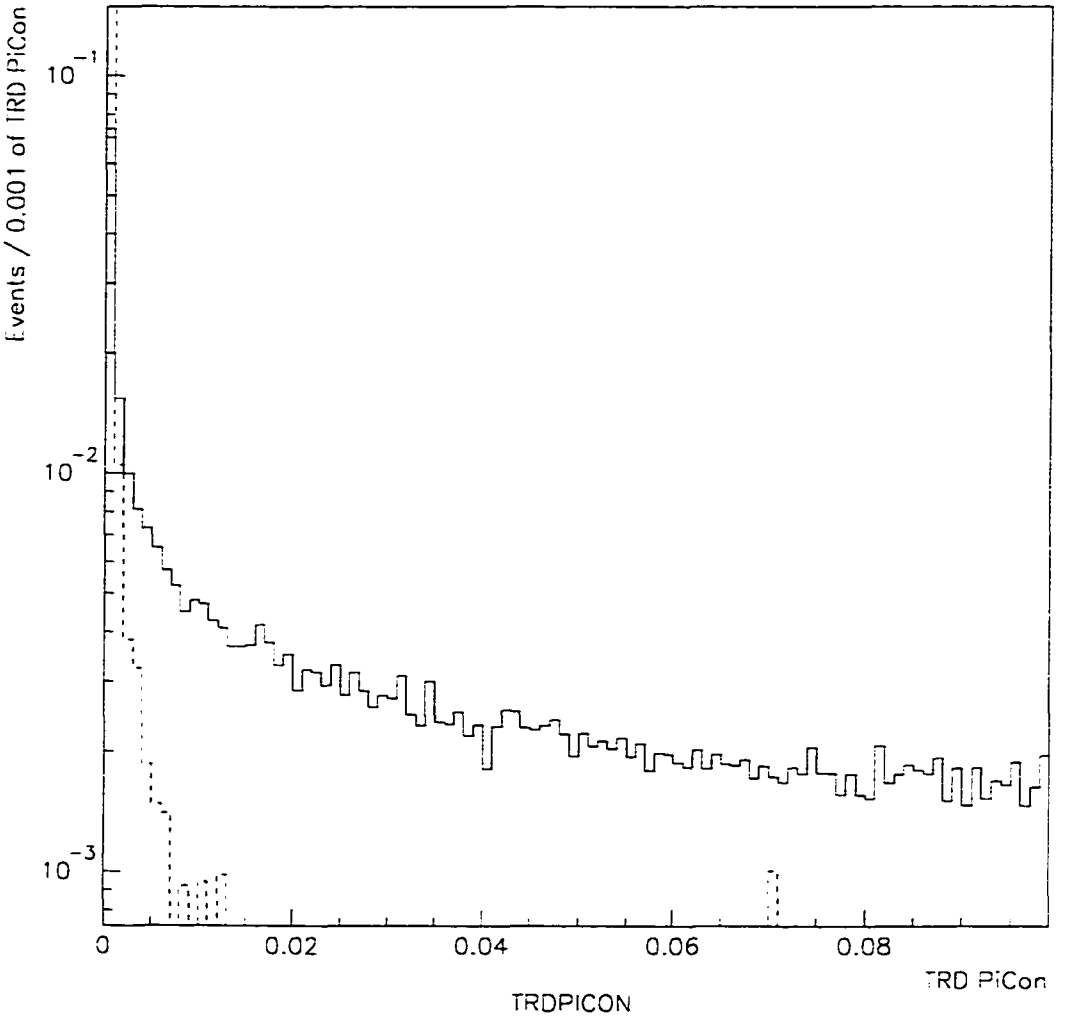

Figure 6.11: The Monte Carlo TRD pion contamination variable as described in the text. The solid line is for π's and the dashed line is for electrons.

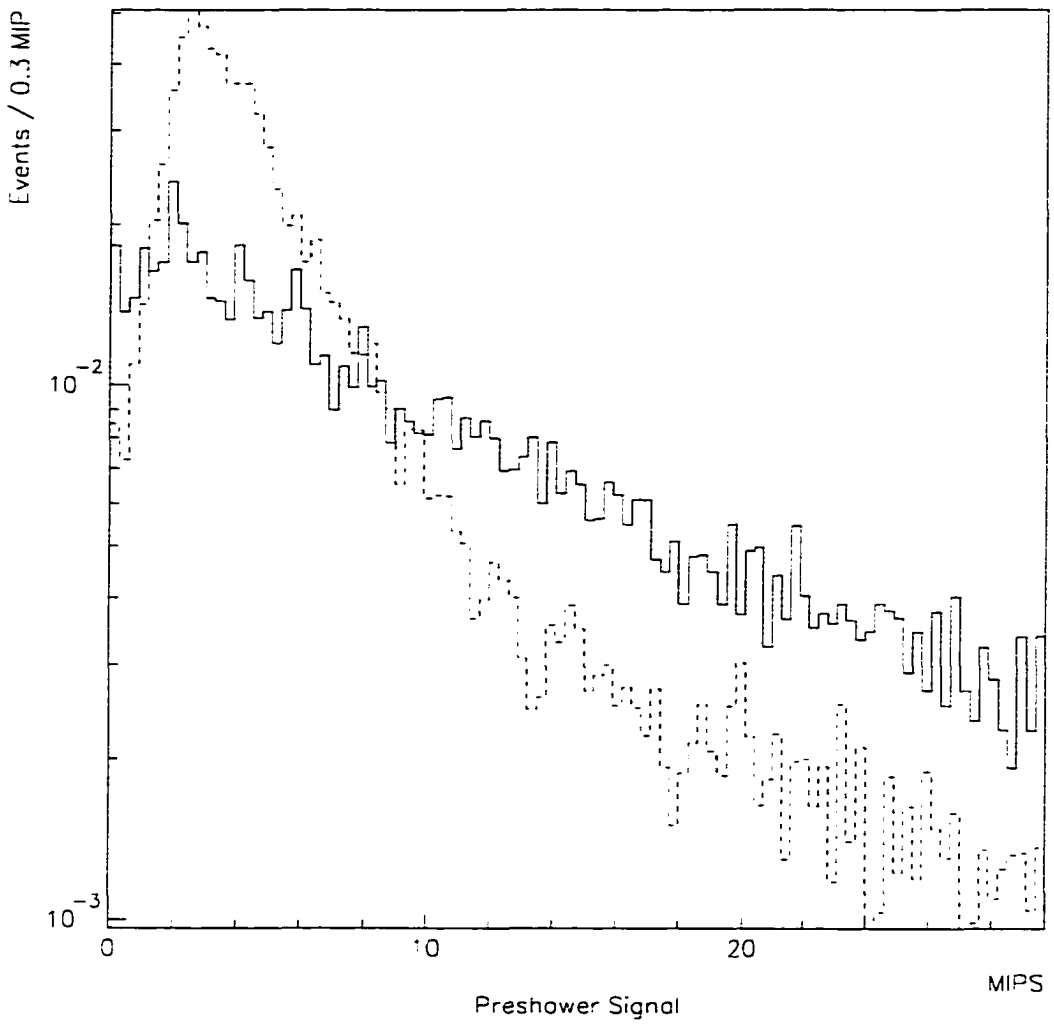

Figure 6.12: Monte Carlo signal deposited in the preshower. The solid line is for π's and the dashed line is for electrons. The pions tend to leave a minimum ionizing signal.

6.3.3 Electron Signatures in the Electromagnetic Calorimeter

For each track reaching the ECal a cluster was made. The two main criteria for electron identification can be made by looking at the difference for a given track's momentum measured by the drift chambers and its associated energy deposited in the ECal and the shower shape of the associated ECal cluster. In this analysis only the difference in $E_{cal} - p_{DC}$ was used. More specifically $E_{cal} - p_{DC}/\Delta(E_{cal} - p_{DC})$ was looked at to make this decision. $\Delta(E_{cal} - p_{DC})$ is the error in the measurement of $E_{cal} - p_{DC}$. Electrons will deposit close to all their energy in the ECal, whereas pions and muons will leave either a minimum ionizing signal or only a fraction of their energy (See Figure 6.13).

6.3.4 Electron Selection

Since the leading lepton was already selected, and major sources of background reduced, using kinematical information, slightly less stringent electron identification requirements can be imposed on lepton candidates that one might have to use in order to insure the desired level of purity. Electrons were identified by either of the following criteria:

- $TRDPICON < 1 \times 10^{-2}$
- $E_{cal} - p_{DC}/\Delta(E_{cal} - p_{DC}) > -0.5$

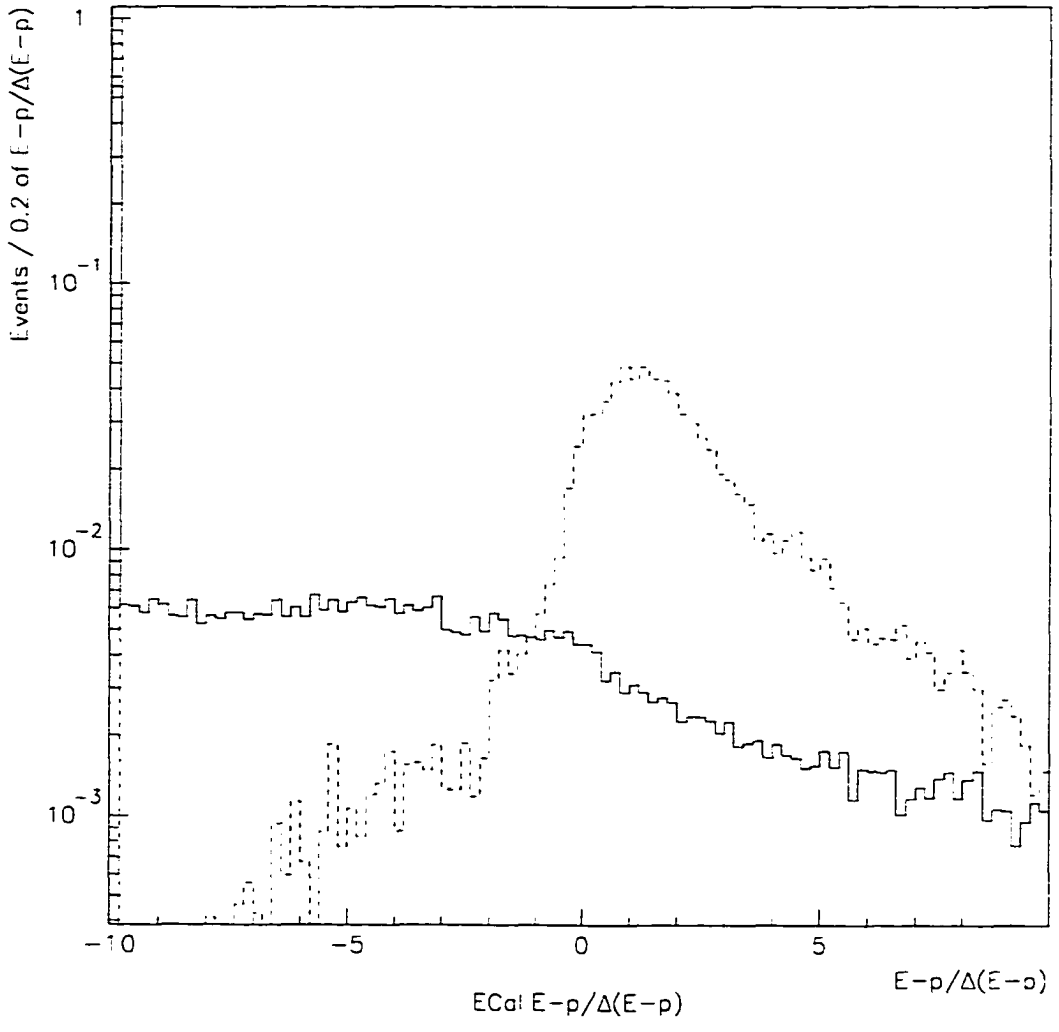

Figure 6.13: Monte Carlo Simulated $E_{cal} - p_{DC}/\Delta(E_{cal} - p_{DC})$. The solid line is for π's and the dashed line is for electrons. The pions tend to leave a minimum ionizing signal. The electrons tend to clump around zero. Underflows are shown in the first bin.

- $PRS_x + PRS_y > 3MIPS$

OR

- No Match in TRD

- $E_{cal} - p_{DC}/\Delta(E_{cal} - p_{DC}) > -0.3$

- $PRS_x + PRS_y > 6MIPS$

This selects out 86% of electrons and 4.8% of pions. The energy dependence is shown in Figure 6.14.

Furthermore, it was required that there be no muon in the event for it to be classified as a ν_e.

6.3.5 Muon Identification in the Muon Chambers

Extrapolations of every track were made to the muon chambers. A decision for a proper match was made by proximity of extrapolation and tracks formed in the two stations of muon chambers. A distance of 40 cm or less was required for a match in station one and a distance of 50 cm or less was required for a match in station two. The selection efficiency as a function of energy is shown in Figure 6.15.

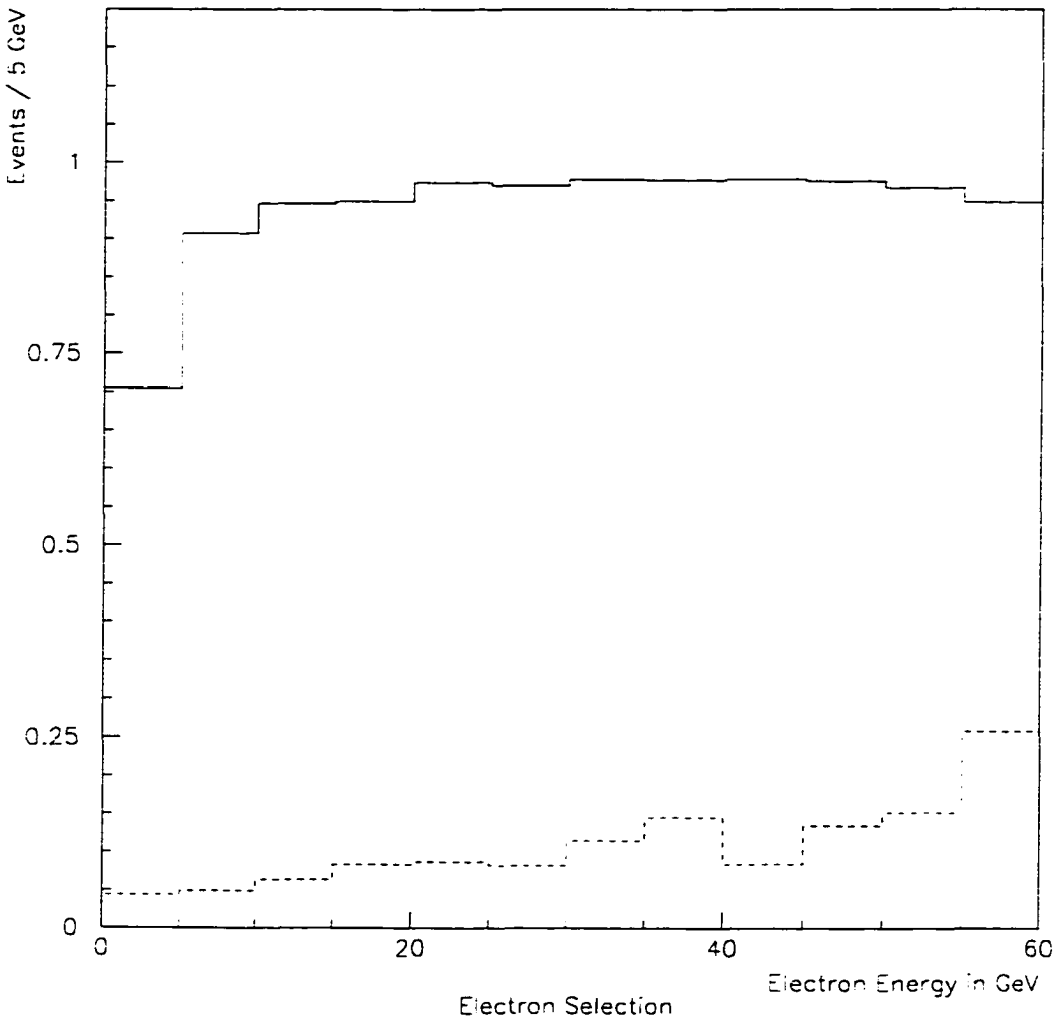

Figure 6.14: Monte Carlo Selection Efficiency for Electrons and Pions as a Function of Energy. The solid line is for electrons and the dashed line is for π's.

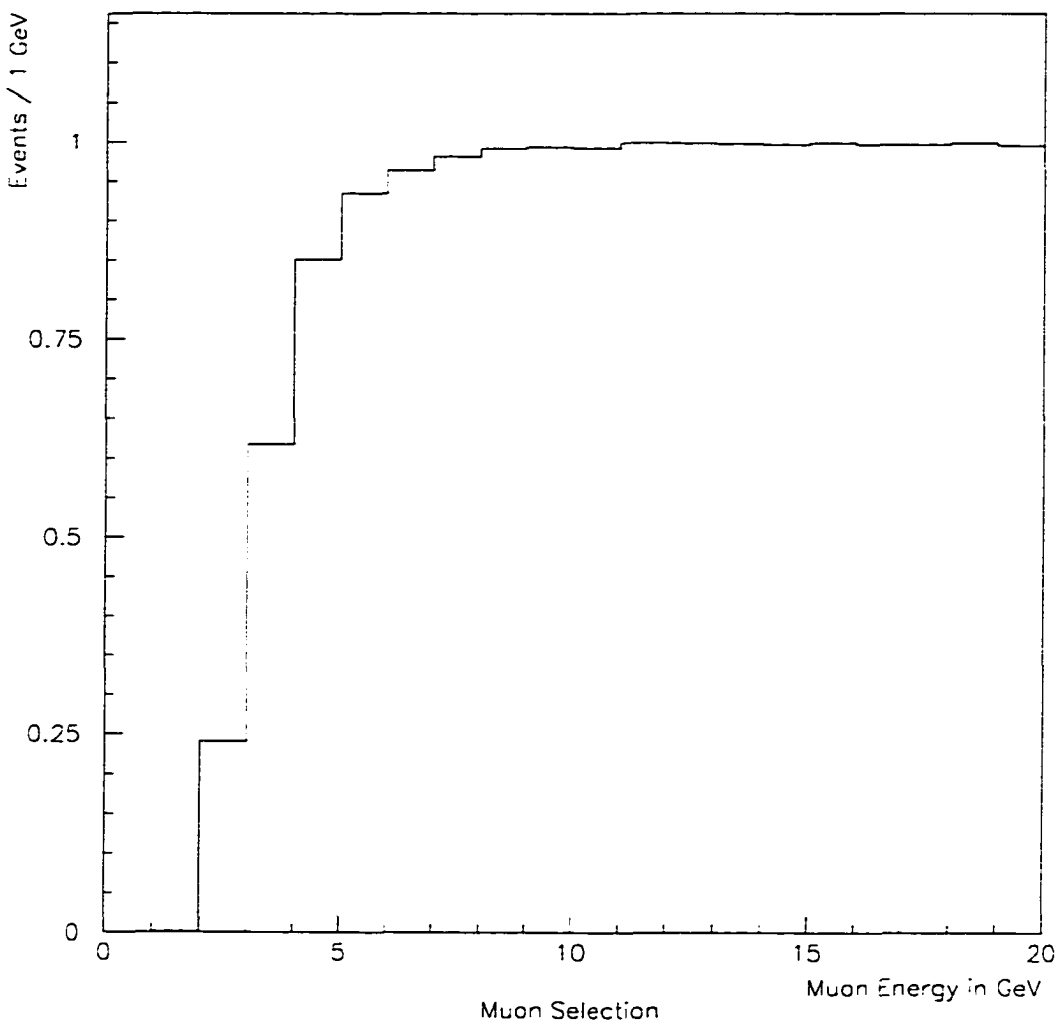

Figure 6.15: Monte Carlo Selection Efficiency for Muons as a Function of Energy. Low energy muons below about 3 GeV do not have enough energy to make it to the muon stations.

6.4 Comparsion of Predicted Spectrum with Data

The main thrust of this analysis revolves around looking for differences between the ratio of ν_μ and ν_e energy spectra predicted from the Monte Carlo and that of the selected data sample. Therefore, a good agreement between the data and the Monte Carlo is ideal.

The problem immediately run across is that the agreement of the ν_μ spectrum predicted by the Monte Carlo and that of the data differ significantly as seen in Figure 6.16 and Figure 6.17. In other analyses the ν_μ spectrum from the data is used to reweight the ν_e spectrum to make a better prediction. Unfortunately, that is the method proposed to look for a ν_e oscillation signal.

When Figures 6.18 and 6.19 are looked at, other kinematic variables show that similar problems are observed (as should be expected) in the leptonic and hadronic energy spectrum. In the transverse variables a very dramatic difference in the p_t spectrum is seen.

A very detailed comparison of ν_μ CC events in the data and Monte Carlo in NOMAD was done by Geiser and Long [35]. Their study used a FLUKA based beam Monte Carlo and not the empirical parametrization used for this analysis. The major points are outlined here.

NEGLIB Event Weights : At the level of NEGLIB event generation, there are several kinematic cutoffs, specifically $\nu > 1.0$ GeV, $Q^2 > 0.3$ GeV^2 and $W^2 > 1.3$ GeV^2. To compensate for this they reweight events near these

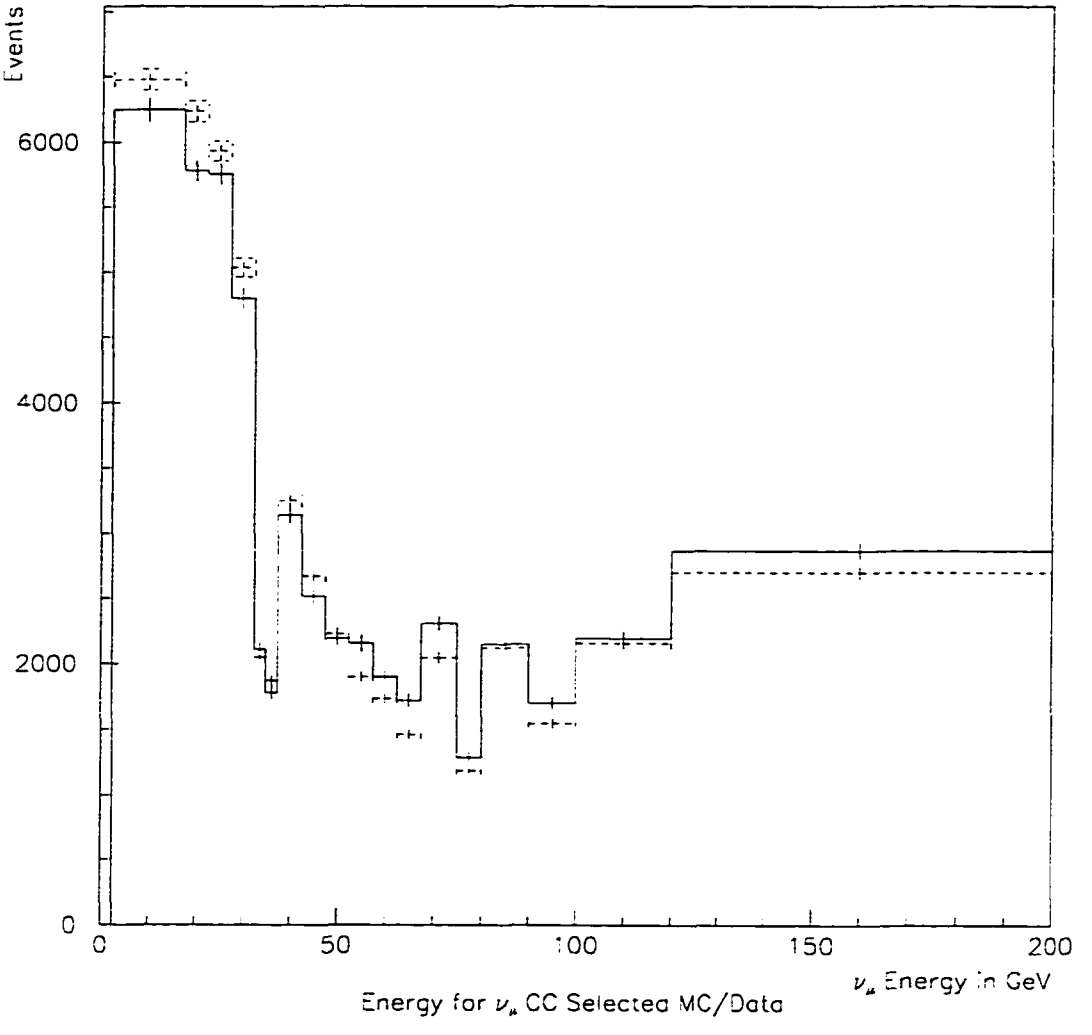

Figure 6.16: The Spectrum of ν_μ from Selected Data and from Selected Monte Carlo. The solid line is Monte Carlo and the points are data.

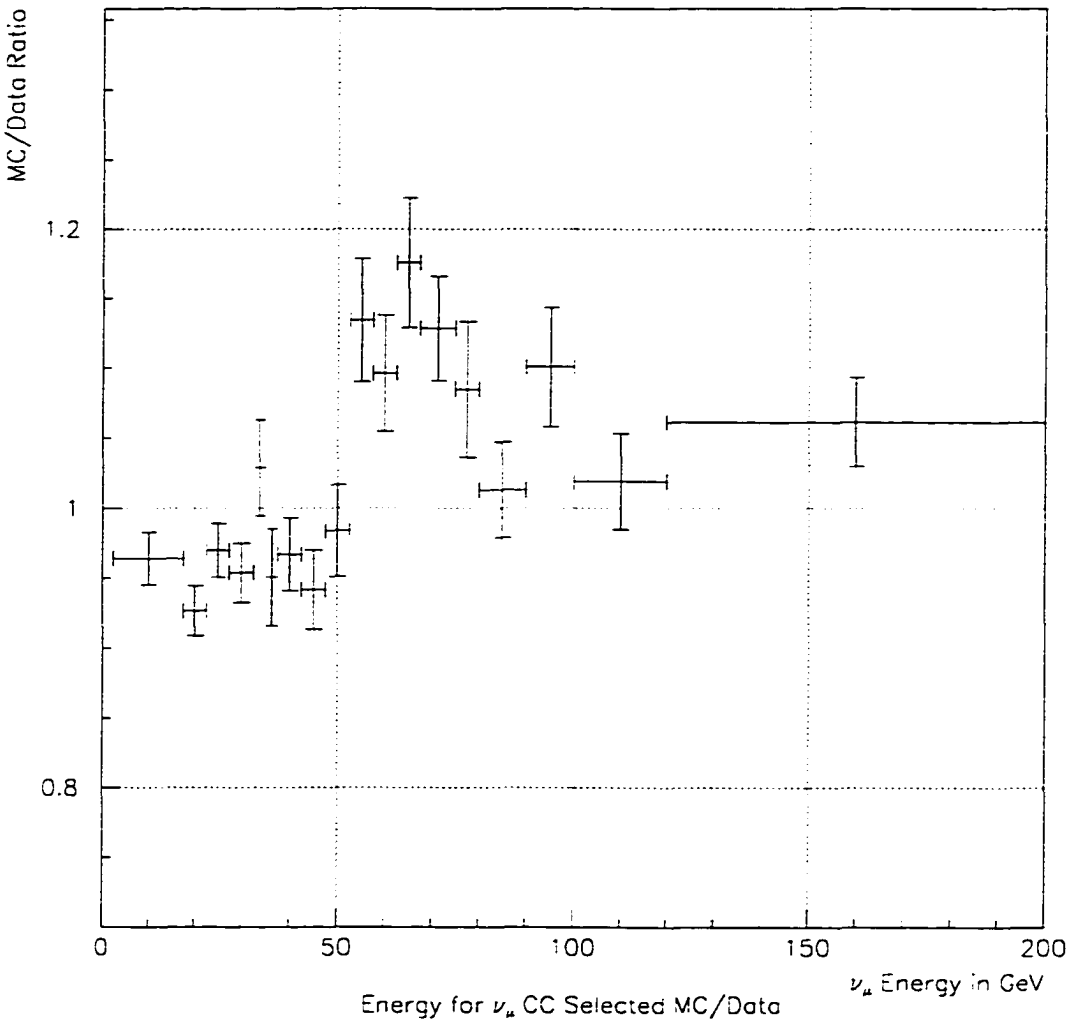

Figure 6.17: The Ratio of the Spectrum of ν_μ from the Data and from the Monte Carlo.

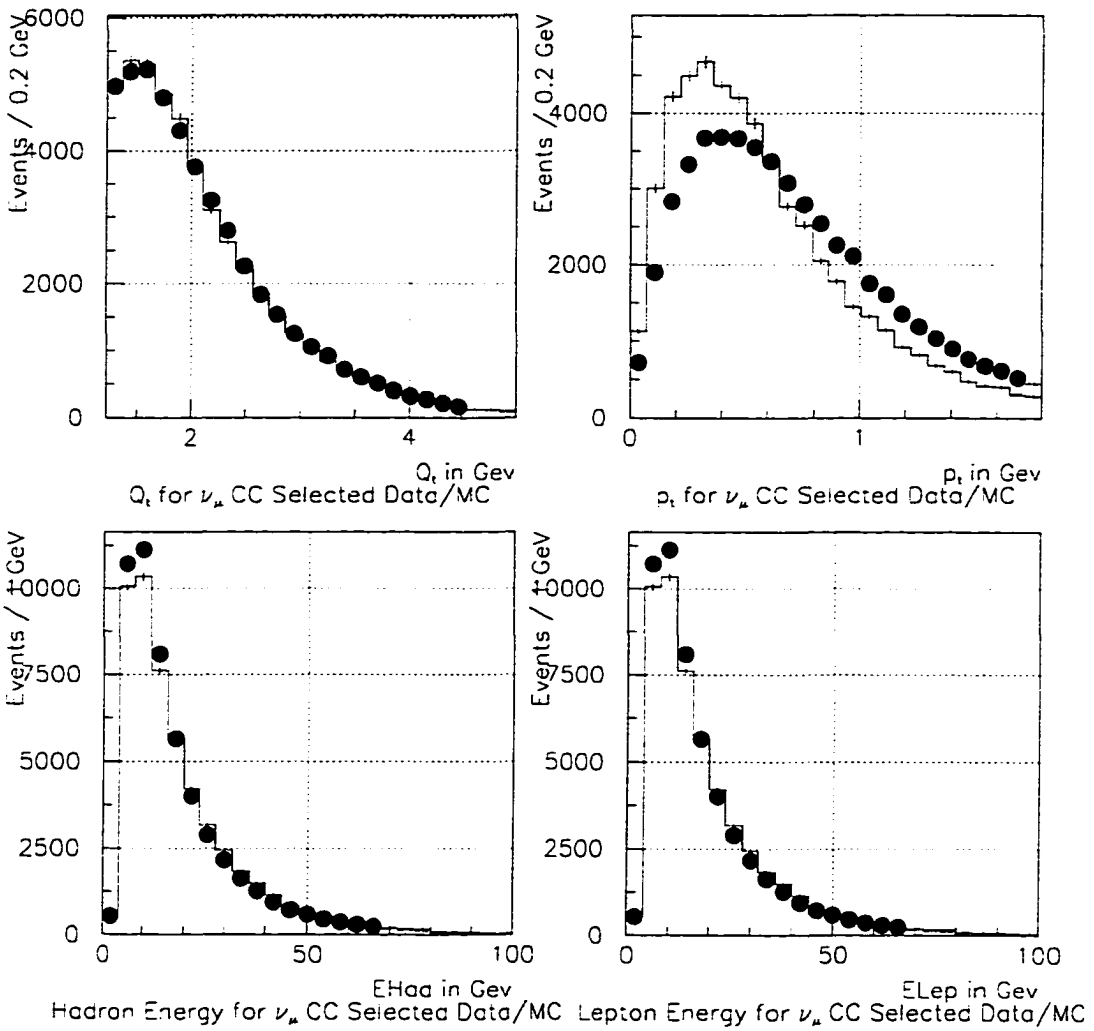

Figure 6.18: Kinematic Variables of ν_μ CC Selected Events from Data and from Monte Carlo. The solid line is Monte Carlo and the points are data.

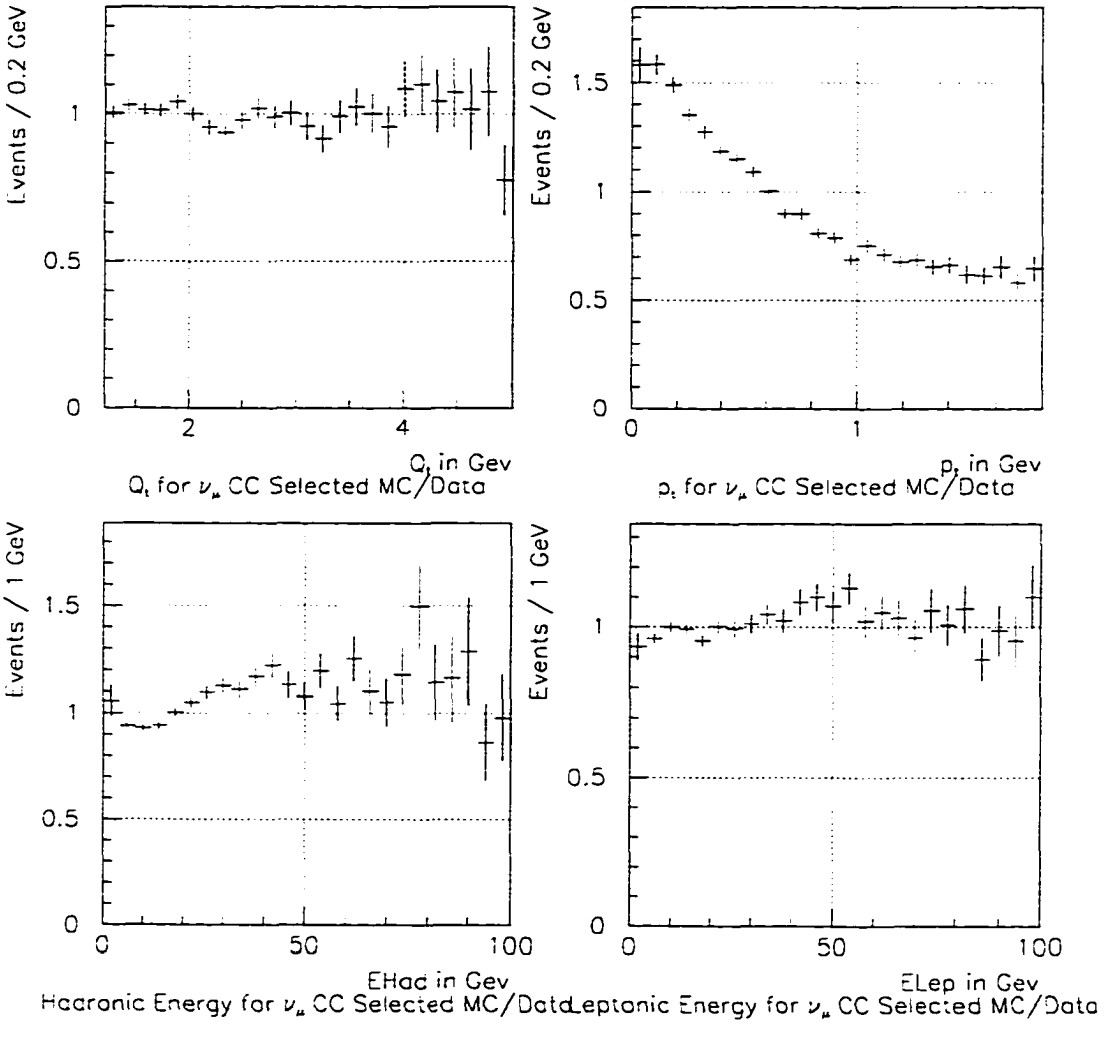

Figure 6.19: Ratios of Kinematic Variables of ν_μ CC selected Events Data to Monte Carlo.

limits by factors that can range from 1-3. In this analysis the requirement that events have a minimum Q^2 and W^2 helps to avoid this region.

Filter Efficiency : Due to constraints of the reconstruction program, events with no tracks in them and events with high hit densities were not dealt with at all. The global efficiency for this filter is approximately 93% but can be much lower for events with high energy. A study by P. Steffen [38] showed that a correction of the form

$$Corr = 1.013 + (1.178 \times 10^{-5})E_\nu^2 \tag{6.2}$$

is needed, where E_ν is the true neutrino energy. This will be necessary when the limit is calculated because the efficiencies calculated were done on a sample that has already been filtered. This correction has a minimal effect on the final answer though, since it effects both ν_e and ν_μ the same way.

Nuclear Effects : There are several nuclear effects which were not taken into account at the generation level.

- The tail of the Fermi momentum distribution was generated above the original cutoff of 225 MeV/c. A flat distribution up to 1 GeV/c was introduced in approximately 10% of the events to deal with this.
- Nuclear reinteractions are not well understood, but were not dealt with at all in the version of the simulation used. Routines from the

NUCRIN package [39] were used to simulate these effects. This program calculates the probability of reinteraction for low energy ($p < 5$ GeV/c) hadrons and updates the track list. Interactions occur on the order of 10% of events.

- A soft nuclear recoil was introduced in events as a random boost opposite the direction of the original jet. This was tuned to reproduce the p_t distribution of the hadron jet.

Nuclear effects mainly effect the transverse variables. In fact they can explain the difference between the data and Monte Carlo in the p_t spectrum well. The effect on this analysis of p_t is primarily in the determination of the selection efficiency and will be discussed further on.

The results, pertinent to this analysis, of the Geiser-Long analysis can be seen in Figure 6.20. The discrepancies between the data and the Monte Carlo persist. Primarily, there was a large discrepancy between the hadronic energy measured in the data and that derived from the Monte Carlo. For this analysis this was not a large problem because the ratio of the $\nu_e/\ \nu_\mu$ spectra was what was considered. In fact, all errors in common between ν_e and ν_μ will be small or negligible as they will cancel each other in the ratio. For example, this analysis was done with and without the correction factor due to the filter efficiency problem and the result remained the same. These corrections were therefore not taken into account in this analysis.

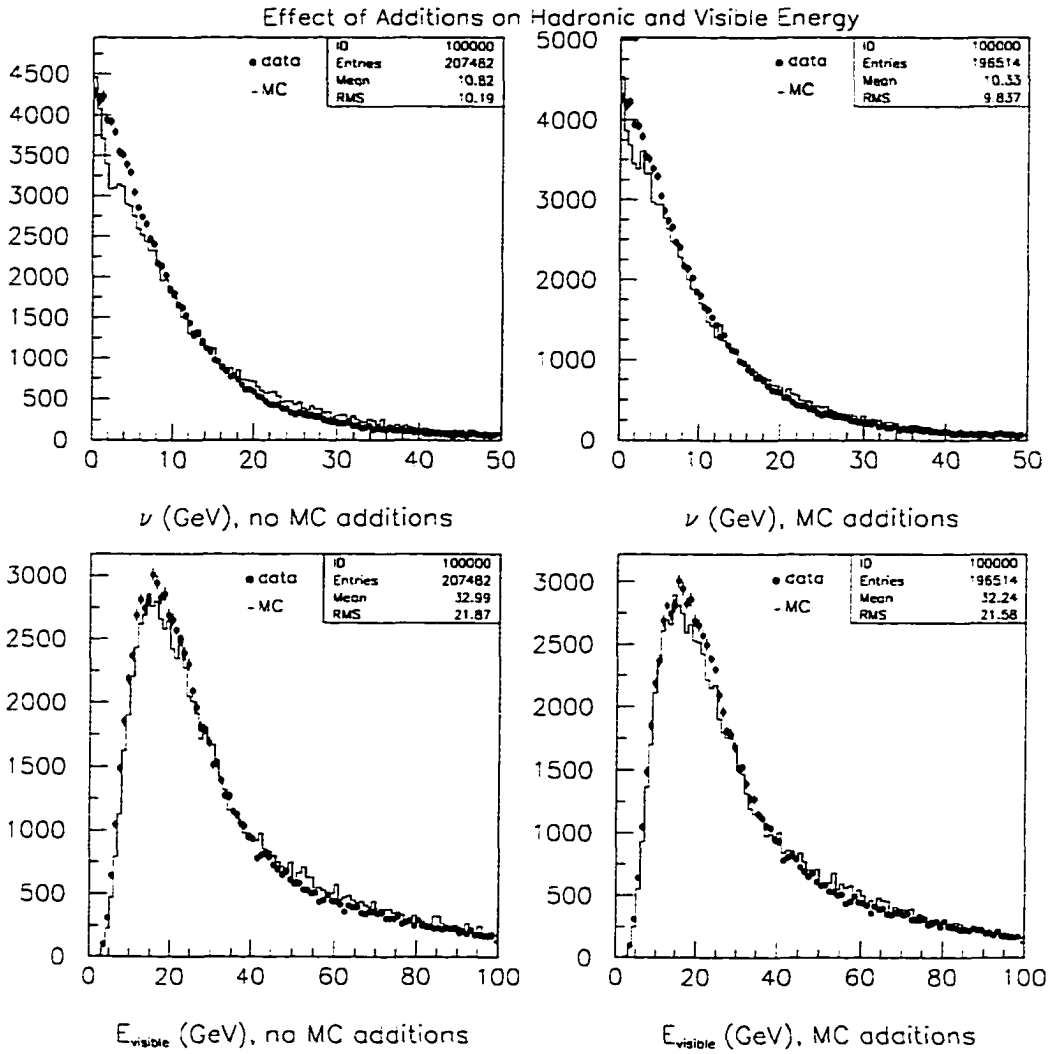

Figure 6.20: Hadronic and Visible Energy Distributions of ν_μ CC events before (left) and after (right) Geiser/Long Monte Carlo corrections.

There may still be a problem in the understanding of the neutrino flux. In fact, the shape of Figure 6.17 indicates an excess of higher energy events in the Monte Carlo, suggesting that a decrease of the kaon contribution to the flux distribution would be in order, but unfortunately this is not sufficient. Some of these errors should have factored out as the ratio of $\nu_e/\ \nu_\mu$ spectra was used, but they do not completely cancel as the two have different sources. It will be seen that the misunderstanding of the flux will lead to a large part of this analysis' systematic error.

6.5 Total Events Selected and Monte Carlo Efficiencies

The efficiencies for selection of different types of events were determined from the Monte Carlo. In Table 6.4 a breakdown of the overall selection efficiencies for ν_μ and ν_e events, as well as the efficiencies of individual cuts, is given in Table 6.5. The selection efficiency with respect to energy is shown in Figure 6.21.

The major factor in reducing the neutral current background comes from the Q_t and the p_t cuts. Unfortunately, this cuts out a large portion of the CC sample close to 40%. The requirement of no muon in the event and the electron particle ID were quite effective in reducing the sizable ν_μ background in the ν_e sample.

To determine the number of expected events in each MC category the number

Cut	ν_e CC Efficiency	ν_μ CC Efficiency	ν_μ NC Efficiency
$Q_t > 1.0$ GeV	.673	.628	.034
$p_t < 2.5$ GeV	.965	.977	.682
$\Delta z < 15$ cm	.923	.971	.848
$Q^2 > 2$ GeV^2	.861	.848	.655
$W^2 > 5$ GeV^2	.967	.932	.828
Muon in event	.969	.047	.932
Lead Particle electron ID	.799	.007	.038
Total	.382	.00015	.00030

Table 6.4: MC Event Selection Cuts and Efficiencies on ν_e MC Samples.

of ν_μ in the MC sample was normalized to match the level in the data sample. In Table 6.6 the final number of selected events and the number expected from Monte Carlo for both ν_e and ν_μ are given.

In the end, 721 ν_e events and 52598 ν_μ events were observed. The shape of the ν_e spectrum is shown in Figure 6.22. A break down of the event population can be found in Table 6.7. The Monte Carlo prediction of 722.3 events for the number of ν_e compares well with the number found in the data. There was a 4.3% background (see Figure 6.23) in the ν_e's and negligible background in the ν_μ's. Note the low statistics in the ν_e background; it was small but not negligible.

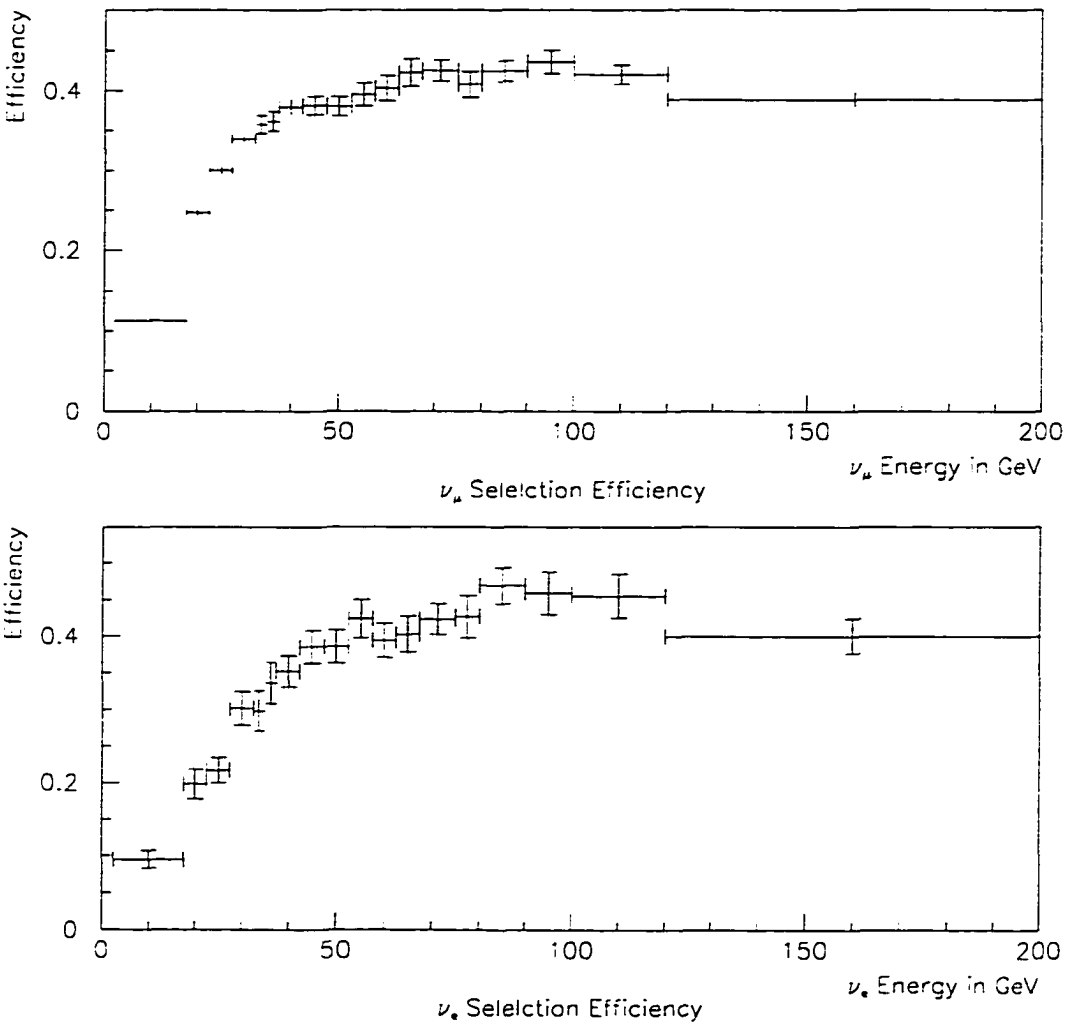

Figure 6.21: Selection Efficiencies for ν_μ and ν_e versus Energy.

Cut	ν_μ CC Efficiency	ν_e CC Efficiency	ν_μ NC Efficiency
$Q_t > 1.0$ GeV	.628	.673	.033
$p_t < 2.5$ GeV	.977	.966	.681
$\Delta z < 15$ cm	.971	.923	.848
$Q^2 > 2$ GeV^2	.861	.848	.655
$W^2 > 5$ GeV^2	.967	.932	.828
Lead Particle muon ID	.899	.001	.020
Total	.419	.0006	.00021

Table 6.5: MC Event Selection Cuts and Efficiencies on ν_μ MC Samples.

	Selected ν_e	Selected ν_μ
ν_e CC Monte Carlo	691.1	1.1
ν_μ CC Monte Carlo	18.4	52589.9
ν_μ NC Monte Carlo	12.8	7.1
Total MC	722.3	52598.1
4 DC Module Data	130.0	7643.0
8 DC Module Data	254.0	18383.0
11 DC Module Data	337.0	26572.0
Total Data	721.0	52598.0

Table 6.6: Final ν_e and ν_μ Events Selected and Predictions from Monte Carlo.

Energy Bin	Selected ν_e	Selected ν_μ
2.5- 17.5 GeV	17.0 ± 4.1	6479.0 ± 80.5
17.5- 22.5 GeV	38.0 ± 6.1	6235.0 ± 78.9
22.5- 27.5 GeV	52.0 ± 7.2	5932.0 ± 77.0
27.5- 32.5 GeV	56.0 ± 7.5	5038.0 ± 70.9
32.5- 35.0 GeV	35.0 ± 5.9	2050.0 ± 45.3
35.0- 37.5 GeV	28.0 ± 5.2	1872.0 ± 43.3
37.5- 42.5 GeV	67.0 ± 8.1	3249.0 ± 57.0
42.5- 47.5 GeV	50.0 ± 7.1	2673.0 ± 51.7
47.5- 52.5 GeV	53.0 ± 7.3	2231.0 ± 47.2
52.5- 57.5 GeV	53.0 ± 7.3	1900.0 ± 43.6
57.5- 62.5 GeV	34.0 ± 5.8	1733.0 ± 41.6
62.5- 67.5 GeV	37.0 ± 6.1	1462.0 ± 38.2
67.5- 75.0 GeV	48.0 ± 6.9	2044.0 ± 45.2
75.0- 80.0 GeV	24.0 ± 4.9	1185.0 ± 34.4
80.0- 90.0 GeV	37.0 ± 6.1	2121.0 ± 46.1
90.0-100.0 GeV	31.0 ± 5.6	1541.0 ± 39.3
100.0-120.0 GeV	29.0 ± 5.4	2154.0 ± 46.4
120.0-200.0 GeV	32.0 ± 5.7	2699.0 ± 52.0

Table 6.7: Final ν_e and ν_μ Events Selected with Errors in Each Energy Bin.

6.6 ν_μ-ν_e Spectrum Ratio

An oscillation signal would evince itself in the form of an enhancement in the low energy part of the spectrum (for low Δm^2) or over the entire spectrum (for large Δm^2). Looking directly at the ν_e spectrum is problematic because this makes the measurement extremely sensitive to fluctuations in the predicted flux and simulation. Looking at the ratio ν_e/ν_μ helps to cancel out some of this dependence but does not completely resolve the problem as ν_e's and ν_μ's have different sources. The ratio approach also cancels out other common effects such as hadronic energy resolution and event selection biases. This analysis, therefore, looks at the ratio of the two spectra.

A non-uniform binning was used for the energy spectrum. This was done in order to maintain a sufficient level of statistical significance in each channel. The energy bins were chosen so that each channel has no fewer than than 15 ν_e events (see Table 6.7).

As can be seen from a cursory scan of Figure 6.24, the agreement between the selected sample and the prediction was quite good. Over the eighteen bins there were 10 bins with an excess of the data over the Monte Carlo and 8 bins with a deficit. The χ^2 [40] used for this data sample is

$$\chi^2 = \sum_i -2 \log P(n_i|\mu_i) + 2 \log P(n_i|n_i) \tag{6.3}$$

where

$$P(n|\mu) = (\mu + b)^n \frac{\exp^{-\mu+b}}{n!} \tag{6.4}$$

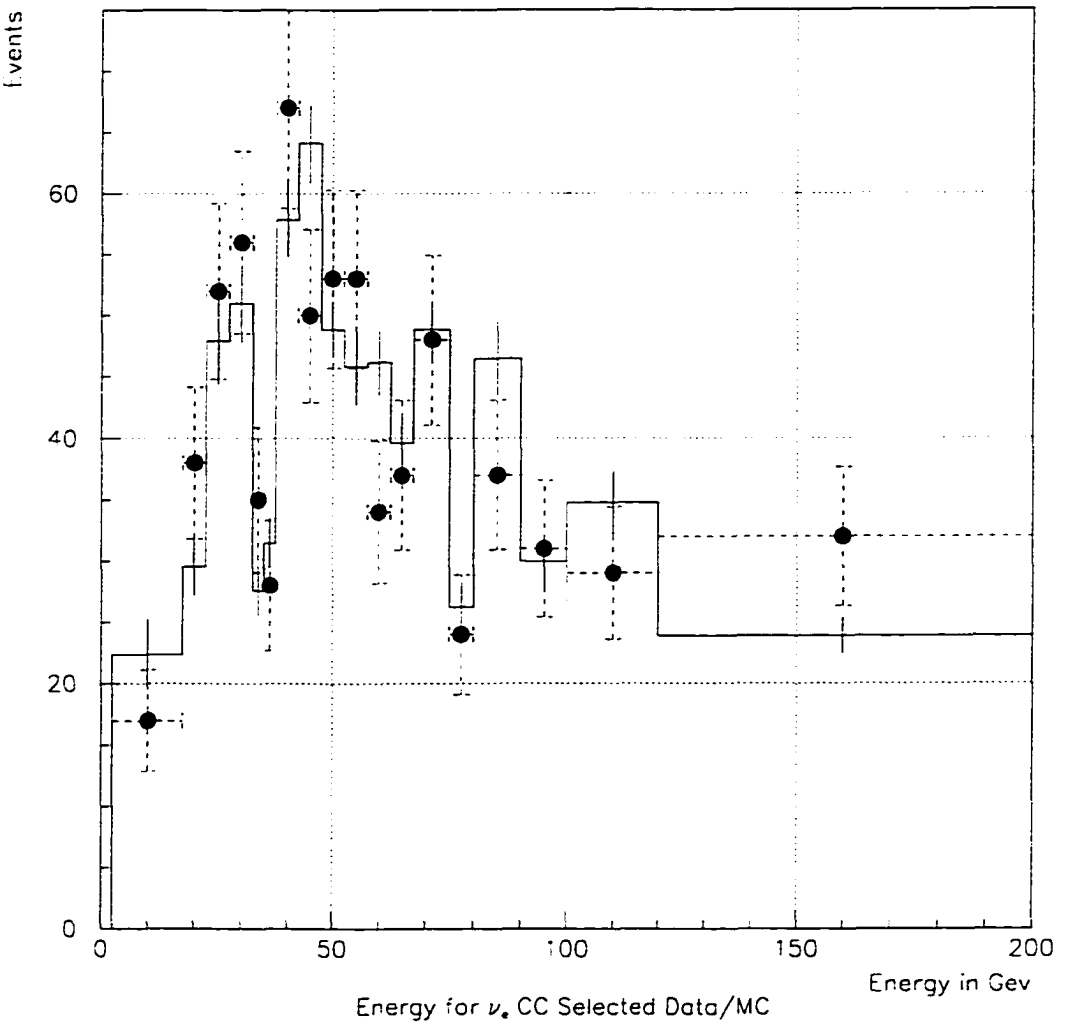

Figure 6.22: ν_e CC Selected Spectrum. The Monte Carlo is the solid line and the data are the dots.

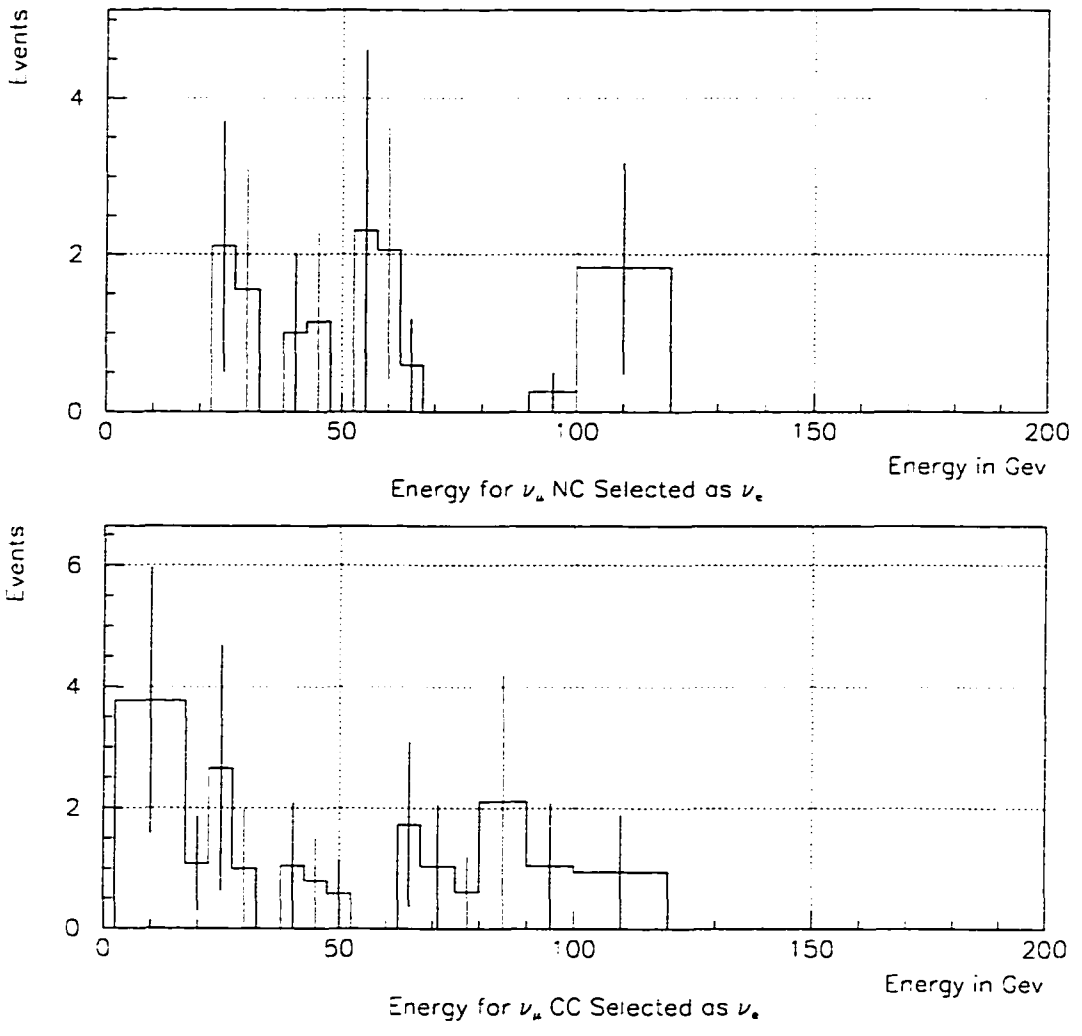

Figure 6.23: Background Shapes from ν_μ NC and CCs. The top graph is from NC and the bottom from CC.

Here μ is the number of signal events expected, b is the number of background events and n is the number of events observed.

These were summed for all energy bins and found to be 20.9 for 18 degrees of freedom. Locally, there were no regions of significant excess. It was therefore assumed that there was no excess of ν_e events over the Monte Carlo and therefore no evidence for neutrino oscillations.

The rest of the discussion will now concentrate on extracting a limit on the oscillation probability.

6.7 Setting a 90% Confidence Limit

The standard way of presenting neutrino oscillation limits is by giving a region in the plane of Δm^2 vs $\sin^2 2\theta$ for which oscillations have been ruled out at a 90% confidence level. In order to define this region, several values for Δm^2 were taken and the corresponding Monte Carlo prediction for the ratio spectrum was calculated for the $\sin^2 2\theta$ which minimizes the χ^2. Then the values of $\sin^2 2\theta$ for which the χ^2 is 2.71 over the minimum were found. For each Δm^2 there is now a value of $\sin^2 2\theta$ and these points define the 90% confidence level boundary.

6.7.1 ν_e Oscillation Contribution

The oscillation probability is a function of the energy of the incoming neutrino as well as the distance it has travelled. In order to calculate the probability

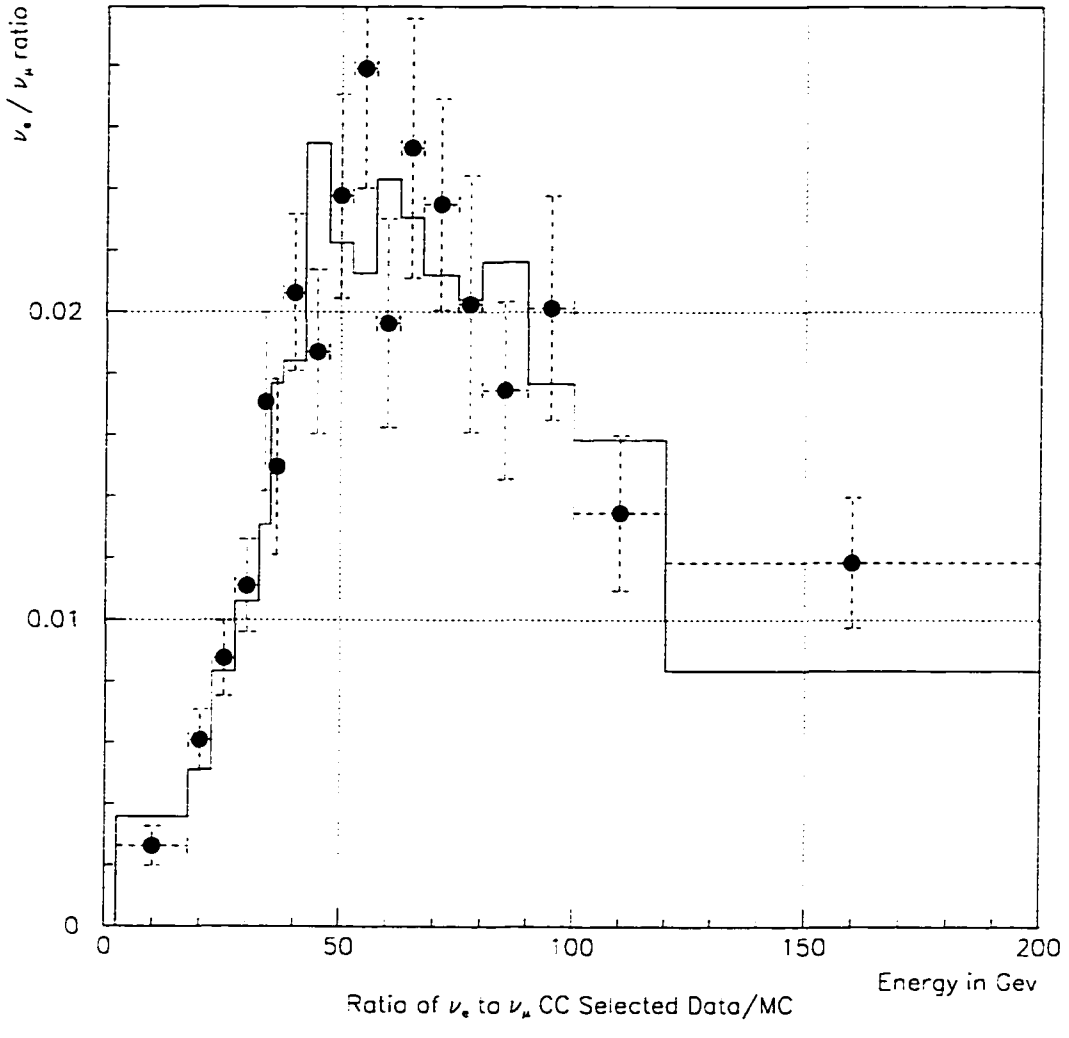

Figure 6.24: The ratio of ν_e and ν_μ CC Spectra. The solid line is Monte Carlo and the dots are the data.

$p(\nu_\mu \rightarrow \nu_e)$ that a given neutrino will oscillate, the following equation was used:

$$p(\nu_\mu \rightarrow \nu_e) = \sin^2 2\theta \sin(\frac{1.27\Delta m^2 L}{E}) \tag{6.5}$$

where E is the energy of the incoming neutrino in GeV, and L is the path length travelled in kilometers. The neutrino source is not a point source, it is in fact a 413 meter long tunnel. The oscillation probability was calculated at 200 points along the length of the tunnel and averaged. The distribution of decays along the tunnel was assumed to be flat. The difference this length effect has on the final oscillation contribution can be seen by comparing the distributions in Figure 6.25 and Figure 6.26. It can be seen that absence of corrections due to the length of the tunnel induces spikes to the spectrum which are smoothed out due to the different points of origins of neutrinos along the tunnel.

Once the oscillation probability was calculated it can be applied to the ν_μ spectrum to determine the shape of the oscillation contribution to the ν_e spectrum. This distribution is shown for four different values of Δm^2 in Figure 6.26. Then from the previous Monte Carlo study the selection efficiency and corrections from the reconstruction can be factored in to give the spectrum as it would be observed in the data. The effect is shown for four different values of Δm^2 in Figure 6.27. Finally, the oscillation contribution was added to the background ν_e spectrum from standard ν_e sources. Looking at Figure 6.28 where a contribution with a $\sin^2 2\theta$ of 0.01 has been added to the ν_e spectrum, the different effects from different Δm^2 can be seen. For low Δm^2 the excess will be seen mostly in the

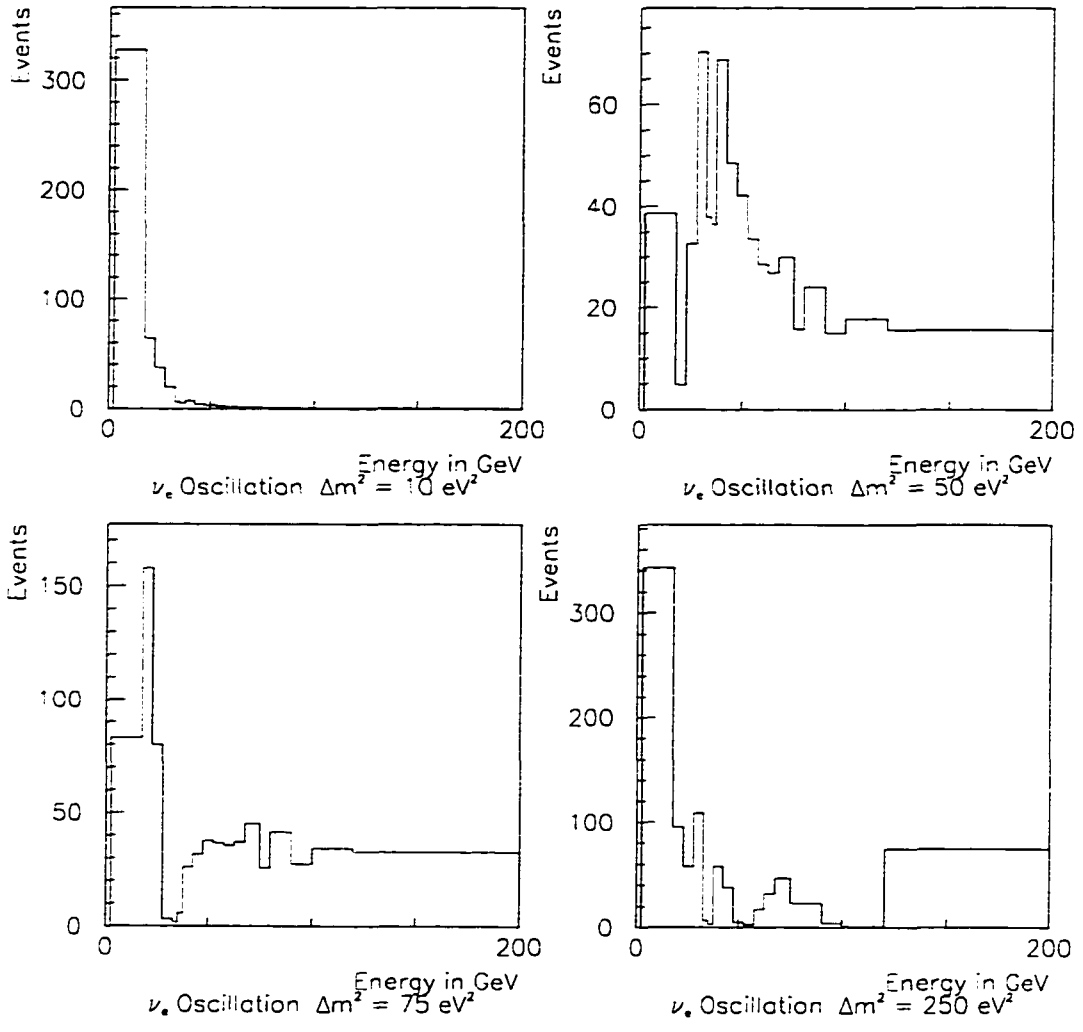

Figure 6.25: The ν_e Oscillation Contribution for Δm^2 of 10 eV$^2/c^4$, 50 eV$^2/c^4$, 100 eV$^2/c^4$, 250 eV$^2/c^4$ without the length of the tunnel taken into account.

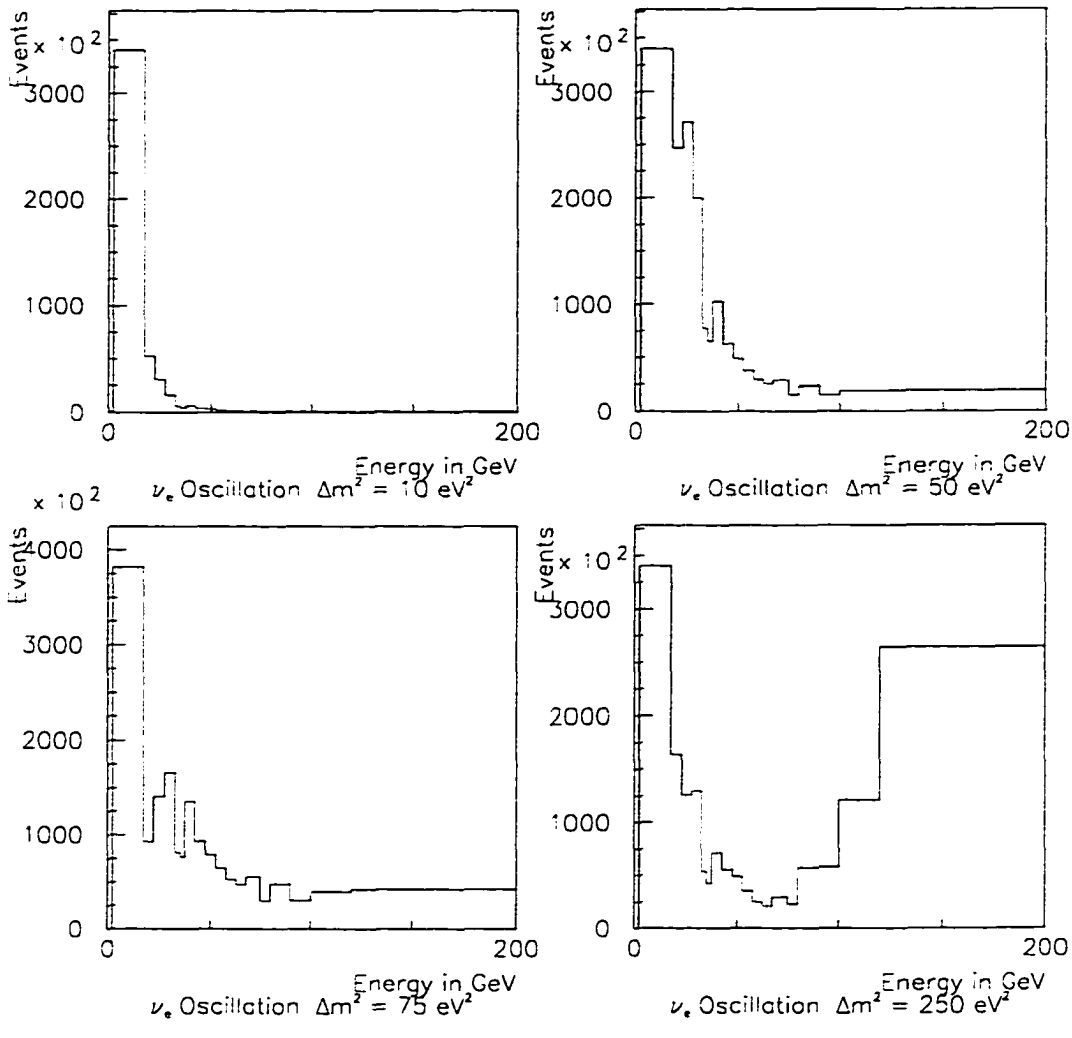

Figure 6.26: The ν_e Oscillation Contribution for Δm^2 of 10 eV$^2/c^4$, 50 eV$^2/c^4$, 100 eV$^2/c^4$, 250 eV$^2/c^4$.

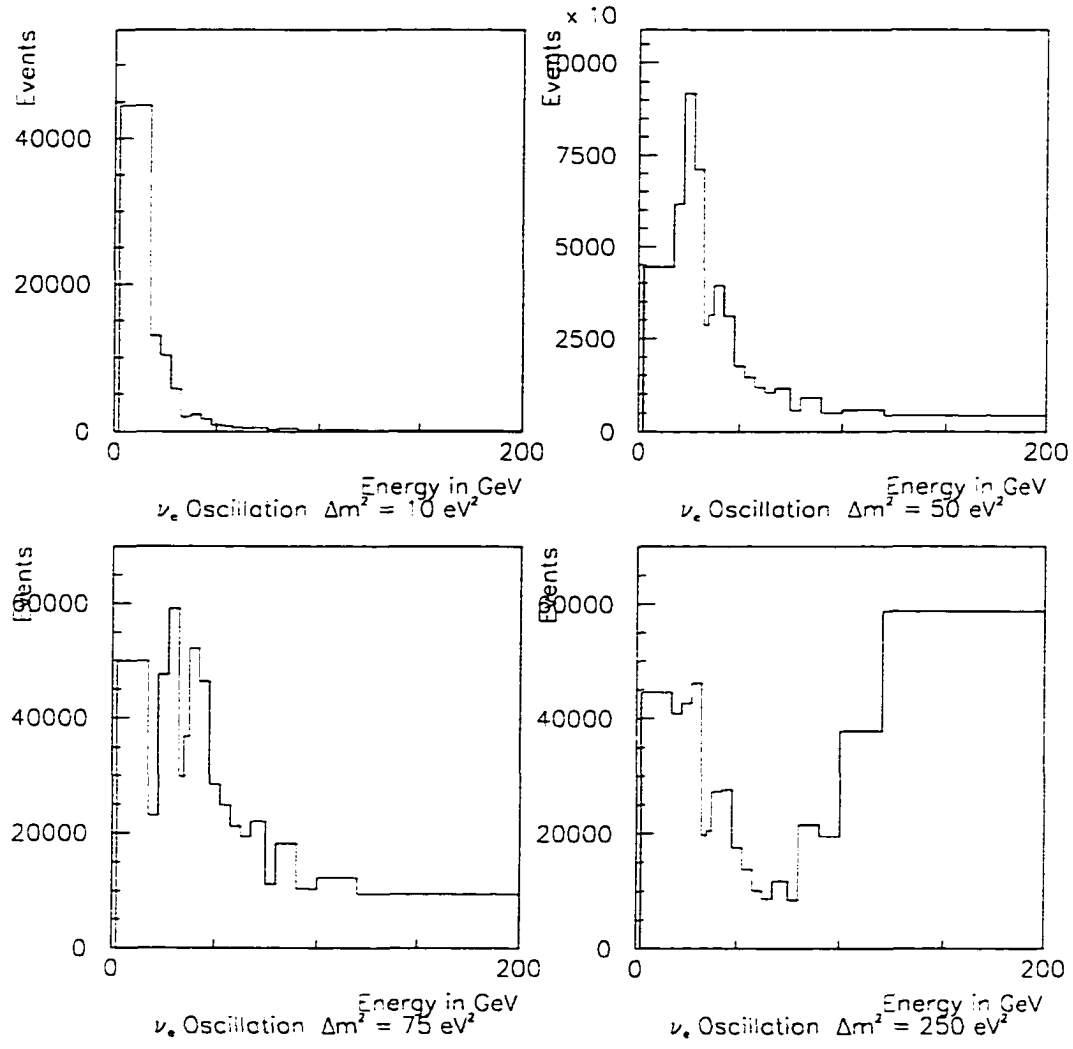

Figure 6.27: The ν_e Oscillation Contribution for Δm^2 of 10 eV$^2/c^4$, 50 eV$^2/c^4$, 100 eV$^2/c^4$, 250 eV$^2/c^4$ corrected for ν_e efficiency.

low energy region whereas, for higher Δm^2 the excess is noticeable on the whole spectrum.

6.7.2 Minimization of the χ^2

With the form of the signal available for a set of Δm^2s, it is possible to calculate the value of $\sin^2 2\theta$ that minimizes χ^2 for each value of Δm^2. For gaussian errors the standard form that χ^2 takes is:

$$\chi^2 = \sum_i \frac{\left(\frac{N_i^{E^{\nu_e}}(MC)+N_i^{E^{\nu_e}}(Osc)}{N_i^{E^{\nu_\mu}}(MC)} - \frac{N_i^{E^{\nu_e}}(Data)}{N_i^{E^{\nu_\mu}}(Data)}\right)^2}{\sigma_i^2} \tag{6.6}$$

where σ_i^2 is just taken from the $\sqrt{n_i}$ where n_i is the number entries in the ith bin. This form unfortunately has the problem that for bins where the data is less than predicted the error is too small and bins where there is more data than predicted the error is too big. An alternate form for the χ^2 based on the likelihood function was used:

$$\chi^2 = 2\sum_i N_i^{E^{\nu_e}}(Predicted) - N_i^{E^{\nu_e}}(Data) + N_i^{E^{\nu_e}}(Data)\log\frac{N_i^{E^{\nu_e}}(Data)}{N_i^{E^{\nu_e}}(Predicted)} \tag{6.7}$$

where

$$N_i^{E^{\nu_e}}(Predicted) = N_i^{E^{\nu_\mu}}(Data)\frac{N_i^{E^{\nu_e}}(MC)}{N_i^{E^{\nu_\mu}}(MC)} + N_i^{E^{\nu_e}}(Osc) \tag{6.8}$$

This is derived from equations 6.3 and 6.4.

In order to find χ^2_{min} the Newton-Raphson method for finding roots was used. This method uses the the derivative of a function to extrapolate to zero and then

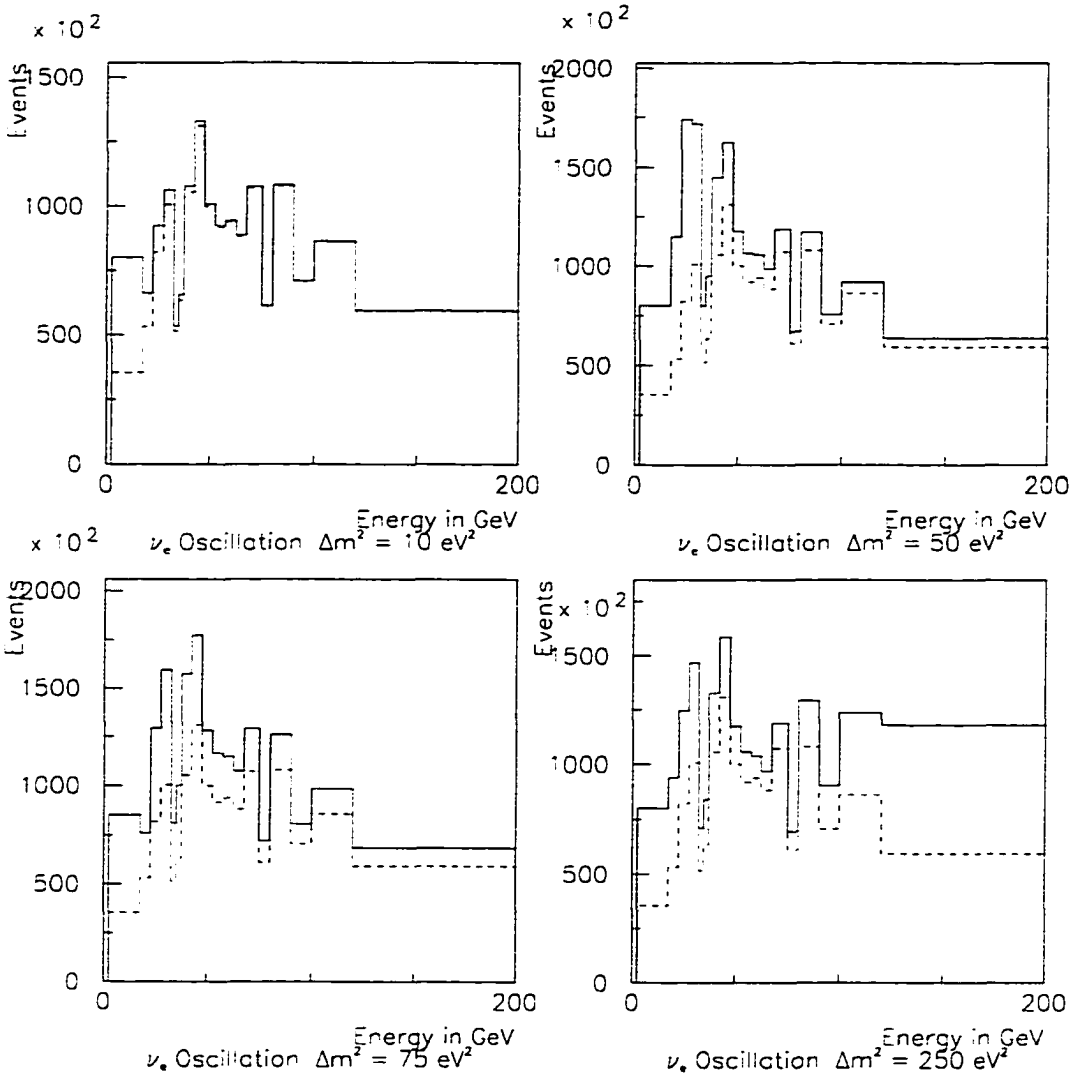

Figure 6.28: The ν_e Oscillation Contribution for Δm^2 of 10 eV^2/c^4, 50 eV^2/c^4, 100 eV^2/c^4, 250 eV^2/c^4 with $\sin^2 2\theta = 0.01$ corrected for efficiency and added to the ν_e spectrum. The dotted line is the ν_e spectrum with no oscillation contribution.

using that point as the next guess. The functional form the $N_i^{E^{\nu_e}}(Predicted)$ can be rewritten in terms of $\sin^2 2\theta$:

$$N_i^{E^{\nu_e}}(Predicted) = N_i^{E^{\nu_\mu}}(Data)\frac{N_i^{E^{\nu_e}}(MC)}{N_i^{E^{\nu_\mu}}(MC)} + \sin^2 2\theta N_i^{E^{\nu_e}}(Osc) \qquad (6.9)$$

where $N_i^{E^{\nu_e}}(Osc)$ is now the oscillation contribution for a $\sin^2 2\theta$ value of 1.

Then, taking the derivative of this function with respect to $\sin^2 2\theta$ is trivial. Minimum values of χ^2 were then sought between values of -1.0 and 10. Once a value for the minimum of χ^2 was found, then the Newton-Raphson method was used once more to find the value of $\sin^2 2\theta$ for which χ^2 is the minimum χ^2 + 2.71 which gives us the two-sided 90% confidence limit for a χ^2 distribution with one degree of freedom. This was done for for values of Δm^2 from 0.1 eV^2/c^4 up to 250 eV^2/c^4. For each of these values of Δm^2, a value of $\sin^2 2\theta$ was found. These points define the boundary of a 90% confidence level area of exclusion of neutrino oscillation in the Δm^2-$\sin^2 2\theta$ plane. It is displayed in Figure 6.29. The limit, at 250 eV^2/c^4, is 2.4×10^{-3}. Notice also the ripple in the curve with a frequency of about 20 eV^2/c^4. This is the effect of the $\sin(\frac{1.27\Delta m^2 L}{E})$ term in the oscillation probability. With an average energy of 30 GeV and the propagation distance about 1 km, a frequency of order 20 eV^2/c^4 is expected.

6.7.3 Alternative Methods

While this method is valid given that it is assumed that there was no signal in this selected data sample, there are other techniques which have historically been

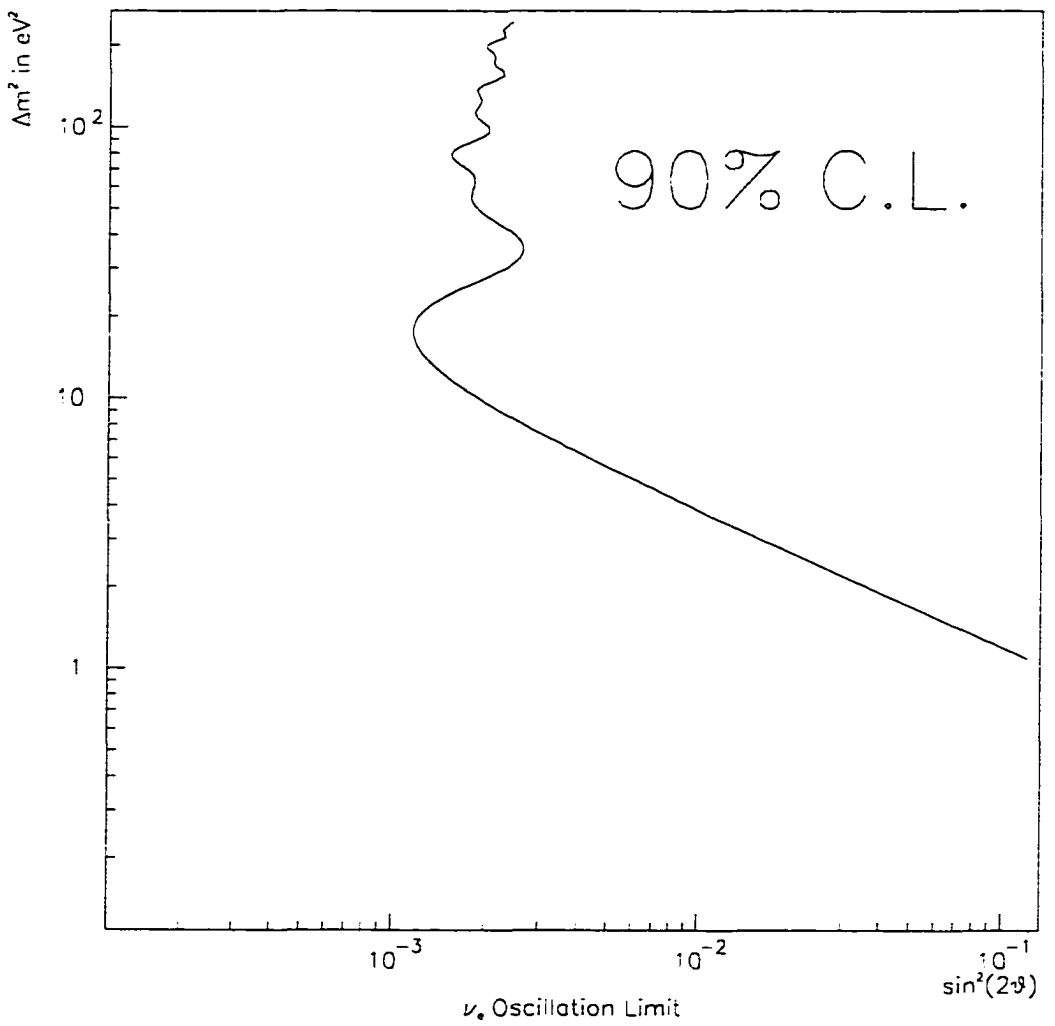

Figure 6.29: Boundary of 90% Confidence Level Exclusion of ν_e Oscillations from Statistical Errors Only.

used to perform this calculation. These methods are discussed in [41] where, also, a new method for performing this calculation is presented. These methods are referred to as the Raster Scan, the Flip-Flop Raster Scan, and the Global Scan. The method used in this analysis is called the Raster Scan.

The Flip-Flop Raster Scan makes a decision whether to set a one-sided upper limit or a two-sided interval based on what is seen in the data. If a signal with greater than three standard deviations significance is seen, then one performs the normal Raster Scan to come up with an interval of acceptance. If not an upper limit is set using the one-sided 90% C.L. $\Delta\chi^2$ value of 1.64. This method suffers from the fact that it undercovers the 90 % C.L. region.

The Global Scan makes a best fit to both Δm^2 and $\sin^2(2\theta)$, and then all points that have a χ^2 within 4.61 of this minimum value are said to be within the region of confidence. This method suffers from both under-coverage and over-coverage.

The method that was used in this analysis is not very effective at finding regions of signal if they exist. This is because it performs the limit calculation at fixed values of Δm^2. Also there is no mechanism for insuring that the limit set is meaningful (i.e., within the physical bounds). The technique proposed in [41] overcomes this flaw by using a method similar to the Global Scan, but it uses a Monte Carlo simulation to determine $\Delta\chi^2$ values for different values of Δm^2 and $\sin^2(2\theta)$ using an ordering technique proposed in the text.

6.8 Systematic Effects

Up to now only statistical errors have been taken into account, even though there are many systematic effects, including the prediction of the neutrino flux, which have not been looked at. This will now be done.

6.8.1 Modifying the Limit

The method used for modifying the limit finds errors for each effect, adds them in quadrature with each other, and then adds this sum in quadrature with the limit.

6.8.2 Kinematic Selection

This analysis is basically a counting and comparison experiment, so variations between the Monte Carlo and reality can have a strong influence on the the final result. A good way to check this is to look for systematic effects due to this selection. In order to study whether systematic effects were introduced by the selection of specific kinematic cuts, the cuts were varied and the subsequent shifts in the end results were observed.

The kinematical cuts were varied as follows.

Cut	Min	Max	Value used
Q_t	0.9 GeV	1.1 GeV	1.0 GeV
p_t	2.2 GeV	2.8 GeV	2.5 GeV
Δz	13.0 cm	17.0 cm	15.0 cm
Q^2	1.5 GeV^2	2.5 GeV^2	2.0 GeV^2
W^2	4.5 GeV^2	5.5 GeV^2	5.0 GeV^2
X and Y Vertex	120.0 cm	140.0 cm	130.0 cm

Each cut was varied individually.

The best fit value of $\sin^2(2\theta)$ was calculated for several values of the given cut in the ranges given above. A search for a systematic pattern was looked for. If none were found the error was taken to be the average shift from the original selected value for value $\sin^2(2\theta)_{BEST}$. The variation in $\sin^2(2\theta)_{BEST}$ for the different cuts can be seen in Figure 6.30 and Figure 6.31.

In Figure 6.31 it is seen that a transition between 130 and 120 cm of the vertex cut is undergone. This is near the edge of the fiducial region of NOMAD. It can be seen that this effect is of the order of about 0.3×10^{-3}, which is small compared to the statistical error. An error of 0.3×10^{-3} was assigned due to the choice of the vertex.

More significant seems to be the choice of W^2 cut. As can been seen in Figure 6.32, there is a transition region between 4 GeV^2 and 6 GeV^2. The level of this effect is of the order 0.7×10^{-3}. An error of 0.7×10^{-3} was assigned due to the choice of the W^2 cut.

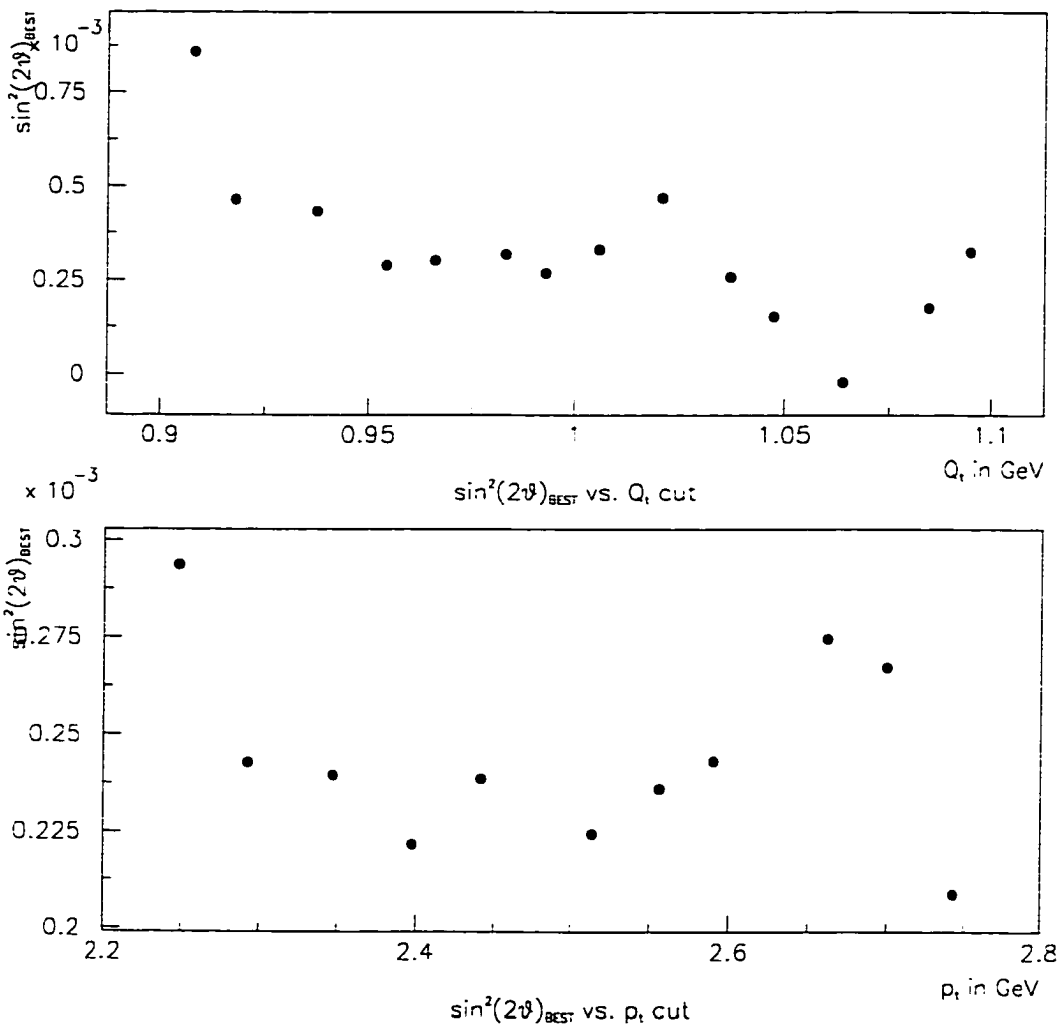

Figure 6.30: Variation in $\sin^2(2\theta)_{BEST}$ vs. Cuts on Q_t and p_t.

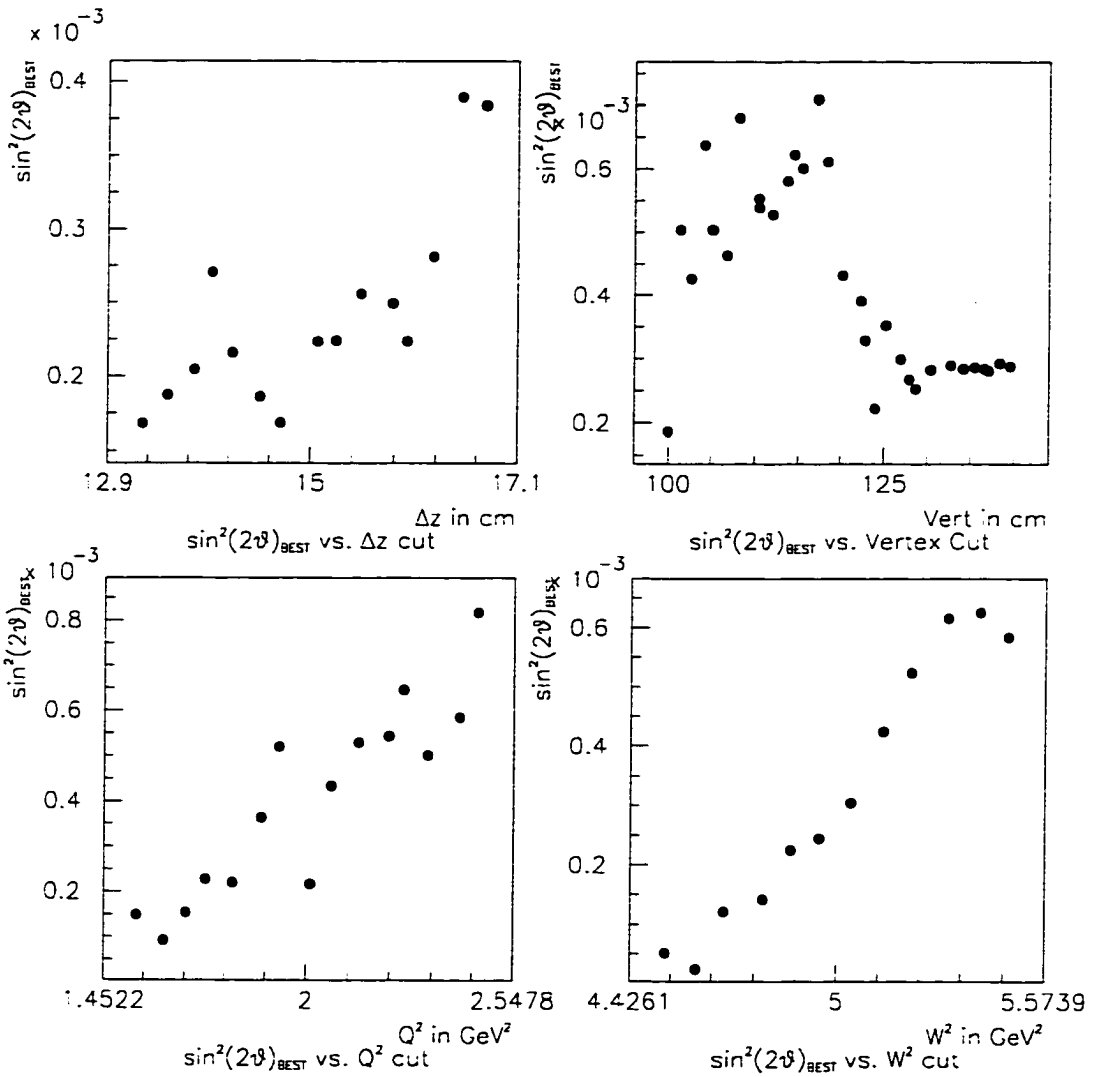

Figure 6.31: Variation in $\sin^2(2\theta)_{BEST}$ vs. Cuts on Δz, the Vertex Position, Q^2 and W^2.

A similar effect exists for the Q^2 cut (see Figure 6.32). The level of the effect is of the order of 0.5×10^{-3}. An error of 0.5×10^{-3} was assigned due to the choice of the Q^2 cut.

Trends in the other variables were not detected. The magnitude of all these effects can be see in Table 6.8.

6.8.3 Electron Selection

In order to see the effect of differences in electron selection between data and Monte Carlo, the electron selection criteria were modified and the subsequent shift in the ν_e/ν_μ ratio was looked at. The variations used were:

Cut	Min	Max	Value used
$TRDPICON$	8×10^{-3}	1.5×10^{-2}	1×10^{-2}
$E_{cal} - p_{DC}/\Delta(E_{cal} - p_{DC})$	0.0	-1.0	-0.5
$PRS_x + PRS_y$	2.0	9.0	3.0

Each criteria was varied individually.

The best fit value of $\sin^2(2\theta)$ was calculated for several values of the given cut in the ranges given above. A search for a systematic pattern was looked for. If none were found the error was taken to be the average shift from the original selected value for value $\sin^2(2\theta)_{BEST}$. The variation in $\sin^2(2\theta)_{BEST}$ can be seen in Figure 6.33.

As expected these effects are not large (see Table 6.8), as the main selection of the proper leading lepton comes from the kinematical choice of the leading

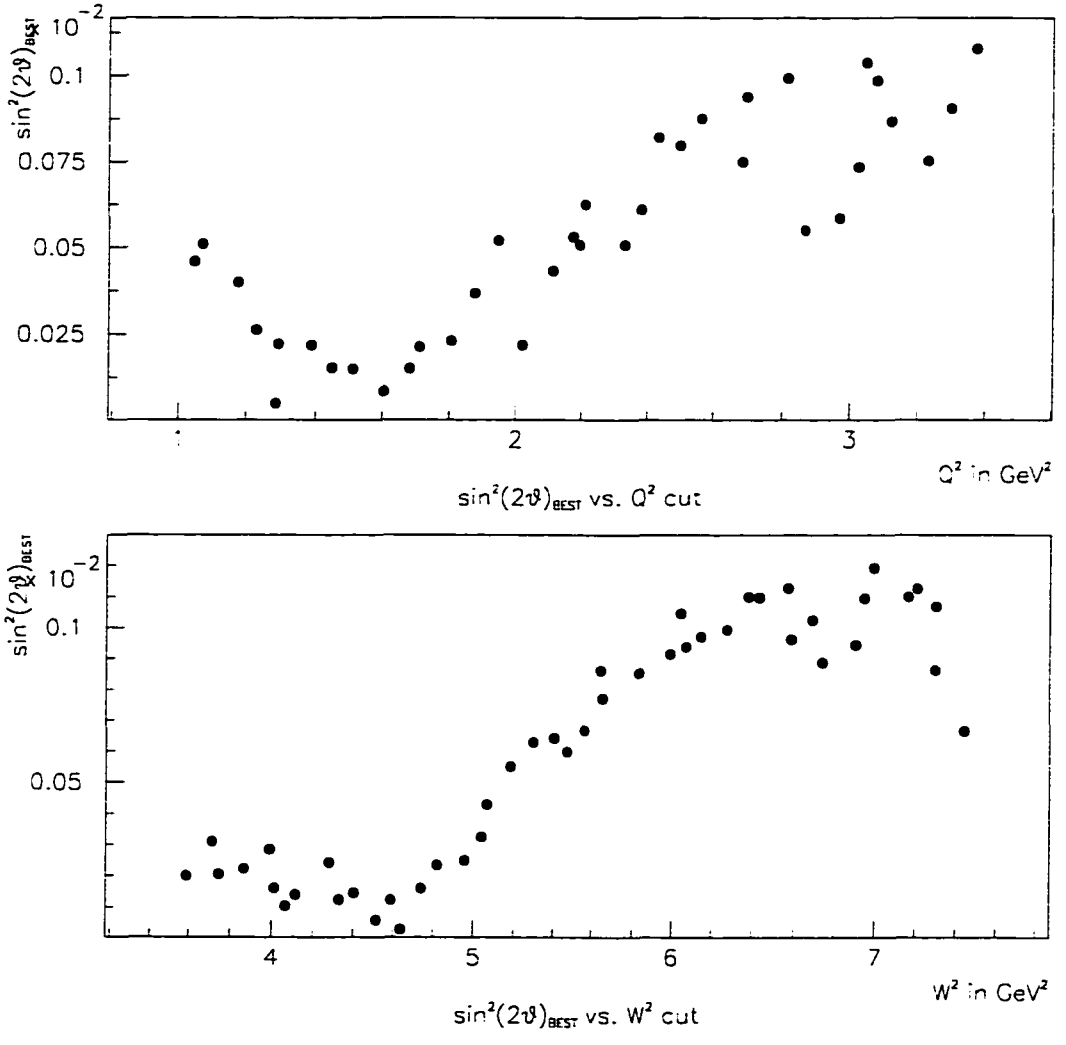

Figure 6.32: Variation in $\sin^2(2\theta)_{BEST}$ vs. Cuts on Q^2 and W^2.

lepton. Most of the error originates from the Ecal cut on $E - p/\Delta(E - p)$.

6.8.4 ν_e Flux

The error of the ν_e flux from the empirical parametrization used is 2.7% [30]. In order to see the effect on this analysis, the predicted ν_e spectrum was shifted by plus/minus this amount and the difference in the end result was observed. It can be seen that this variation is small, in Figure 6.34. In Figure 6.35 the variation can be seen to be small relative to the statistical error. The error introduced is of the order 0.9×10^{-3}. This is the single largest error.

6.8.5 Electron Track Reconstruction

The difference between muon tracks being reconstructed in the MC and data was measured to be less than 1% [35] by using tracks in the TRD. Electrons are much more difficult to measure as they scatter in the tracking media and this has not been measured very well. For this analysis we assumed an error of 3% as reasonable given the order of the effect for muons.

6.8.6 Other Effects

A study using a similar method was done by Weber [42] on the same data sample and several other systematic effects were looked at and found to be small. Among these effects were the shape of the background, the shape of the flux, event

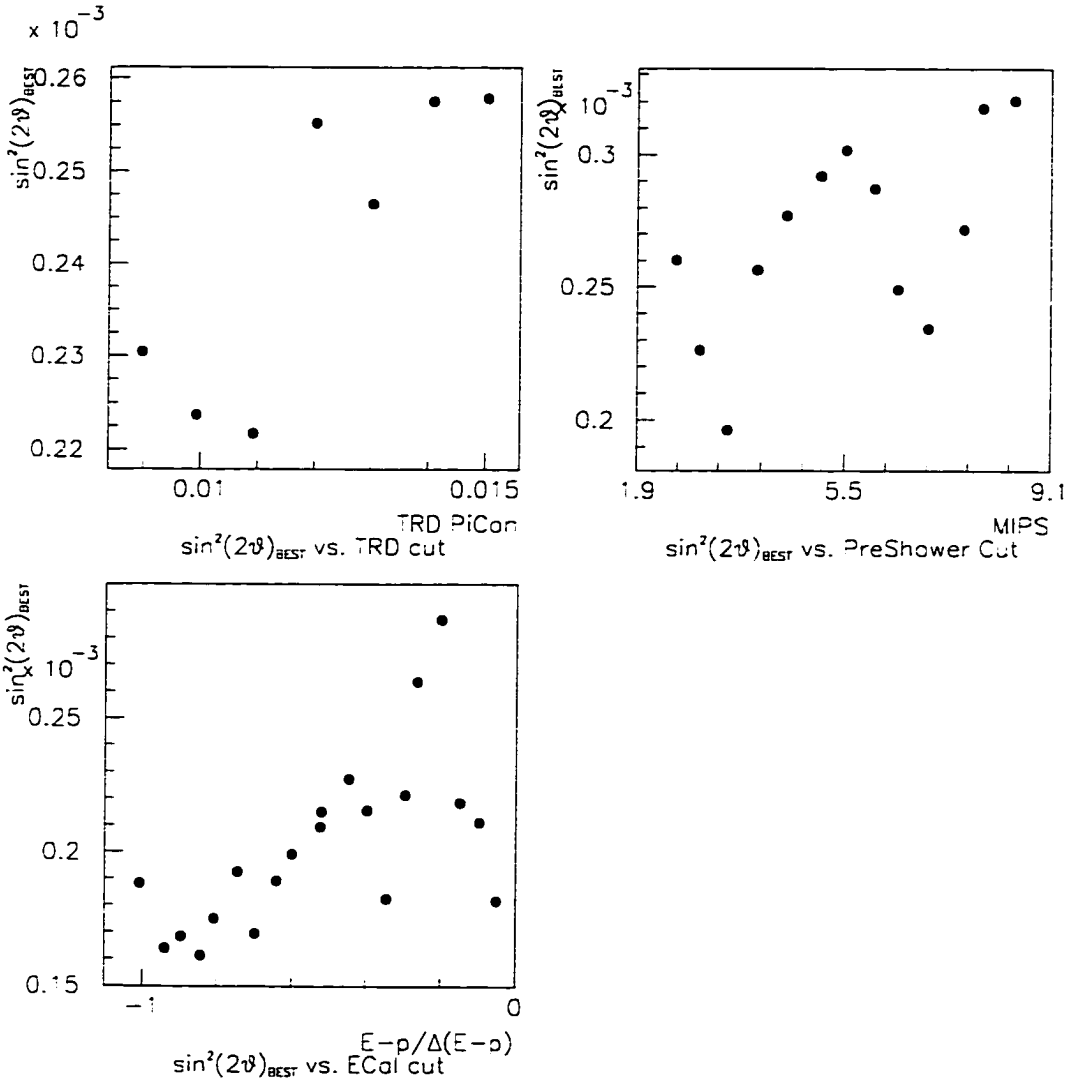

Figure 6.33: Variation in $\sin^2(2\theta)_{BEST}$ for Various Values of the Electron Selection Cuts.

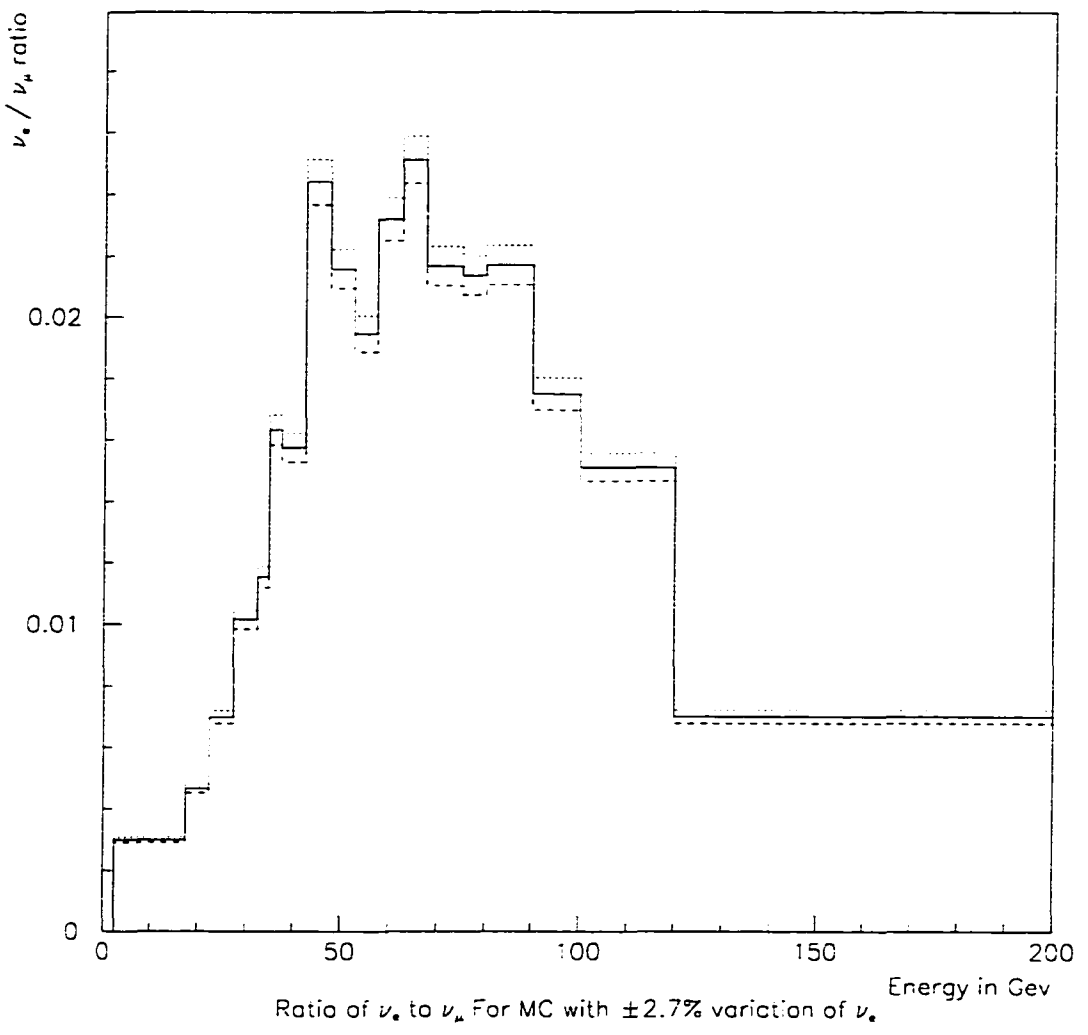

Figure 6.34: The ν_μ/ν_e Spectrum Ratio of the Simulation. The ν_e flux has been varied ±2.7%. The solid line is the nominal ratio, the dotted line is for −2.7%, and the dashed line is for +2.7%.

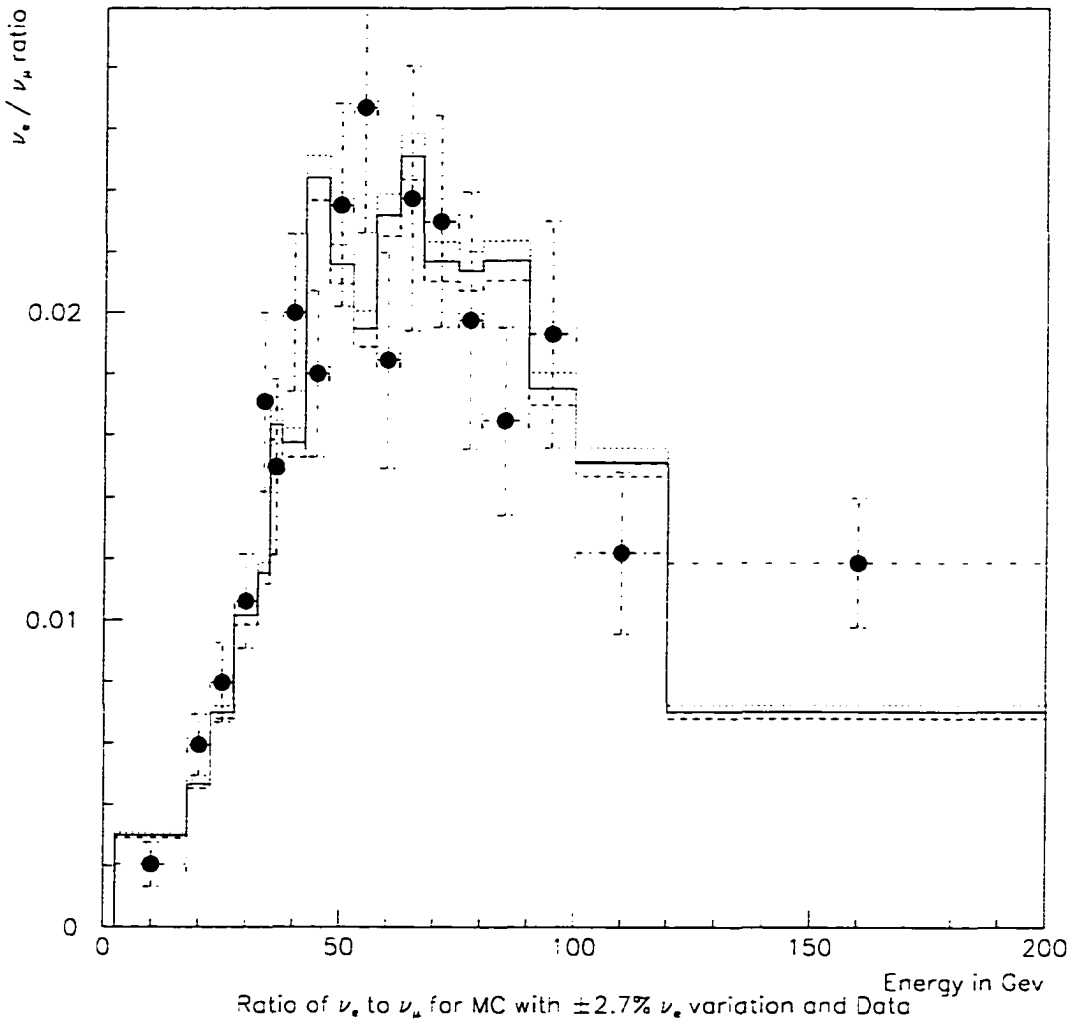

Figure 6.35: The ν_μ/ν_e Spectrum Ratio of the Simulation. The ν_e flux has been varied ±2.7%. The solid line is the nominal ratio, the dotted line is for −2.7%, and the dashed line is for +2.7%. The data, having been superimposed, is the dots.

Cut	Associated error
Q_t	0.7
p_t	0.3
Δz	0.3
Vertex	0.3
Q^2	0.5
W^2	0.7
TRD	0.04
PreShower	0.1
$E - p/\Delta(E - p)$	0.4
Flux	0.9
Electron Reconstruction	0.9

Table 6.8: Systematic Errors at the Δm Value of 250 eV^2/c^4. The errors are quoted in units of 10^{-3}.

generator cutoffs and muon identification. These effects were not taken into account in this analysis.

Chapter 7

Conclusion

A search for an excess of ν_e charged current events was conducted using the NOMAD detector with the data sample from the 1995 run in order to attempt to find a signal of excess ν_e's from the $\nu_\mu \rightarrow \nu_e$ oscillation process. A limit was then set at a 90% confidence level for this process. This is shown in Figure 7.1. The high mass limit on $\sin^2(2\theta)$ is 3.2×10^{-3}. A limit on Δm^2 is set below 1 eV^2 for full mixing and a limit of 2.1×10^{-3} can be set at the Δm^2 value of 26 eV^2 (see Table 7.1).

A large section of the LSND result in the high mass region can be excluded. This leads one to believe that if the LSND result is indeed an oscillation signal, it likely is an indication for oscillations in a lower Δm^2 region.

The major limitations of this analysis arise primarily from the limited statistical sample and the uncertainty in the beam composition. With the data samples from the 1996 and 1997 runs, the number of events should increase by close to

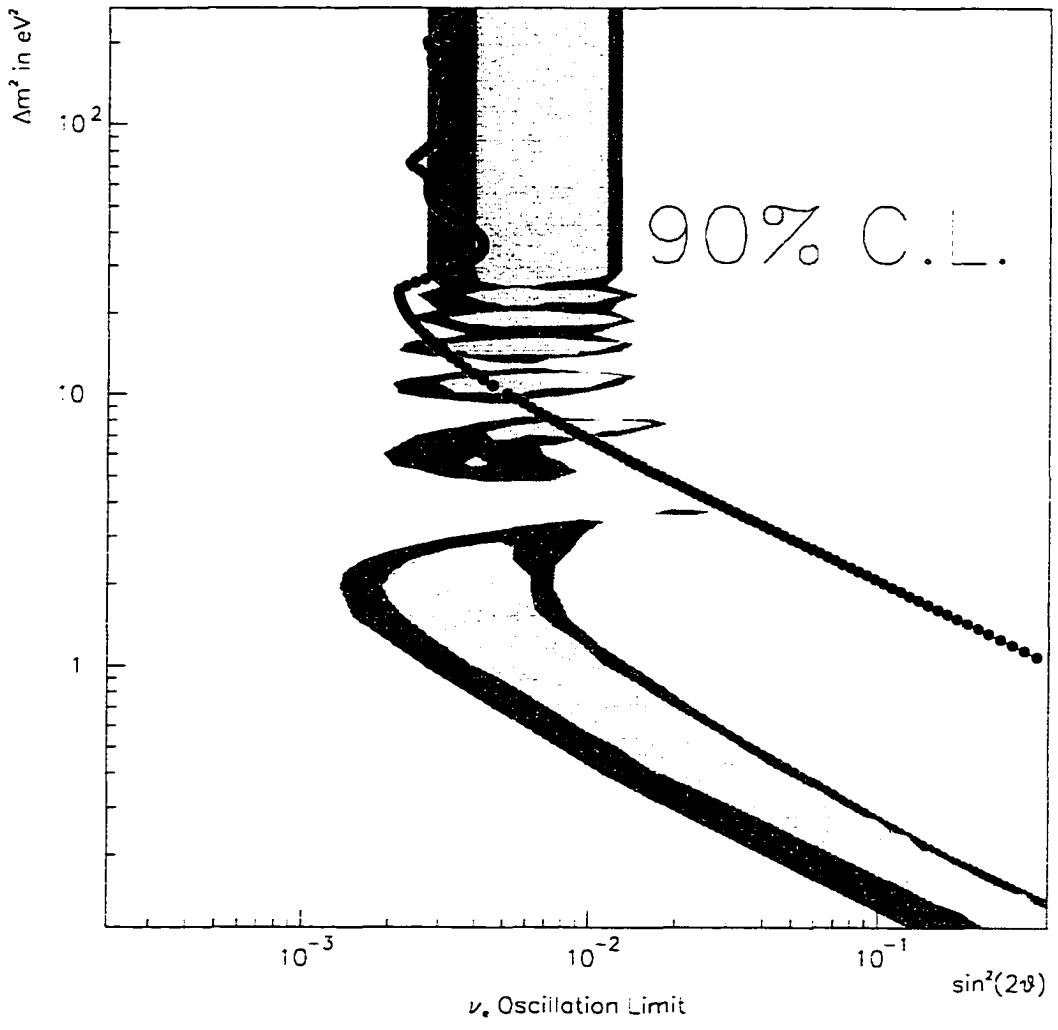

Figure 7.1: Final 90% C.L. Exclusion Region for this Analysis and the LSND Eesult. The dark line is the 90% C.L. limit for this analysis. The dark shaded region is the 99% allowed region for the LSND result and the light shaded region is the 90% allowed region.

Δm^2	$\sin^2(2\theta)_{BEST}$	90% C.L. $\sin^2(2\theta)$
1 eV^2	-0.14	0.34
10 eV^2	-1.9×10^{-3}	4.9×10^{-3}
26 eV^2	-3.7×10^{-4}	2.1×10^{-3}
50 eV^2	3.7×10^{-4}	2.8×10^{-3}
75 eV^2	1.1×10^{-6}	2.4×10^{-3}
100 eV^2	2.4×10^{-4}	3.0×10^{-3}
150 eV^2	4.0×10^{-4}	2.8×10^{-3}
200 eV^2	3.2×10^{-4}	2.6×10^{-3}
250 eV^2	5.8×10^{-4}	3.2×10^{-3}

Table 7.1: $\sin^2(2\theta)_{BEST}$ and 90% C.L. Limits for various Δm^2

an order of magnitude. Also, results from the SPY collaboration on the study of the pion to kaon ratios at different energies from 450 GeV protons on beryllium should be able to provide a useful comparison with the empirically derived neutrino spectrum used.

Bibliography

[1] Clowes, Dan, *Eightball*, Episode**9**, (Fantagraphics Books Inc., 1993).

[2] Cahn, Robert N. and Gerson Goldhaber, *The Experimental Foundations of Particle Physics* (New York, Cambridge University Press, 1991).

[3] Reines, F. and C.L. Cowan, Jr. "Free Antineutrino Absorbtion Cross Section. I. Measurement of the Free Antineutrino Absorbtion Cross Section by Protons," *Physical Review* **113** 273 (1959).

[4] Danby, G., et. al., "Observation of High-Energy Neutrino Reactions and the Existence of Two Kinds of Neutrinos," *Physical Review Letters* **9** 36 (1962).

[5] Perl, M. L. *et al.*, "Evidence for Anomalous Lepton Production in e^+e^- Annihilation." *Phys. Rev. Lett.*,**35**, 1489 (1975).

[6] Particle Data Group, *Phys. Rev. Lett.* **D34** (1996)

[7] Kesyer, B.,*Phys. Rev. D*, **24**,110 (1981)

[8] Bahcall, J.N. and Pinsonneault, M. H., *Rev. Mod. Phys.* **64**, 885 (1992).

[9] Langacker, P., *32nd International School of Subnuclear Physics*, Erice, 1994

[10] Wolfenstein, L.,*Phys. Rev.*, **D17** 2369 (1978)

[11] Mikheyev, S. P., Smirnov, A. Yu., *Nuovo Cimento* **C9** 17 (1986)

[12] Hirata, K.S. *et al.*,*Phys. Lett.* **B280**, 146 (1992)

[13] Becker-Szendy, R. *et al.*, *Phys. Rev.* **D46** 3720 (1992)

[14] Berger, Ch., *et al.*, *Z. Phys.*,**C66** 417 (1995)

[15] Aglietta, M. *et al.*, *Europhys. Lett* **8** 611 (1989)

[16] Goodman, M.C. *et al.*, *Nucl. Phys. B (Proc. Suppl.)*, **B38**,337 (1995)

[17] Anselmann, P. *et al.*,*Nucl. Phys. B (Proc. Suppl)*, **B38** 68 (1995)

[18] Abdurashitov, J.N.,*et al.*,*Nucl. Phys. B (Proc. Suppl)*, **B38** 60 (1995)

[19] Cleveland, B.T.,*et al.*,*Nucl. Phys. B (Proc. Suppl)*,**B38** 47 (1995)

[20] Suzuki, Y.,*et al.*,*Nucl. Phys. B (Proc. Suppl)*,**B38** 54 (1995)

[21] Athanassopoulos, C. *et al.*, *Phys. Rev. Lett.*,**77**, 3082 (1996)

[22] Armbruster, B. *et al.*,*Proc. of Int. Europhysics Conf. on High Energy Phys. EPS-HEP97, Jerusalem*, Aug. 19-26, (1997)

[23] Altegoer, J. *et al.*, *The NOMAD Experiment at the CERN SPS*, CERN-PPE/97-059, (1997)

[24] Dignan, T. *et al.*, NOMAD by Numbers, NOMAD Memo, (1994)

[25] Astier, P. *et al.*, *NOMAD Reconstruction Software, Drift Chamber package version 7.1*, NOMAD Software Note, (1996)

[26] Bird I. G. , *Vertex finding and fitting package*, NOMAD internal note. (1996)

[27] GEANT *Detector Description and Simulator Package*, CERN Programming Library Long Writeup W5013

[28] Fasso, A., *et al.*, FLUKA92, in *Proc. of the Workshop on Simulating Accelerator Radiation Environments*, Santa Fe, NM, (1993)

[29] SPY Collaboration, G. Ambrosini *et al.*, CERN-SPSLC/96-01 (1996)

[30] Das, R. and Mishra, S. R., NOMAD Memo 97-038, (1997)

[31] Meyer, J. P., and A. Rubbia, *NOMAD Event Generator Off-Line Manual (Draft)* NOMAD Software Note, (1994)

[32] Ingleman, G., "LEPTO version 6.1—The Lund Monte Carlo for Deep Inelastic Lepton–Nucleon Scattering," *Physics at HERA* (proceedings), Hamburg, October 1991, v. 3., p. 1366.

[33] Altegoer, J., et. al., *NOMAD GEANT Offline Manual* Version 5.11, NOMAD Software Note, (1996)

[34] Fesefeldt, H.C., "*Simulation of hadronic showers*", PITHA report 85-02, RWTH Aachen

[35] Geiser, A. and Long, J., *Study of ν_μ-CC events and Comparison with NUBEAM, NEGLIB and GENOM* NOMAD Memo 97-005, (1997)

[36] Fazio, T., *et al.*, NOMAD Memo 95-041, (1995)

[37] Fazio, T., *et al.*, *TRD Simulation Package* NOMAD Software Note, (1993)

[38] Steffan, P., NOMAD Memo 97-013, (1997)

[39] Hanssgen, K. and Ranft, J.,"The Monte Carlo Code NUCRIN", *Computer Physics Communications* **39** (1986), 53

[40] Baker, S. and Cousins, R. D., *Nuclear Insturements and Measurements*,**221**, 437,(1984)

[41] Feldman, G. J. and Cousins, R. D., NOMAD Memo 97-047, (1997)

[42] Weber, F., NOMAD Memo 97-029, (1997)

IMAGE EVALUATION TEST TARGET (QA-3)

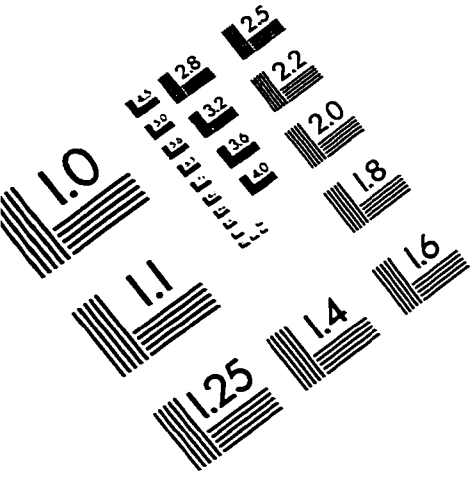

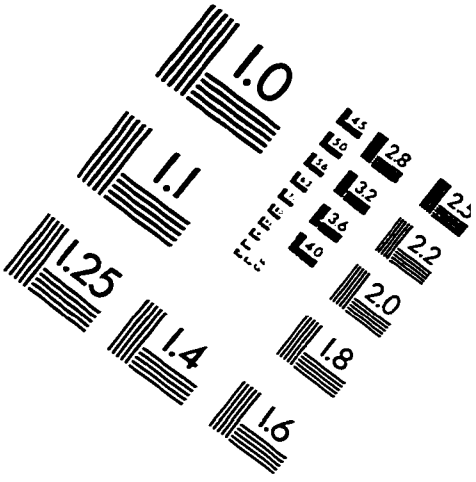

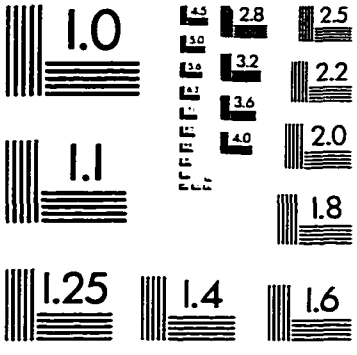

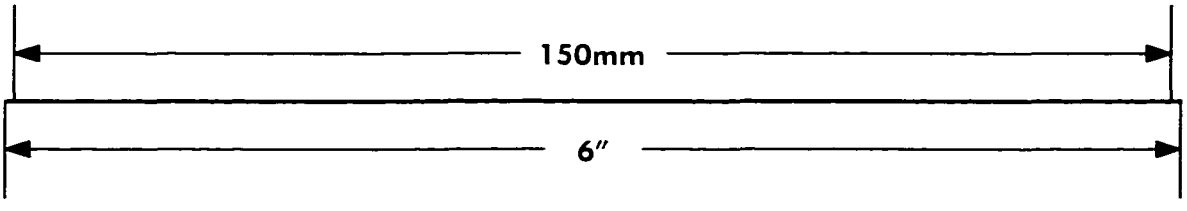

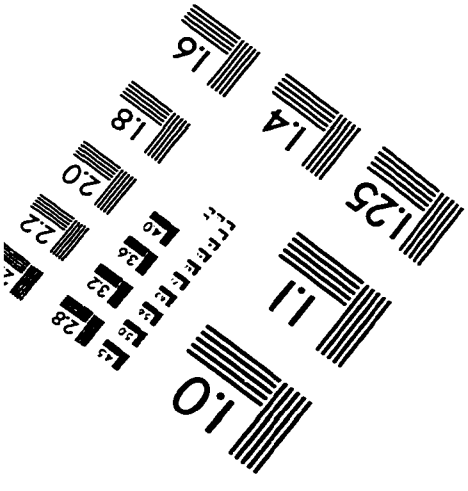

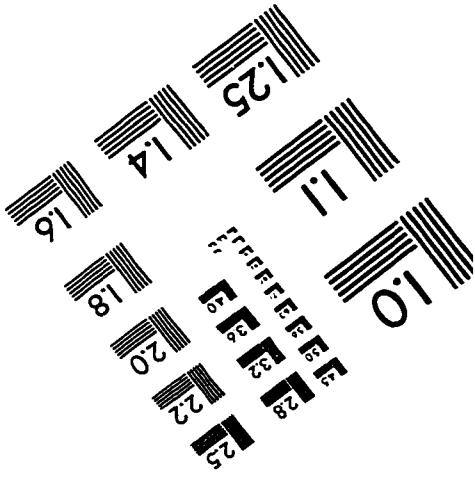

APPLIED IMAGE, Inc
1653 East Main Street
Rochester, NY 14609 USA
Phone: 716/482-0300
Fax: 716/288-5989